Bangor University

DOCTOR OF PHILOSOPHY

Characterisation and lifetime studies of CPDT- and BT- based photovoltaic cells

Waters, Richard

Award date:
2015

Awarding institution:
Bangor University

Characterisation and lifetime studies of CPDT- and BT-based photovoltaic cells

PRIFYSGOL
BANGOR
UNIVERSITY

Richard Huw Robert Waters

School of Electronic Engineering

Bangor University

A thesis submitted in partial fulfilment for the degree of

Doctor of Philosophy

July 2015

Declaration

This work has not previously been accepted in substance for any degree and is not being concurrently submitted in candidature for any degree.

Signed: Date:

STATEMENT 1

This thesis is the result of my own investigations, except where otherwise stated. Throughout the thesis, Prof Masaki Horie and his group at the National Tsing Hua University, Hsinchu, Taiwan, prepared all PCPDTBT-based materials. The group also provided the cyclic voltammetry data in section 4.2, UV-visible spectra in section 4.4.1, and the molecular weight and product yield calculations in section 4.5.1. Prof Masaki Horie and Dr Jeff Kettle developed the model for WAXS measurements in section 4.6, using data provided by the Cambridge Crystallographic Data Centre. Dr U-Ser Jeng at the National Synchrotron Radiation Research Centre, Hsinchu, Taiwan, was responsible for acquiring GISAXS and GIWAXS data in sections 5.2.6 and 6.8, including the modelling of PCBM aggregation. Noel Bristow assisted with EQE data acquisition in section 5.2.4. Prof Graham Smith at the University of Chester assisted with acquiring XPS data and instructing on analysis in section 5.5. Other sources are acknowledged by giving explicit references.

Signed: Date:

STATEMENT 2

I hereby give consent for my thesis, if accepted, to be available for photocopying and for inter-library loan, and for the title and summary to be made available to outside organisations.

Signed: Date:

Abstract

Organic photovoltaic (OPV) devices provide an opportunity for low cost, printable solar cells. This thesis focuses upon improving power conversion efficiencies (PCE) and lifetimes of OPV devices, with an emphasis on studying materials made from cyclopentadithiophene (CPDT) and benzothiadiazole (BT) monomers. The first part of the work focuses on characterising the optical and electrical properties of new materials based on this material system. A donor-acceptor-donor (D-A-D) small molecule, with the monomer order of CPDT-BT-CPDT (C2B1) was trialled and demonstrated an optical band gap of 1.8 eV. OFET mobility was measured as 5 x 10^{-3} $cm^2.V^{-1}.s^{-1}$ in the saturation region, and when blended with phenyl-C_{71}-butyric acid methyl ester ($PC_{71}BM$), gave a PCE of 1.54% under AM1.5G illumination. The moderate performance directed research towards donor-acceptor (D-A) polymers (PCPDTBT), synthesised using direct heterolytic arylation. OPV devices made with this material blended with $PC_{71}BM$ gave a maximum PCE of 4.23%, when tested under AM1.5G. OPV device performance is slightly higher than for PCPDTBT synthesised using more established techniques. This is the first known report of a working device with an active layer polymer synthesised using the direct heterolytic arylation route.

The stability of the PCPDTBT material was tested using a combination of OPV device data and analytical instruments. From device data, PCPDTBT was shown to be less stable than the more commonly reported P3HT material. Significantly, processing additives used to optimise the active layer morphology, are shown to be detrimental to long-term performance, approximately halving the device half-life ($T_{50\%}$). The physical changes are examined using Atomic Force Microscopy (AFM) and Grazing-Incidence Small-Angle X-ray Scattering (GISAXS) and show that the inclusion of processing additives leads to greater morphological changes during ageing experiments. The chemical changes occurring in PCPDTBT were examined using XPS and show that light soaking leads to observations of severe oxidation, with a break-up of the aromatic rings, formation of sulphates at the thiophene ring, chain scission in the polymer backbone and loss of side chains. However, it is concluded that morphological changes are mostly responsible for the observed decrease in OPV device PCE.

PCPDTBT with thermally initiated cross-linking behaviour is characterised and used to fabricate OPV cells. Cross-linkable PCPDTBT demonstrates a PCE of 3.65%, which is similar to its non-cross-linkable analogue, however, improved stability is observed from ageing experiments. This increase in stability, investigated further using AFM and GISAXS, is a result of fewer morphological changes in the active layer.

While the work has focussed on PCPDTBT, many of the conclusions regarding the analysis of material degradation could be of wider interest to the field. The analysis could provide some new insights, on the degradation and stability of conjugated polymers and fullerene derivatives.

Crynodeb

Rhodda dyfeisiau ffotofoltaidd organig (OPV) gyfle i wneud celloedd solar cost isel ac argraffedig. Mae'r thesis hwn yn canolbwyntio ar wella effeithlonrwydd trosi pŵer ac oes bywyd dyfeisiau OPV, gyda phwyslais ar ddeunyddiau a wnaed o monomerau cyclopentadithiophene (CPDT) a benzothiadiazole (BT). Canolbwyntia rhan gyntaf y gwaith ar nodweddu priodweddau optegol a thrydanol deunyddiau newydd yn seiliedig ar CPDT a BT. Profwyd moleciwl rhoddwr-derbyniwr-rhoddwr (CPDTB-BT-CPDT [C2B1]) bach newydd, sydd yn dangos bwlch egni optegol o 1.8 eV. Mesurwyd symudedd gwefr o 5 x 10^{-3} $cm^{2}.V^{-1}.s^{-1}$ gyda dyfais OFET yn rhanbarth dirlawn, a phan y'i cymysgwyd gyda ffenyl-C_{71}-asid bwtyrig ester methyl ($PC_{71}BM$), rhoddodd effeithlonedd o 1.54% o dan olau AM1.5G. Ysgogodd y perfformiad cymedrol hwn i'r gwaith ganolbwyntio ar bolymerau rhoddwr-derbyniwr PCPDTBT a wnaed gan ddefnyddio aryleiddiad heterolytig uniongyrchol. Rhoddodd dyfeisiau OPV a wnaed gyda'r deunydd hwn gyda $PC_{71}BM$ effeithlonedd o 4.23%, pan brofwyd o dan AM1.5G. Mae'r perfformiad ychydig yn uwch nag i PCPDTBT a wnaed gan ddefnyddio technegau mwy sefydledig. Hwn yw'r adroddiad hysbys cyntaf o ddyfeisiau'n gweithio, gyda deunydd a wnaed gyda aryleiddiad heterolytig uniongyrchol.

Profwyd sefydlogrwydd PCPDTBT gyda chyfuniad o ddyfeisiau OPV ac offer dadansoddi. O ddata dyfeisiau, dangoswyd PCPDTBT i fod yn llai sefydlog na P3HT, sydd yn ddeunydd a ddefnyddir yn aml. Dangoswyd bod ychwanegion prosesu i optimeiddio morffoleg haenau gweithredol, yn niweidiol i berfformiad hirdymor, gan arwain at haneru'r hanner-oes ($T_{50\%}$). Archwiliwyd y newidiadau ffisegol gyda microsgopeg grym atomig (AFM) a gwasgariad pelydr-x o ongl-bach trawol (GISAXS), sydd yn dangos bod ychwanegion prosesu yn arwain at fwy o newidiadau morffolegol wrth heneiddio. Defnyddiwyd sbectrosgopeg ffoto-electron pelydr-x (XPS) i ddangos bod boddi golau yn arwain at ocsidiad difrifol, gan dorri cylchoedd aromatig, ffurfio sylffadau ar y cylch thioffen, hollti cadwyn y polymer, a cholled ochr-gadwynau. Daethpwyd i gasgliad bod newidiadau morffolegol yn gyfrifol am y dirywiad mwyaf mewn dyfeisiau OPV.

Cynhyrchwyd PCPDTBT a drawsgysylltiwyd yn thermol, ei nodweddu, a'i ddefnyddio i greu dyfeisiau OPV. Dangosa PCPDTBT a drawsgysylltiwyd effeithlonedd o 3.65%, sydd yn debyg i'r deunydd cyfatebol sydd heb ei drawsgysylltu. Gwelwyd sefydlogrwydd uwch gydag arbrofion heneiddio. Daw'r cynyddiad mewn sefydlogrwydd, a ymchwiliwyd gyda AFM a GISAXS, oherwydd llai o newidiadau morffolegol yn yr haen weithredol.

Tra bod y gwaith wedi canolbwyntio ar PCPDTBT, dichon fod nifer o'r casgliadau ar ddirywiad deunyddiau o ddiddordeb ehangach i'r maes. Gall y dadansoddi rhoi syniadau newydd ar sefydlogrwydd a dirywiad polymerau cyfieuol a deilliaid ffuleren

Acknowledgements

I would like to thank first and foremost my supervisor Dr Jeff Kettle for giving me this opportunity, and for his supervision and guidance throughout the previous three and a half years.

During my time at Bangor University I have had the pleasure of meeting, working and collaborating with many interesting people. I would like to extend my thanks, in no particular order, to Noel, Vasil, Ding, Omar, Eifion, Colin, Rafael, Elder, Bruno, Mike Lewis, Sanjay, Michal, Iwan, David, Yvonne, Julie, Siân, Gaynor, Wendy, Roger, Dr Yanhua, Dr Mohammed, Professor Alan, Professor Martin and Dr Saad. I would like to particularly thank Dr Paul Sayers for his work in maintaining an efficient working environment. Thanks also to Professor Lewis for his interesting questions.

Thanks also to my family and friends.

Diolch, o hyd, i Dad a Mari.

Publications

- Jeff Kettle, **Huw Waters**, Masaki Horie, and Shu-Wei Chang. "Effect of hole transporting layers on the performance of PCPDTBT: PCBM organic solar cells." *Journal of Physics D: Applied Physics* 45, no. 12 (2012): 125102.

- Shu-Wei Chang, **Huw Waters**, Jeff Kettle, and Masaki Horie. "Cyclopentadithiophene–benzothiadiazole oligomers: Synthesis via direct arylation, X-ray crystallography, optical properties, solution casted field-effect transistor and photovoltaic characteristics." *Organic Electronics* 13, no. 12 (2012): 2967-2974.

- Shu-Wei Chang, **Huw Waters**, Jeff Kettle, Zi-Rui Kuo, Chun-Han Li, Chin-Yang Yu, and Masaki Horie. "Pd-Catalysed Direct Arylation Polymerisation for Synthesis of Low-Bandgap Conjugated Polymers and Photovoltaic Performance." *Macromolecular rapid communications* 33, no. 22 (2012): 1927-1932.

- **Huw Waters**, Jeff Kettle, Shu-Wei Chang, Chun-Jen Su, Wei-Ru Wu, U-Ser Jeng, Ya-Ching Tsai, and Masaki Horie. "Organic photovoltaics based on a crosslinkable PCPDTBT analogue; synthesis, morphological studies, solar cell performance and enhanced lifetime." *Journal of Materials Chemistry A* 1, no. 25 (2013): 7370-7378.

- **Huw Waters**, Noel Bristow, Omar Moudam, Shu-Wei Chang, Chun-Jen Su, Wei-Ru Wu, U-Ser Jeng, Masaki Horie, and Jeff Kettle. "Effect of processing additive 1, 8-octanedithiol on the lifetime of PCPDTBT based Organic Photovoltaics." *Organic Electronics* 15, no. 10 (2014): 2433-2438.

- Jeff Kettle**, Huw Waters**, Ziqian Ding, Masaki Horie, and Graham Smith. “Chemical change studies in PCPDTBT:PCBM solar cells using XPS and TOF-SIMS and the use of inverted cell structure for improving lifetime.” *Solar energy materials and solar cells* 141. (2015): 139-147. (

- Jeff Kettle**, Huw Waters**, Masaki Horie, and Graham Smith. “Alternative processing additives for PCPDTBT-based solar cells for enhanced stability.” *Journal of Applied Physics*. (Under review.)

- Shu-Wei Chang, **Huw Waters**, Jeff Kettle, Masaki Horie, “Cyclopentadithiophene-benzothiadiazole copolymers with various lengths of repeating unit; synthesis, optical and electrochemical properties and photovoltaic characteristics.” *Macromolecules chemistry and Physics*. (Under review.)

Conferences

- Centre for Advanced Functional Materials and Devices (CAFMad), Postgraduate Conference. Dolgellau, Wales. 2012. Oral. *New polymers and oligomers for printing of next-generation solar cells.*

- Saint David’s Day Poster Competition. Y Senedd, Cardiff, Wales. 2012. Poster. *New polymers and oligomers for printing of next-generation solar cells.*

- Society of Information Displays (SID) [UK / Ireland Chapter]. Imperial College, London. 2012. Poster. *Cyclopentadithiophene-benzothiadiazole based oligomers and polymers for OPVs.*

- Institute of Physics Ireland, Spring Meeting. Galway, Ireland. 2013. Poster. *Organic photovoltaics based on a cross-linkable PCPDTBT analogue.*

- Cynhadledd Rhyngwladol 2014, Y Coleg Cymraeg Cenedlaethol (International Conference 2014, The Welsh National College). The Millennium Centre, Cardiff, Wales. 2014. Poster. *Celloedd ffotofoltaëg plastig (Plastic photovoltaic cells).*

- International Summit on OPV Stability (ISOS). Barcelona, Spain. 2014. Poster. *Lifetime studies on PCPDTBT·PCBM solar cells.*

Contents

List of figures

List of tables

Chapter 1 Introduction

The US Government's Energy Information Administration estimates that the world's energy consumption will increase by as much as 56% between 2010 and 2040. The majority of this energy demand is predicted to come from developing non-OECD (Organisation for Economic Co-operation and Development) nations (see Figure 1.1) [1].

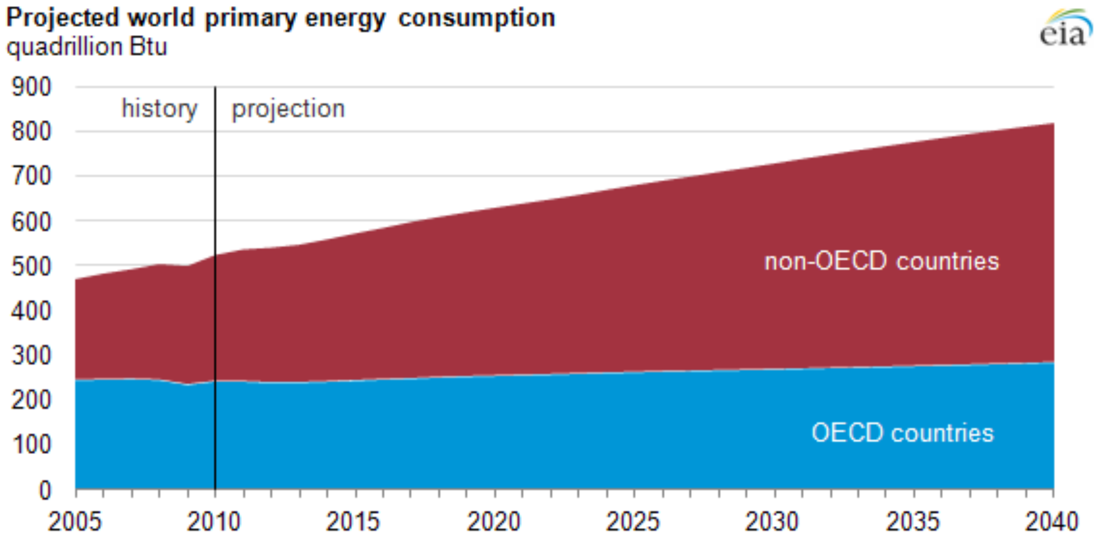

Figure 1.1: The projected energy requirements of the world, and the split between OECD and non-OECD countries [1].

Continued developments, especially in non-OECD countries, will inevitably lead to increased energy demands. Non-renewable energy sources are polluting, and likely to become more and more expensive due to their finite availability. On the other hand, non-polluting renewable energy sources are infinitely available, and are reducing in cost with increased uptake. Among them, wind is the most widely used renewable energy source in the UK. Many reports show that wind alone cannot supply the UK's energy needs, and can only contribute to an 'energy mix' [2]. Hydroelectric requires the tidal power of the sea or a moving water source such as a river, limiting its geographical deployment. Solar electricity generation has grown dramatically in the UK over the past ten years. This growth is due to the falling cost of solar modules and government feed-in tariffs. In the UK, the average solar insolation level is 1050 kWh.m^{-2}.year^{-1} [3]. While this is significantly lower than most of Europe, the levels in the south of the UK are comparable to most of Germany, which is the largest solar electricity producer in the world. As of December 2014, solar energy is expected to have a peak grid contribution of over 4 GWp (Giga Watt peak) in the UK [4].

Solar cell technologies are broadly categorised into three *generations*. First-generation solar cells based upon polycrystalline silicon (poly-Si) are the most commonly used, due to the low-cost of modules and the long-established use of silicon in microelectronics [5]. Commercially available first generation solar cells give power conversion efficiencies (PCE) of 15 to 20%, due to silicon's favourable 1.1 eV band gap and an optimised cell structure [6]. Poly-Si efficiently absorbs from 400 to 1100 nm of the solar spectrum, but poorly for wavelengths greater than 1100 nm, where 15% of the total solar flux is present (based upon the AM1.5G spectrum from the ASTM G173-03 standard - see Figure 1.2).

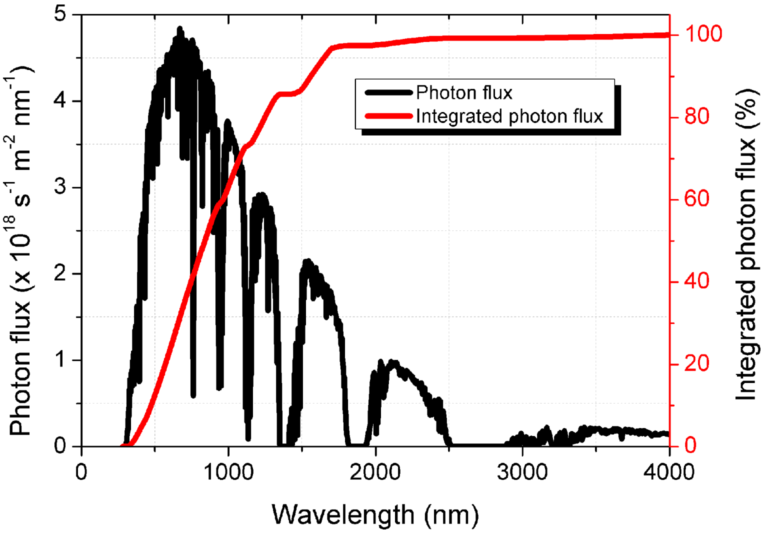

Figure 1.2: Solar photon flux as a function of wavelength (in black). Overlaid is the integrated photon flux with the axis on the right (in red).

Second-generation solar cells are based upon thin film technologies and include amorphous silicon (a-Si), copper indium gallium selenide Cu(In,Ga)(Se,S)$_2$ [CIGS] or cadmium telluride (CdTe) [7, 8]. Although they have lower PCEs of 10 to 15%, their fabrication costs are potentially reduced, owing to thinner active layers and reduced material requirements. The cost of poly-Si modules has decreased dramatically in the past ten years, making it difficult for second-generation cells to compete commercially. Recently, First Solar (US) have claimed to manufacture CdTe cells at a cost lower than poly-Si, but these are only available to large commercial solar farms [9].

Third generation solar cells use materials such as small molecules or polymers [10], but also cover expensive experimental multi-junction solar cells. These multi-junction solar cells currently hold the highest recorded efficiencies, but are only used for space applications or high concentrator systems due to their very high production costs. Organic materials are abundant and can be used in high-volume production methods, such as roll-to-roll (R2R) or printing over large surface areas. Organic photovoltaic (OPV) cells have many other advantages, such as not requiring high temperatures during fabrication. Unlike other technologies, rare metals are not used. Also, OPV appearance is tunable to different colours by varying the active layer material.

Since January 1993, Green et al. [11] have published updated verified record efficiencies for all PV cells. As shown in Figure 1.3, OPV efficiencies were first recorded in 2001, when the University of Linz reported a PCE surpassing 3%, and have now demonstrated verified efficiencies of up to 11.9%, as seen in Figure 1.3 [11]. For any PV technology to succeed, it is necessary to fulfil the requirements of the *critical triangle*: high PCE, high stability and low cost [12]. Whilst the efficiencies have steadily increased over the past 15 years, their low stability inhibits many commercial applications. The many problems in attaining suitable stability are complex and discussed in further detail in the literature review.

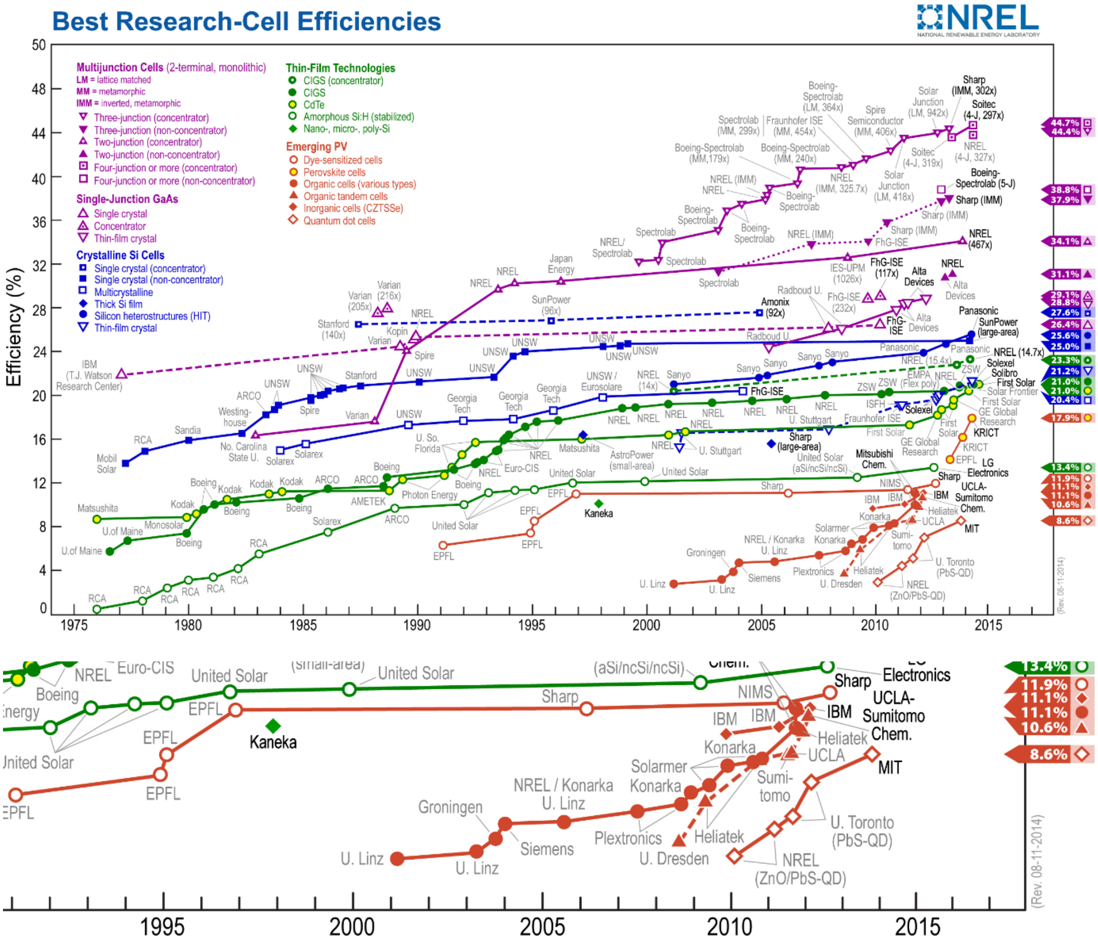

Figure 1.3: A comparison of verified record efficiencies for all PV material systems undertaken by NREL (top). The chart was downloaded 1st February 2015. An enlargement (bottom) of the PCE breakthroughs for organic semiconductor based PV [11].

The work contained in this thesis focused on studying the stability of organic solar cells made with cyclopentadithiophene (CPDT) - benzothiadiazole (BT) materials. CPDT and BT show promise as high performing OPV materials due to their more extended electron delocalisation in the ground state, more planar molecular geometries, and more rigid structures, leading to smaller energy-gaps and closer intermolecular interactions [13, 14]. These materials have already shown good hole mobilities when used in FET devices. Initially, the work focused upon the screening of promising active layers. A larger section of this thesis is devoted to studying the performance and chemical degradation of CPDTBT-BT-based OPV cells with time. The effects of initial processing conditions and degradation routes for the material were studied, using X-ray Photoelectron Spectroscopy (XPS) and Grazing Incident Small-Angle X-ray Scattering (GISAXS). To the author's knowledge, this is one of the first times that this material has been extensively studied for stability, and it is envisaged that many of the conclusions are applicable to other materials. Finally, attempts to improve the stability of this material were studied using a cross-linkable CPDT-BT based polymer.

The work contained within this thesis is original, containing several prominent discoveries. The three most significant achievements are:

- Reporting on the chemical degradation pathways of PCPDTBT-based materials;
- Discovering that processing additives tend to have negative effects upon the long-term stability of OPV cells;
- Demonstrating that polymers based upon cross-linked allyl side chains improves the air stability of OPV cells.

1.1 Thesis outline

The structure of this thesis is as follows:

Chapter 2 discusses the physics underpinning OPV operation and the current state of the art of OPV materials. The discussion also includes the many degradation mechanisms that inhibit long-term stability.

Chapter 3 outlines the experimental methods used in this thesis for fabricating OPV. Discussed are the testing and analytical techniques used for investigating degradation pathways of OPV cells.

Chapter 4 is the first of three results chapters. New CPDT-BT based oligomers and polymers are screened for performance. Their optoelectrical properties and OPV performances are reported. Also studied are the effects of CPDT-BT synthetic route upon OPV performance.

Chapter 5 reports on the stability of PCPDTBT-based OPV cells using indoor testing. Degradation pathways are studied using several analytical techniques.

Chapter 6 discusses the effect of attaching a cross-linkable side chain to CPDT-BT based polymers. The performance and stability of cross-linkable CPDT-BT are studied.

Chapter 7 summarises the main findings in this thesis and suggests directions for future work.

Chapter 2 Literature review

The first part of this chapter reviews the basic physics underpinning OPV cell operation. Secondly, a summary is provided of the materials used during fabrication, with particular attention given to poly[2,6-(4,4-bis-(2-ethylhexyl)-4*H*-cyclopenta[2,1-*b*;3,4-*b*']dithiophene)-*alt*-4,7(2,1,3-benzothiadiazole)] [PCPDTBT], as this thesis focuses on polymer and fullerene bulk-heterojunction solar cells. The chapter culminates with a review of OPV degradation mechanisms.

2.1 Device operation

OPV cells convert photon energy into electrical energy in an active layer sandwiched between electrodes of different work functions (see Figure 2.1). OPV active layers typically contain a p-type (donor) polymer and an n-type (acceptor) fullerene. One of the electrodes is transparent for illumination of the active layer. Buffer or interfacial layers are often applied between the electrodes and the active layer. These interfacial layers ensure charge-selective transport to the electrodes. An OPV cell's efficiency is, therefore, dependent on the properties of a number of layers. Converting photon energy to electrical energy is a product of fundamental processes. The relationship between each process is defined by the equation

$$\eta_{efficiency} = \eta_{abs} \times \eta_{diss} \times \eta_{trans} \times \eta_{col} \tag{2.1}$$

where the overall device efficiency ($\eta_{efficiency}$) can be related to the efficiencies of photon absorption (η_{abs}), exciton dissociation (η_{diss}), charge transport (η_{trans}) and charge collection (η_{col}). All of these efficiencies are critical and need to be maximised to obtain a high overall device efficiency ($\eta_{efficiency}$).

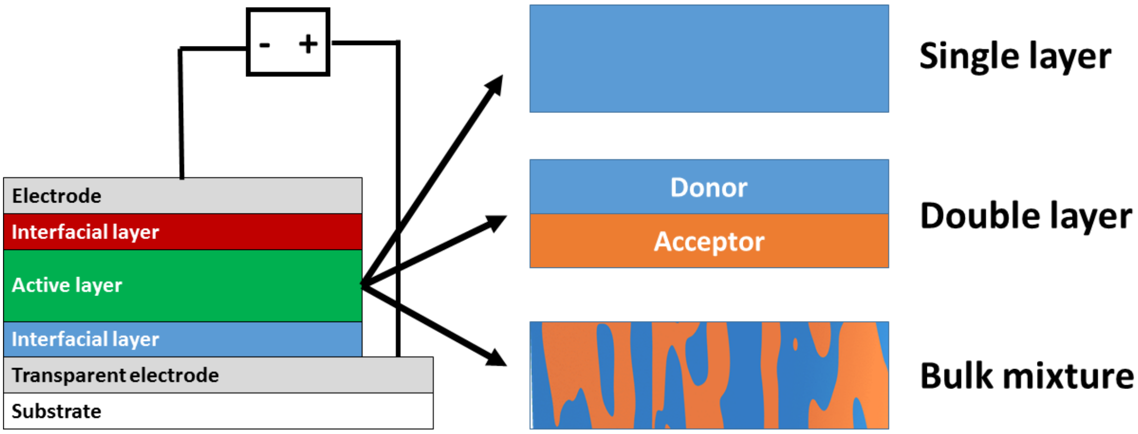

Figure 2.1: An example of an OPV cell stack, along with possible active layer structures. The photocurrent is extracted to an external circuit via the electrodes.

2.1.1 Equivalent circuit model

Figure 2.2 shows an equivalent circuit model for an OPV cell. Each of the efficiencies defined in equation (2.1 are related to the circuit components. With the diode acting as a rectifier, maximising the extractable photocurrent (I_L) requires a large shunt resistance (R_{SH}), and a small series resistance (R_S). Initial photocurrent generation (I_L) requires high photon absorption (leading to a high value of η_{abs}) and high effective exciton dissociation (η_{diss}). Poor active layer morphology, or electrical short-circuits bypassing the rectification behaviour of the cell, is correlated to low R_{SH} (leading to a decrease in the value of η_{trans}). A non-optimum interface between the cell's active layer and electrodes, giving a low R_{SH}, can lead to bimolecular charge recombination losses (reducing the value of η_{col}). R_S is given by the sum of the inherent resistance in each layer. Degradation of a particular layer, leading to the material behaving more as an electrical insulator, would ultimately increase R_S.

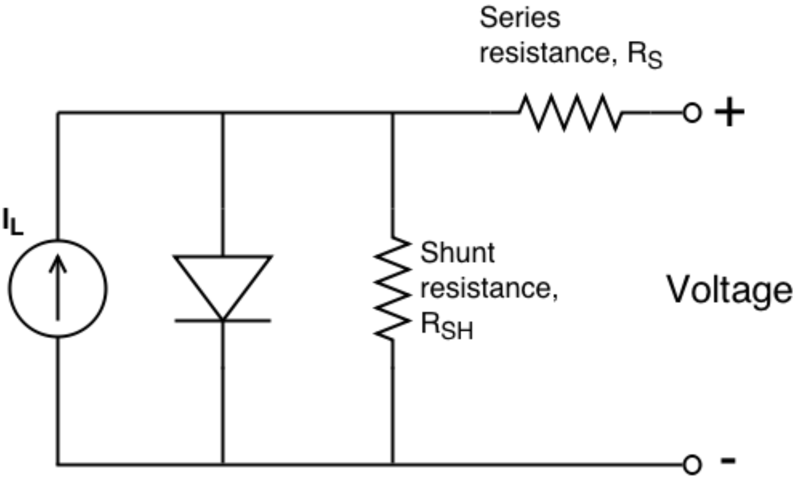

Figure 2.2: The equivalent circuit for an OPV cell. Increased series resistance inhibits charge from being extracted to an external circuit. Decreased shunt resistance bypasses photocurrent pathways, also leading to a reduction in performance.

2.1.2 Photon absorption and exciton dissociation

Polymer-fullerene solar cells use materials capable of absorbing from the UV to infrared, due to intra-band transitions. Materials are selected to capture as much of the AM1.5G spectrum (see Figure 1.2) as possible, leading to higher values of η_{abs}. Upon photon absorption in the donor material, an electron is excited from the highest occupied molecular orbit (HOMO) to the lowest unoccupied molecular orbit (LUMO). The excited electron leaves behind a hole in the HOMO, which remains bound to the excited electron by a Coulombic force [Figure 2.3 (a)]. This bound hole-electron pair is known as an exciton. It is worth noting that Figure 2.3 only shows processes occurring in the donor, but analogous processes can occur in the acceptor.

Subsequently, excitons diffuse through the donor to the interface with the acceptor material [Figure 2.3 (b)]. An inability to reach the interface in a short enough time (~1 ns), leads to the recombination of the hole and electron of the exciton (and a subsequent reduction in η_{diss}) [15]. At the donor-acceptor interface, the electron of the exciton is transferred from the donor to the acceptor [Figure 2.3 (c)]. Electron transfer only occurs if the difference between the electron energy of the donor and the corresponding acceptor level is larger than the exciton binding energy, which is approximately the difference between LUMO energy levels. A hole is present in the HOMO of the donor, with the electron present in the LUMO of the acceptor in a charge-transfer complex.

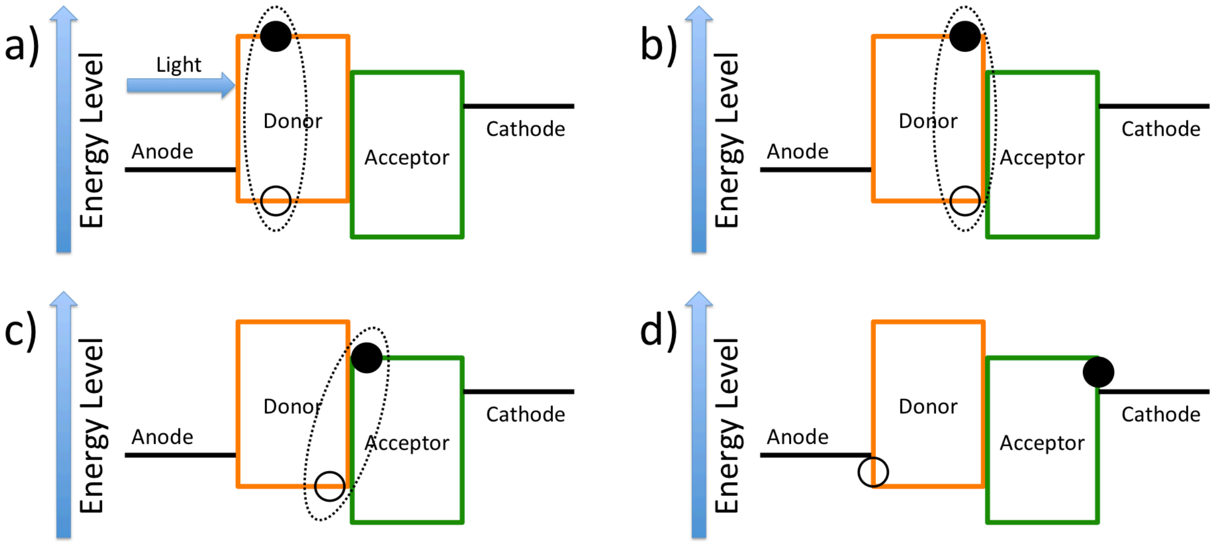

Figure 2.3: a) A photon is absorbed, exciting an electron from the donor's HOMO to its LUMO. b) The bound hole-electron pair diffuses towards the donor-acceptor interface. c) Providing the LUMO offset is greater than the exciton Coulombic binding energy, the electron is transferred from the LUMO of the donor to the LUMO of the acceptor. d) The separation of the weakly bound electron and hole into free charge carriers, which are then collected at their respective electrodes [15, 16].

2.1.3 Charge transport and collection

An electric field is necessary for charge separation, induced by the work function mismatch between the anode and cathode. The electric field drives electrons to the fullerene and holes to the polymer. Charges will drift to their respective electrodes via hopping processes (the efficiency of this process determines η_{trans}). Once at their respective electrodes, the hole and electron can be extracted to generate a photocurrent [Figure 2.3 (d)]. A good interface between donor and acceptor materials and their corresponding electrodes is critical for effective charge extraction, and reduced charge recombination (leading to high values of η_{col}).

2.1.4 Device characterisation

An OPV cell's PCE is determined from its current-voltage (I-V) characteristics, where the electrodes are biased with an incrementing voltage and the resulting photocurrent measured (shown in Figure 2.4).

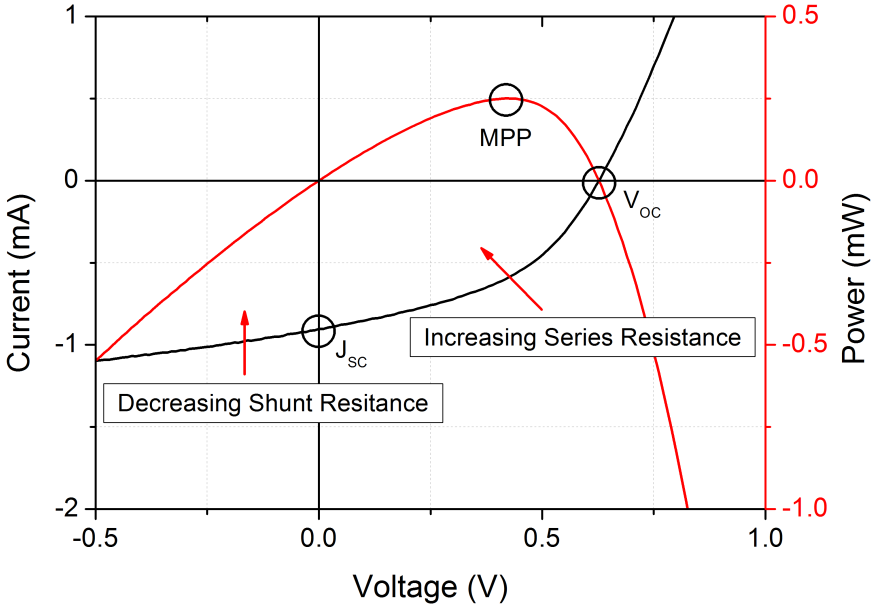

Figure 2.4: Shown are the measured current and power output as a function of applied bias. The maximum power point (MPP) represents a point on the I-V curve where the power output is at its maximum. A decreasing shunt resistance (R_{SH}) or increase in series resistance (R_S) leads to a reduction in MPP, and thus FF.

PCE is a product of the cell's open-circuit voltage (V_{OC}), short-circuit current density (J_{SC}) and fill factor (FF), divided by the incident radiant power, defined by the equation

$$PCE = \frac{V_{OC} \times J_{SC} \times FF}{Power\ of\ irradiation} \tag{2.2}$$

These four parameters are used in this thesis to evaluate performance and stability.

The origins of the V_{OC} in polymer-fullerene solar cells have been the subject of much discussion in literature. V_{OC} was initially shown to be determined by the electrode work function difference [17, 18]. Scharber et al. [17] also showed that V_{OC} has an almost linear dependence upon the effective energy gap of the donor and acceptor materials (see Figure 2.5).

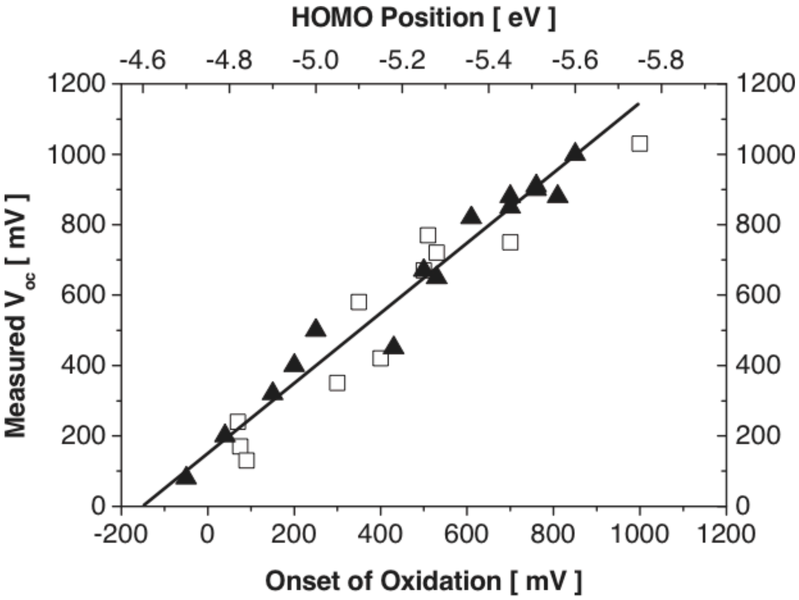

Figure 2.5: The linear relationship between the effective energy gap between the polymer HOMO and PCBM's LUMO, as reported by Scharber et al. [17].

In Figure 2.5, it can be seen that the relationship between the LUMO (shown as the Onset of Oxidation) and the HOMO is linear. Scharber et al. [17] deduced the following relationship for V_{OC}, defined by the equation

$$V_{OC} = HOMO_{DONOR} - LUMO_{ACCEPTOR}) - 0.3\ eV \tag{2.3}$$

where $\mathrm{HOMO}_{\mathrm{DONOR}}$ and $\mathrm{LUMO}_{\mathrm{ACCEPTOR}}$ are the respective energy levels of the active layer materials. The offset of -0.3 eV was believed to originate from the splitting of the electrochemical potentials of holes and electrons determined by the Fermionic nature of charge carriers [19, 20], however this was not discernable from Figure 2.5. Experimental work by Mihailetchi et al. [21] indicated that V_{OC} was determined by the work function difference when non-Ohmic electrodes were used. The use of Ohmic electrodes demonstrated the same behaviour seen by Scharber et al. The effective energy gap has also been shown to be influenced by the active layer morphology [18, 22, 23].

FF is an OPV cell's maximum obtainable power divided by the product of V_{OC} and J_{SC}, and is a measure of ideality. FF is defined by the equation

$$FF = \frac{V_{MPP} \times J_{MPP}}{V_{OC} \times J_{SC}} \tag{2.4}$$

OPV cells with zero losses (maximum η_{diss}, η_{trans} and η_{col}) are not attainable due to the Shockley-Queisser limit, where any energy lost is converted to heat. However, parasitic resistances, R_S and R_{SH} significantly affect FF. Typically a high performing OPV cell demonstrates an FF in the range of 65% [24]. Since FF is a measure of loss it takes into account several factors, many which are attributed to the morphology of the active layer. The shape of I-V curves (as shown in Figure 2.4) shows changes in R_{SH} and R_S and provides information on the changes occurring in the cell.

2.2 OPV design consideration

2.2.1 Active layer structures

During diffusion, excitons may geminately recombine if the distance to the donor-acceptor interface is too great. Numerous values for the exciton diffusion path lengths are reported, and range from 1 nm to 20 nm, depending on the material system and process conditions [25]. A high efficiency of dissociation (η_{diss}) at the donor-acceptor interface is, therefore, required to reduce exciton recombination.

Two active layer structures are employed in OPV cells, taking into account the relatively short exciton diffusion path lengths. The first approach uses a bilayer heterojunction [shown in Figure 2.1 (double layer)], where an acceptor layer is on top of the donor layer forming a single plane interface [26]. Each of these layers should be thin enough so that their thicknesses are within the exciton diffusion path lengths. This approach limits photon absorption due to the relative thinness of donor-acceptor layers. The second approach uses a bulk heterojunction (BHJ) [shown in Figure 2.1 (bulk mixture)], where donor and acceptor materials are coated from the same solution. During the coating and drying stages, the donor and acceptor materials separate, leading to interconnected and independent phases. This phase separation can lead to a greater total interface area, compared to the planar bilayer architecture. These interconnected phases are interdigitated, with dimensions of the exciton diffusion path length, thus increasing the probability of exciton dissociation. Since donor and acceptor phases are within the exciton diffusion path lengths of each other, it is possible to use thicker active layers, further increasing photon absorption (η_{abs}).

One novel approach developed by a number of authors including Huck et al. [27], is controlling the morphology by nanoimprinting (Figure 2.6). Nanoimprinting leads to highly ordered ‘pillars’ of either donor or acceptor materials. While the approach leads to improved electrical performance through increased FF, PCE increases are rarely seen due to a decrease in J_{SC}.

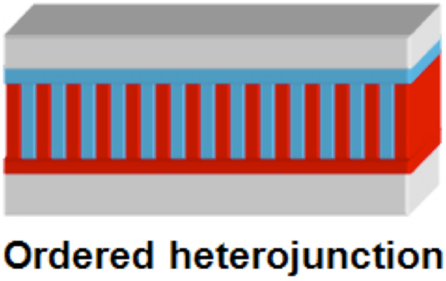

Figure 2.6: An ideally ordered bulk heterojunction. A bulk heterojunction increases the interface between p and n-type materials.

2.2.2 Interfacial layers

In the typical OPV cell architecture shown in Figure 2.1, there are three primary components: a transparent front electrode, an organic photoactive layer and a second electrode. Holes and electrons are transferred from the active layer to the Fermi levels of their respective electrodes. Fermi levels significantly different to the HOMO of the polymer or LUMO of the acceptor lead to bimolecular (non-geminate) recombination.

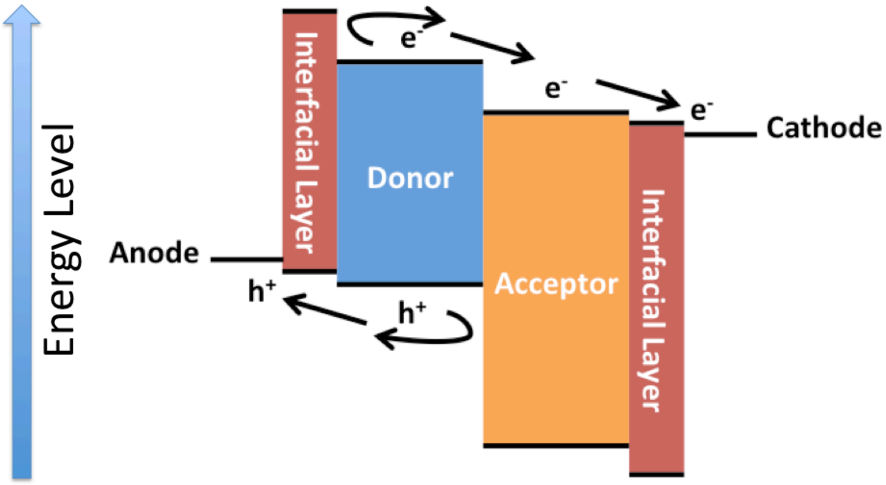

Figure 2.7: A typical cell design, where interfacial charge-transporting layers are introduced to minimise bimolecular recombination losses [28]. The barrier created by the large LUMO mismatch restricts electron movement from the donor to anode. Reducing the barrier between the donor and anode HOMO facilitates charge collection.

Interfacial layers are often placed between an electrode and the active layer. These can be hole-transporting layers (HTL), which are used for the polymer (donor) and the anode or electron-transporting layers (ETL), which are used for the fullerene-derivative (acceptor) and the cathode. Interfacial layers ensure a more optimal energy alignment between the anode and polymer HOMO, and the cathode and fullerene LUMO, enabling efficient charge extraction under forward bias. Figure 2.7 shows an example of its application in the energy level diagram. Considering only the anode, employing a suitable interfacial layer reduces the potential barrier between the HOMO of the polymer and anode. Another benefit of using interfacial layers is that chemical reactions between the active layer and electrode are limited. A good example is that many of the electrode materials used in OPV cells (such as Ag or Al) can diffuse into the polymer active layers. Any diffused ions can form centres of charge recombination. However, certain interfacial layers, such as metal oxides, can act as blocking layers, limiting this effect. Reversing the interface layers so that opposite charges are collected at the same electrode materials is known as ‘inverting’ the cell.

The most commonly reported HTL is poly(ethylene dioxythiophene) doped with polystyrene sulphonic acid (PEDOT·PSS) [29–33]. PEDOT·PSS is almost always used in roll-to-roll (R2R) devices [34, 35] due to its high conductivity (> 1 S.cm^{-1}) [31], and a HOMO difference of 0.2 eV with respect to commonly used poly(3-hexylthiophene-2,5-diyl) P3HT [36]. Another advantage of PEDOT·PSS is that it provides a planarised interface between the anode and the polymer active layer [32, 37]. This has the effect of providing a smooth surface for which the active layer can be deposited. A number of metal oxides show superior properties [38, 39], which include molybdenum oxide (MoO_3) [40], nickel oxide (NiO) [41] and vanadium oxide (V_2O_5) [42]. Metal oxide HTLs show improved stability, energy alignment and optical transparency but are normally deposited with thickness < 20 nm, which is difficult to obtain using an R2R coater.

One of the first reports of metal oxide layers in OPV cells was by Irwin et al. [41], who compared the performance of cells fabricated with and without a NiO interfacial layer. NiO was deposited by means of pulsed layer deposition (PLD), where an increase in FF and a smaller increase in J_{SC} was observed. The same effect could be achieved with other p-type interfacial layers with comparable work functions. Steirer et al. [43] demonstrated OPV cells made with solution processed NiO, giving a similar performance to those made with NiO using (PLD). It was possible to tune the work function of the solution processed NiO by thermal annealing and oxygen plasma treatment. In both of these cases, the improvements were equated to three reasons. Firstly, a decrease in R_S, which led to increased FF, compared to those made with PEDOT·PSS. Secondly, reduced absorption in the HTL. Finally, an improved hole transport due to the better match with the work function of ITO. Oh et al. [44] also investigated the use of tungsten oxide (WO_3) as a replacement for PEDOT·PSS. WO_3 gave increased FF and V_{OC} values as a result of decreased R_S. WO_3 layers thinner than 10 nm gave small islands of material instead of a continuous film.

ETLs are also mostly based on metal oxides and include titanium oxide (TiOx) [45, 46], zinc oxide (ZnO) [47–50] and caesium carbonate (Cs_2CO_3) [51, 52]. Formulations of TiOx and ZnO are R2R compatible and are often reported in OPV modules. However, in laboratory environments, a thin layer of lithium fluoride (LiF) [53] or calcium (Ca) [54] is still often used as an ETL. LiF, when combined with aluminium (Al), demonstrates the best performance among low work function metal electrodes[54]. Although Ca demonstrates slightly reduced PCE when used as an ETL compared to LiF, it is more stable [55].

Metal oxide ETLs using a range of deposition methods have been widely studied. Wang et al. [52] fabricated inverted OPV cells on polyethene naphthalate (PEN) substrates, using ZnO as an ETL. ZnO was applied via atomic layer deposition (ALD) at 80°C, giving a cell PCE of 4.18%. This performance was attributed to the blocking of hole diffusion and enhanced electron collecting efficiency to the electrode of indium oxide doped with tin (ITO) [In_2O_3·Sn]. In order to use ALD on plastic substrates, the process was optimised to enable a low-temperature deposition of ZnO. Another study by Hau et al. [56] used ZnO nanoparticles as an ETL in inverted OPV cells. The cells used the structure ITO / ZnO / P3HT·PCBM / PEDOT·PSS / Ag and achieved a PCE of 3.3%. Improved lifetime was also observed as a more stable material (Ag) was used as a top electrode. The physics of ZnO doping has been studied extensively as this is likely to play a crucial role in electron transport in these layers. Manor et al. [57] studied solution processable ZnO and reported its use as part of inverted OPV cells. These cells suffered from shunts originating from oxygen electron traps in the ZnO layer. Shunts could be removed with cell exposure to UV radiation, leading to increased FF and V_{OC}. Verbakel et al. [58] proposed that adsorbed oxygen on ZnO was desorbed by UV illumination, generating free charge carriers. It is believed that adsorbed oxygen acts as an electron trap, and its release enhances the concentration of mobile electrons. Bristow et al. [59] reported a similar effect, showing that light soaking was necessary to remove 'S-shaped' I-V characteristics.

Kim et al. [60] studied the use of TiOx as an ETL, realising the layer could serve an additional purpose – an enhancement in the optical absorption of the active layer. This layer was termed as an *optical spacer* as shown in Figure 2.8. Photons are incident from the glass side of the cell, with a proportion absorbed by the active layer. Reflected photons can interfere with those arriving at the active layer, reducing the total available for absorption. By carefully selecting the thickness of the optical spacer, destructive interference can be reduced, increasing the electric field intensity in the active layer. Kim et al. supported this observation by demonstrating an enhancement in the cell J_{SC}. Heeger et al. [61] studied this effect further. A solution-based sol-gel process applied 30 nm of TiOx between a P3HT·PCBM active layer and Al cathode. The external quantum efficiency (EQE) of cells was increased by 40% compared to those without the TiOx layer, as a result of the optical spacer effect.

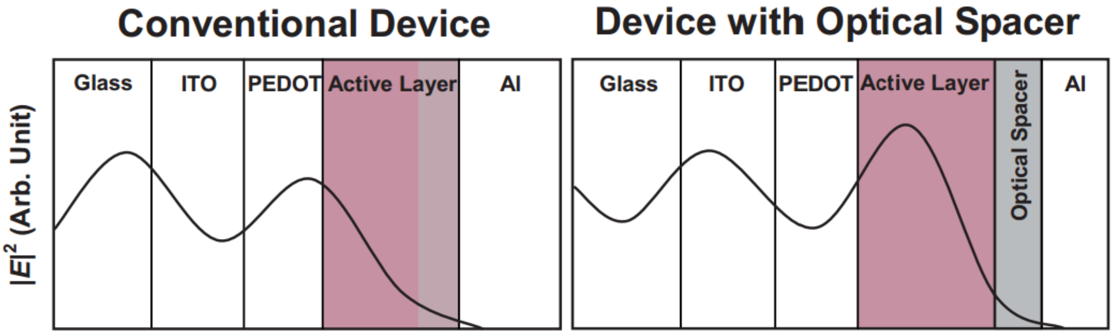

Figure 2.8: An optical spacer reduces the number of photons reflected from the Al electrode, back towards the active layer. Optical spacers inhibit the effect of deconstructive interference, increasing photon absorption [60].

2.2.3 Photon absorption through band gap engineering

One of the most widely reported polymers and one of the first materials used in BHJ active layers is P3HT. P3HT possesses an energy gap of 1.9 eV, resulting in a slight mismatch of peak absorption with the AM1.5G spectrum [62]. Therefore, P3HT is only able to absorb around 23% of solar flux photons [63]. Accounting for intrinsic losses arising from exciton separation, the optimum energy gap for a polymer in a BHJ cell has been calculated as 1.3 eV to 1.5 eV [17].

The first step towards increasing OPV cell performance is to increase the absorption efficiency (η_{abs}). Synthetic chemists can readily engineer the energy gap of the active layer polymer as there are many structural degrees of freedom, maximising the number of photons absorbed [23]. Energy gap engineering is not as achievable for fullerenes. When tuning the polymer energy gap, consideration needs to be given to ensure energy levels complement those of the fullerene for efficient charge separation, without decreasing V_{OC} [64].

One method for reducing the energy gap of polymers is to use a “push-pull” system, alternating electron-rich (donor – D) and electron-deficient (acceptor – A) monomers along a backbone. This method pulls π-electrons from the electron-rich monomer towards the electron-deficient monomer, increasing electron delocalisation across the donor-acceptor (D-A) polymer [65]. Combining electron-withdrawing and electron-donating groups, gives rise to new HOMO and LUMO (see Figure 2.9), narrowing the energy gap and absorbing lower energy photons [23]. In Figure 2.9, polymerisation of the donor (D) and acceptor (A) creates new HOMO and LUMO levels. The new HOMO has a higher energy and the new LUMO a lower energy level, leading to a narrowing of the energy gap.

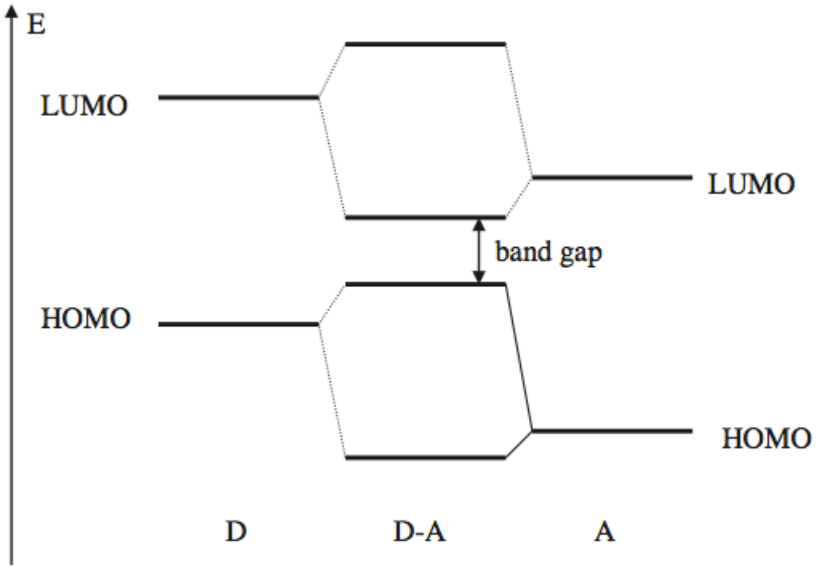

Figure 2.9: Combining electron-rich (donor – D) and electron-withdrawing (acceptor –A) groups leads to the formation a new molecule (D-A) with new HOMO and LUMO, reducing the energy gap [23].

2.3 Current state of the art donor-acceptor polymers

D-A polymers have attracted considerable attention because OPV cells with efficiencies in excess of 8% have been demonstrated [66–69]. High efficiencies were achieved after considerable optimisation of polymer structures and synthetic pathways. Performance depends upon the combination and sequence of donor and acceptor groups, as well as polymer chain length, side chains along the polymer backbone and backbone chain capping. This section provides a brief overview of active layer material development.

One of the earliest reports of OPV cells used a bilayer structure and led to a PCE of 0.04% for an active layer of poly[2-methoxy,5-(2'-ethyl-hexyloxy)-I,4-phenylene-vinylene] (MEH-PPV) and C_{60} fullerene (see Table 2.1) [70]. After the first report of the BHJ, MEH-PPV combined with $PC_{61}BM$, a soluble analogue of C_{60}, increased PCE to 2.9% [71]. During the 2000s, polyfluorenes were investigated for OPV use, primarily as they were being heavily researched at the time for use in organic light emitting diodes (OLED). Polyfluorenes gave maximum efficiencies of 4 to 6% due to their low HOMO, and high V_{OC} when combined with PCBM [72–74].

Table 2.1: Historically relevant polymers during OPV development.

Material	**PCE (%)**	**Additional information**
MEH-PPV·C_{60}	0.04	Evaporated bilayer heterojunction [70].
P3HT·$PC_{61}BM$	4.0	PCE of 6.5% was achieved for 1.5 mm x 1.5 mm active area [75].
P3HT·CdSe	2.1	Best report with CdSe nanocrystals [76].
PFDTBT·$PC_{61}BM$	3.0	PCE limited by small charge-carrier mobility [77].
PSiFDTBT·$PC_{71}BM$	5.4	Silicon replaced fluorine, increasing the charge-carrier mobility [77].
PSBTBT·$PC_{71}BM$	5.1	PSBTBT has increased absorption over PSiFDTBT [77].
PCDTBT·$PC_{71}BM$	6.1	PCDTBT has an internal quantum efficiency (IQE) approaching 100% [61].
PTB7·$PC_{71}BM$	9.2	A PFN interlayer was also used [78].
PCE10·$PC_{71}BM$	9.5	1, 8-diiodooctane (DIO) used for morphological control [79].

One of the first reported D-A polymers used in OPV cells was PCPDTBT. PCPDTBT combined with $PC_{61}BM$ in a BHJ gave an efficiency of 2.7%. Replacing $PC_{61}BM$ with higher absorbing $PC_{71}BM$ increased PCE to 5.5%. Critical for achieving this increased PCE was the use of the processing additive 1, 8-octanedithiol (ODT) [80, 81]. This material and the use of processing additives are discussed further in section 2.5.

Since the first D-A polymers, there have been numerous academic reports on OPV cell active layer materials. Generally fluorene, silafluorene, carbazole, benzo-dithiophene (BDT), cyclopenta-dithiophene (CPDT), dithieno-silol (DTS), indacenodithiophene (IDT) – electron-rich groups - are used as donor groups. Benzothiadiazole (BT), quinoxaline, thieno-pyrrole-dione (TPD), pyrrolo-pyrrole-dione (PPD) – electron-deficient groups – are used as acceptor groups [82]. Figure 2.10 shows some of the mentioned electron-rich and electron-deficient groups, often used in donor-acceptor co-polymers.

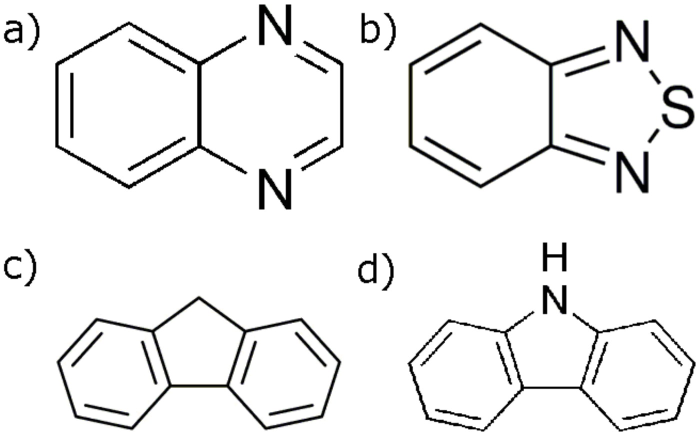

Figure 2.10: Shown are a) quinoxaline, b) benzothiadiazole, c) fluorene and d) carbazole monomer units.

BT is one of the most promising acceptor units due to its ability to preserve a low-positioned HOMO in the polymer. A low-positioned HOMO is not only beneficial for polymer stability, but also in gaining a high V_{OC} in final OPV cells. A lower lying HOMO makes polymers less susceptible to oxidation. Since the first report as an acceptor unit by Kitamura et al. [65], BT has been extensively used in a range of polymers. Table 2.2 summarises some of the significant reports for the performance increase with poly(CPDT-BT) [PCPDTBT] based solar cells [82].

In terms of similar materials, Svensson et al. [72] used BT with polyfluorene to synthesise poly{[2, 7-(9-(20-ethylhexyl)-9-hexyl-fluorene])-alt-[5, 50-(40, 70-di-2-thienyl-20, 10, 30-benzothiadiazole)]} (PFDTBT). Derivatives of PFDTBT have given PCEs of 2 to 3%, when combined with $PC_{61}BM$. This group of materials is limited by charge-carrier mobility, ultimately leading to low FF. Therefore, in order to improve the hole-transporting properties of PFDTBT, the fluorine (F) was substituted with silicon (Si) to give poly[(2, 7-dioctylsilafluorene)-2, 7-diyl-alt-(4, 7-bis(2-thienyl)-2, 1, 3-benzothiadiazole)-5, 5'-diyl] (PSiFDTBT), and when combined with $PC_{71}BM$ gave a PCE of 5.4% [74]. In order to replicate the same charge-carrier mobility property of PSiFDTBT, but with increased absorption, poly((4, 4-octyldithieno(3, 2-b:2’, 3’-d)silole)-2, 6-diyl-alt-(2, 1, 3-benzothiadiazole)-4, 7-diyl) (PSBTBT) was synthesised, giving a PCE of 5.1% when combined with $PC_{71}BM$ [83].

Table 2.2: PCE for different material systems including variants of PCPDTBT.

Material	**PCE (%)**	**Other information**
$PCPDTBT \cdot PC_{61}BM$	2.7	First report of this material [80].
$PCPDTBT \cdot PC_{71}BM$	3.2	$PC_{71}BM$ increased absorption at shorter wavelengths [80].
$PCPDTBT \cdot PC_{71}BM$	5.1	DIO was used as a processing additive to control morphology [84].
$PCPDTBT \cdot PC_{71}BM$	5.5	ODT inclusion increased mobile-carrier lifetime from a change in morphology. ODT also had the effect of increasing π-π stacking [81].
PCPDTBT·CdSe	2.7	CdSe nanocrystals. This is the best reported hybrid cell using PCPDTBT [76].

Poly[N-9”-hepta-decanyl-2, 7-carbazole-alt-5, 5-(4’, 7’-di-2-thienyl-2’, 1’, 3’-benzothiadiazole) (PCDTBT) is another OPV material showing a reasonably high PCE of 6.1% when combined with $PC_{71}BM$ [85]. PCDTBT’s lower HOMO ensures the material’s relative stability in ambient conditions, as well as decreasing the energy gap, thus increasing the V_{OC}. An internal quantum efficiency (IQE) approaching 100% was reported for this material, meaning that each photon absorbed results in separated charge carriers [61].

Another OPV material shown to give high PCE is poly([4, 8-bis[(2-ethylhexyl)oxy]benzo[1, 2-b:4, 5-b’]dithiophene-2, 6-diyl] [3-fluoro-2-[(2-ethylhexyl)carbonyl] thieno[3, 4-b]thiophenediyl]) (PTB7), due to its low HOMO level and absorption into the infrared part of the spectrum. PTB7 demonstrated a PCE of 9.2% when combined with $PC_{71}BM$ in an inverted OPV cell [78]. Finally, poly[(4, 8-bis-(2-ethylhexyloxy)-benzo[1, 2-b:4, 5-b'](dithiophene)-2, 6-diyl-alt-(4-(2-ethylhexanoyl)-thieno [3, 4-b]thiophene)-2, 6-diyl] (PBDTTT-EFT) or PCE10 shows lower HOMO and LUMO levels and increased efficiencies compared to PTB7, but with reduced stability. PCE10 demonstrated an efficiency of 9.5% when combined with $PC_{71}BM$ and using the 1,8-diiodooctane (DIO) processing additive [66, 79]. Figure 2.11 shows the molecular structures for some of the discussed materials.

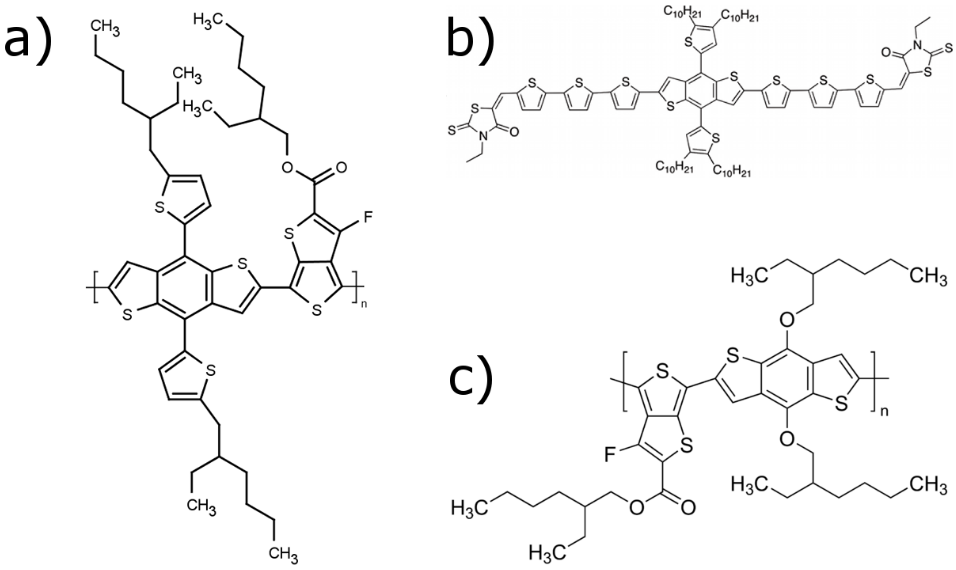

Figure 2.11: Shown are a) PCE10, b) DR3TDBTT and c) PTB7 polymers.

An emerging field of research is hybrid solar cells, combining organic semiconductors with novel materials such as nanoparticles [86]. For example, the fullerene is substituted with organic nanocrystals in a setup known as a hybrid solar cell [87]. Nanocrystals such as cadmium selenide (CdSe) or ZnO are attractive in that they have the potential of tunable energy gaps, high absorption coefficients and high charge-carrier mobilities [88]. Despite these characteristics, solar cell PCEs using nanocrystals remains lower than for those using fullerenes. PCPDTBT combined with CdSe nanocrystals gave a PCE of 2.7%, due to the polymer's increased photon absorption and thus higher J_{SC} [76].

OPV cells using small molecules instead of polymers have drawn much attention since they can be processed using thermal evaporation [89]. Heliatek GmbH in Germany focus exclusively on small molecule OPV cells using evaporative processes and have a verified efficiency of 12.3% [11].

Solution processable small molecules were for a long period considered difficult to treat owing to their intermolecular electron delocalization, which is known to result in molecule nucleation, causing inhomogeneous films [90]. Despite the perceived poorer solution processability, recent reports showed that oligothiophene derivatives exhibit high organic field-effect transistor (OFET) hole mobilities over 1 $cm^2.V^{-1}.s^{-1}$ [91, 92]. PCEs of 6.8% have been reported for OPV cells using vacuum-deposited 2-{[7-(4-N, N-diphenylaminophenylen-1-yl)-2, 1, 3-benzothiadiazol-4-yl]methylene}malononitrile (DPDCPB) and C_{70} [93], and 8.1% for solution-processed DR3TBDTT with $PC_{71}BM$ [94]. Solubility issues have been overcome by using appropriate alkyl substituents and relatively long conjugation systems of 6 to 10 units [94]. One of the drawbacks is that their synthesis typically requires an additional step, increasing reaction times and costs. Small molecule OPV cells have higher $V_{OC,}$ wider energy gap values and similar FF when compared to their polymer equivalent, as a result of shorter conjugation lengths [95]. Table 2.3 summarises the best performing small-molecule based OPV cells.

Table 2.3: Historically relevant small molecules during OPV development.

Material	**PCE (%)**	**Other information**
Pentacene·C_{60}	1.5	Vacuum deposited [96].
CuPc·C_{60}	3.7	Vacuum deposited [97].
NDT(TDPP)$_2$·$PC_{61}BM$	4.1	Spin-cast [98].
DTDCPB·C_{70}	6.8	Best reported vacuum deposited small-molecule OPV [93].
DR3TBDTT·$PC_{71}BM$	8.1	Best reported PCE for spin-cast small-molecule OPV [94].

2.4 Synthetic pathways for Donor-Acceptor polymers

There are many reported chemical routes for the synthesis of semiconducting polymers. The two synthetic routes normally used for OPV polymers are Stille- and Suzuki-coupling. Each one has its advantages and disadvantages.

2.4.1 Stille polymerisation

Stille polymerisation reaction (shown in Figure 2.12) is the most commonly used to synthesise alternating D-A polymers. It owes its popularity to its modular nature where monomers can be alternated, or arranged in block or random structures. Longer reaction times lead to greater polymer molecular weights. The flexibility and reliability of this synthetic route mean it is commonly used for engineering new conjugated polymers, which may be used in OPV cells [99–101].

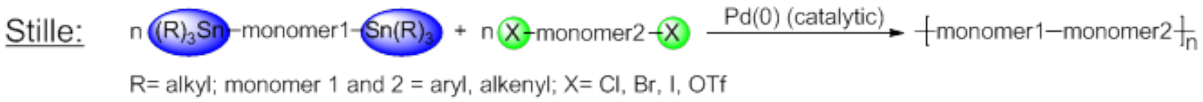

Figure 2.12: A schematic of Stille polymerisation reaction [102, 103].

Stille polymerisation has a number of problems. As the reaction uses a Pd catalyst, it is sensitive to variations in stoichiometry and exposure to air. Some of the materials used during polymerisation, such as organostannane compounds, are highly toxic. Chlorinated aromatic solvents are used as a standard, which are also toxic and have high boiling points. When considering the life cycle of the polymer, the use of such solvents necessitates high-energy inputs to recycle the material [101].

2.4.2 Suzuki polymerisation

Suzuki polymerisation (shown in Figure 2.13) is another condensation reaction similar to Stille in that it requires a Pd catalyst. This synthetic route is environmentally preferential as it uses organoboron compounds, which are less toxic than organostannanes. Suzuki polymerisation is more suited for synthesis on an industrial scale [104].

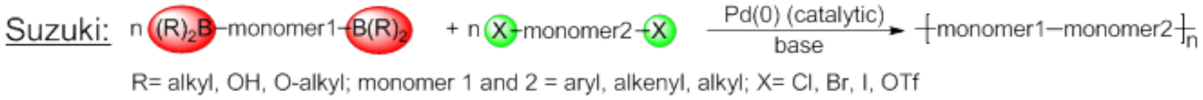

Figure 2.13: A schematic of Suzuki polymerisation [102, 103].

Suzuki polymerisation is somewhat more complex, with difficulties in mixing initial monomer units and prevention of their condensation into cyclic polymers. Further reagents and processing may be required, increasing reaction times and costs [101].

2.4.3 Direct heteroarylation polymerisation

The Stille and Suzuki polymerisation routes rely upon C-C coupling reactions. Direct heteroarylation (also direct arylation) cross-couples aryl C-H bonds directly (shown in Figure 2.14). The advantage of this polymerisation route is that there is no need to prepare the monomers using boron or tin based compounds, reducing the toxicity of this procedure. Only one of the monomers is functionalised, as opposed to two. If assuming 100% yield between each step, direct heteroarylation requires two fewer steps than for Stille and Suzuki coupling, reducing the required reagents and time. This synthetic pathway has been shown to fabricate polymers with molecular weights that are comparable or higher than those made using Stille polymerisation. However, few reports exist of its use for conjugated polymers. In one example, P3HT with a molecular weight of 30 kDa was synthesised with a yield of 99% [101, 105].

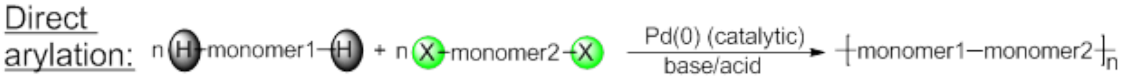

Figure 2.14: A schematic of direct-arylation polymerisation [101, 103].

2.5 PCPDTBT

The focus of this thesis is on the PCPDTBT material; utilising electron-rich cyclopentadithiophene (CPDT) donor and electron-deficient benzothiadiazole (BT) acceptor. PCPDTBT is a "push-pull" polymer with increased π-electron delocalisation, with its structural formula shown in Figure 2.15. Scharber and the group at Konarka GmbH in Europe used Stille coupling to produce the material, first reported in 2008 [80].

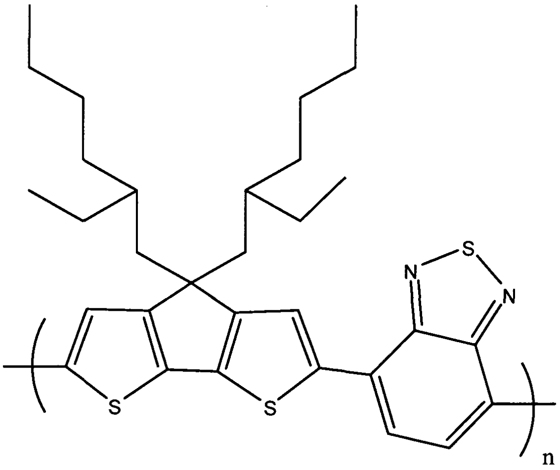

Figure 2.15: The chemical structure of PCPDTBT. The polymer consists of two repeating monomer units – CPDT and BT. The branched 2-ethyl-hexyl side chains on the CPDT unit assist with dissolution [80].

2.5.1 Optical and material properties

Initial cyclic voltammetry (CV) tests by Scharber et al. [80] deduced HOMO and LUMO of 5.3 eV and 3.57 eV for PCPDTBT, giving this material an electrochemical energy gap of 1.73 eV. Optical absorption data suggested an even lower energy gap, with an onset of absorption occurring at 1.4 eV in the solid-state. Electrochemical energy gaps are higher due to charge-barriers between the analyte, which is contained within an electrolyte, and probe interfaces [106]. Other factors that contribute to higher electrochemical energy gaps are the use of a reference material for calibration, and possible probe contamination from other analytes.

PCPDTBT also showed a peak absorption shift of 70 nm between solution and solid-state films, a phenomenon known as solvatochromism. Solvatochromism is observed in conjugated polymers with strong interchain and intrachain actions and is a sign of 2D stacking [77, 107]. Figure 2.16 shows the absorbance and EQE for PCPDTBT blended with $PC_{61}BM$ or $PC_{71}BM$. PCPDTBT shows broad absorption across the visible region from 400 nm up to 800 nm. The absorption peak about 740 nm is attributed to PCPDTBT π-π^* transitions, and the one at approximately 480 nm to HOMO-LUMO transitions in PCBM [108]. $PC_{71}BM$ exhibits greater absorption at shorter wavelengths, resulting in greater EQE from 400 to 600 nm, as seen in Figure 2.16.

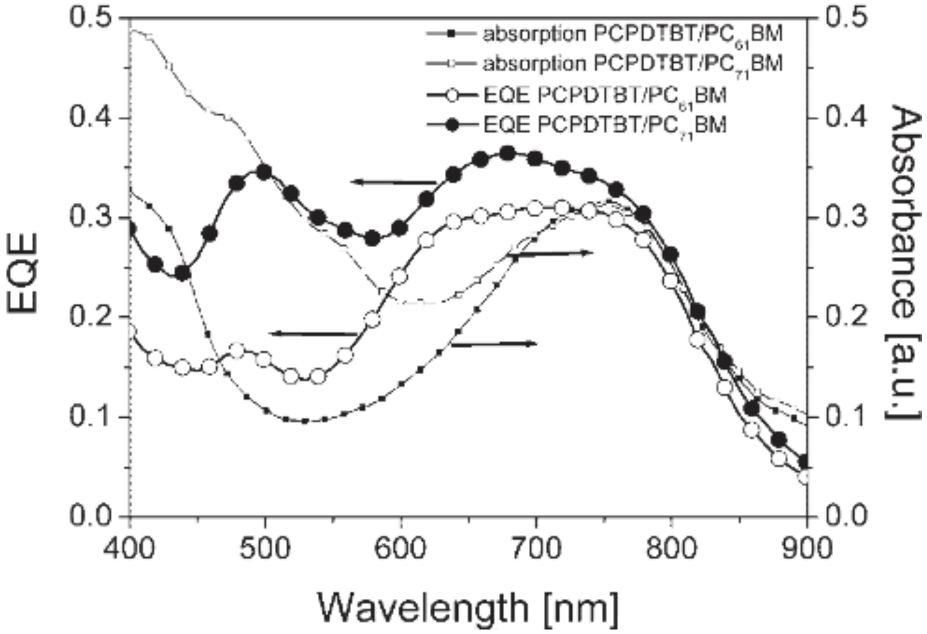

Figure 2.16: Absorbance spectra of PCPDTBT with PC$_{61}$BM and PC$_{71}$BM respectively. PC$_{71}$BM shows increased absorption at shorter wavelengths when compared to PC$_{61}$BM [80].

2.5.2 Electrical properties

A commonly used figure of merit for organic semiconductors is charge carrier mobility. The three most commonly used techniques for characterising mobility are: organic field effect transistors (OFET) biased in the saturation region; time of flight (TOF); and space-charge limited current (SCLC) devices [109].

OFET devices have become established as an experimental gauge for probing charge mobility, carrier density and doping levels in organic thin films and nanostructures. Their fabrication and characterisation are reported in most significant papers on PCPDTBT, listed in Table 2.2. OFET devices can be fabricated using different configurations of the source (S), drain (D) and gate (G) contacts (shown in Figure 2.17), each with their advantages and disadvantages. When fabricating OFET devices, both source and drain contacts should be Ohmic and with negligible resistance with respect to the resistance of the organic material. Bottom-gate top-contact OFET devices exhibit reduced contact resistances compared to bottom-gate bottom-contact, due to an improved interface between the electrodes and organic material [110]. Bottom-gate bottom-contact OFET devices are affected by morphological disorder close to the contact edges, due to processes underpinning organic material deposition.

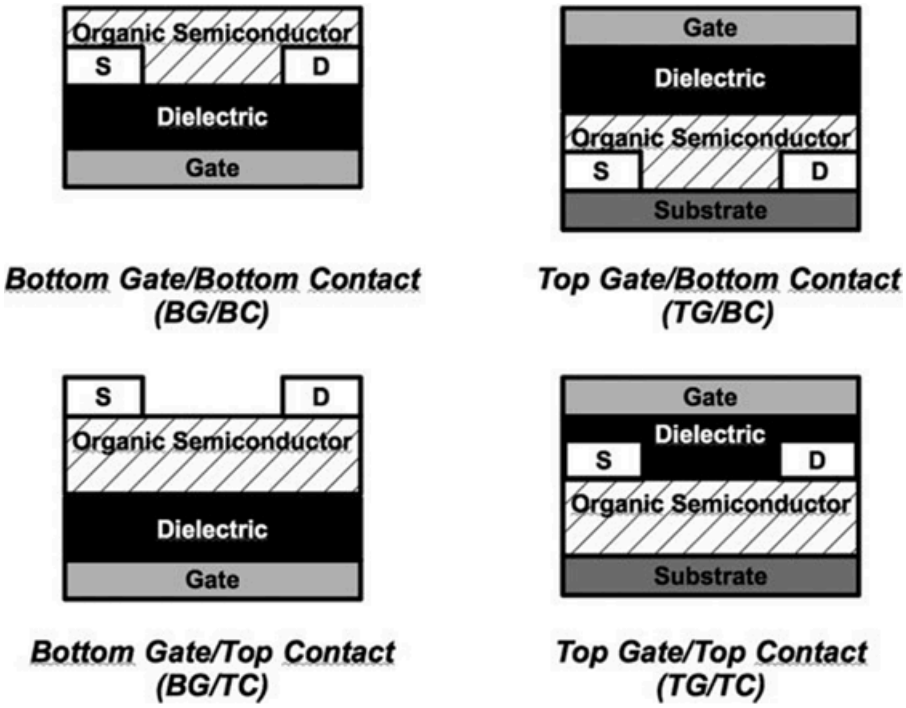

Figure 2.17: Shown are the four possible OFET structures. Current flows from the source to the drain, in a direction parallel to the gate surface. Bottom-gate top-contact OFET devices provide the highest charge mobility values due to better interfaces between the source and drain, and the organic material [110].

OFET devices are controlled by two voltages. A voltage is applied across the source and drain contacts, however an intrinsic semiconductor has very few charge carriers. It is only when an additional voltage is applied between the gate and the drain, that charge is injected into the semiconductor from the source [92, 110]. Increasing the gate voltage increases the number of injected charges. Upon increasing V_D, the current also increases until pinch-off, when the current in the semiconductor saturates [111]. The charge transport characteristics of organic materials used in OFET devices are determined from output and transfer characteristics. Output characteristics are determined by measuring the output current (drain current) with respect to the output voltage (drain-source voltage) (I_D vs. $V_{D/S}$). Transfer characteristics are determined by measuring the output current with respect to gate voltage (I_D vs. V_G).

Zhang et al. [112] fabricated bottom-gate bottom-contact OFET devices made from drop-cast PCPDTBT, demonstrating a maximum hole mobility of 0.17 $cm^2.V^{-1}.s^{-1}$, and an on/off ratio of 10^5. More recently OFET mobilities of up to 3.3 $cm^2.V^{-1}.s^{-1}$ were achieved by Tsao et al. [113]. Increased mobility was attributed to the polymer backbone and the direction of π-π stacking being along the plane of the film [114]. Figure 2.18 shows a schematic of π-π stacking. These OFET devices were also fabricated using the drop-cast method, with the output characteristics and transfer curve shown in Figure 2.19. A number of reasons were attributed to this high mobility value, including optimised morphology and crystallinity. Crystallinity improved with molecular weight, with alkyl side chains facilitating denser polymer packing. Few reports exist of polymers with short alkyl side chains giving high OPV performance. In the case of Zhang et al. [112], hexdecyl ($C_{16}H_{33}$) side chains were used. This is due to the poor solubility of polymers with short alkyl side chains, limiting the concentration of the material in solvents. Ultimately, this imposes a restriction on the final film thickness, limiting the absorption of any OPV cells made from PCPDTBT with alkyl side chains.

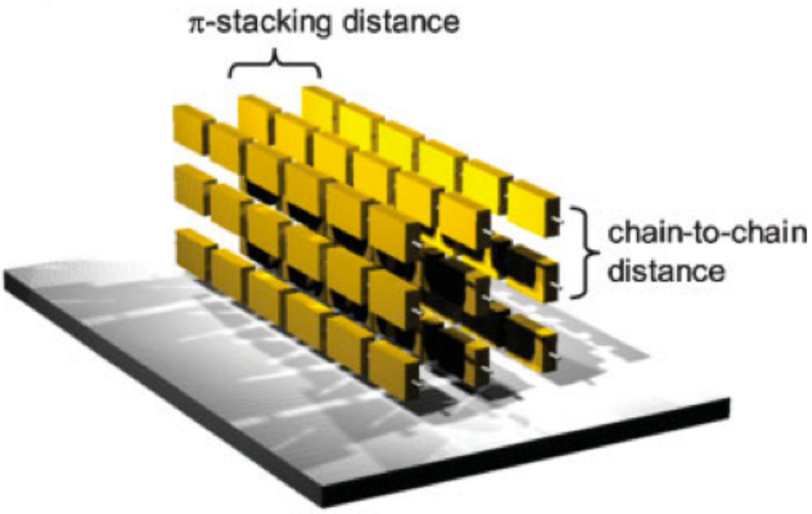

Figure 2.18: A schematic of the interpreted PCPDTBT π-π stacking. The polymer backbone and π-π stacking orientated in the film plane led to the high hole mobilities reported by Tsao et al. [113, 114].

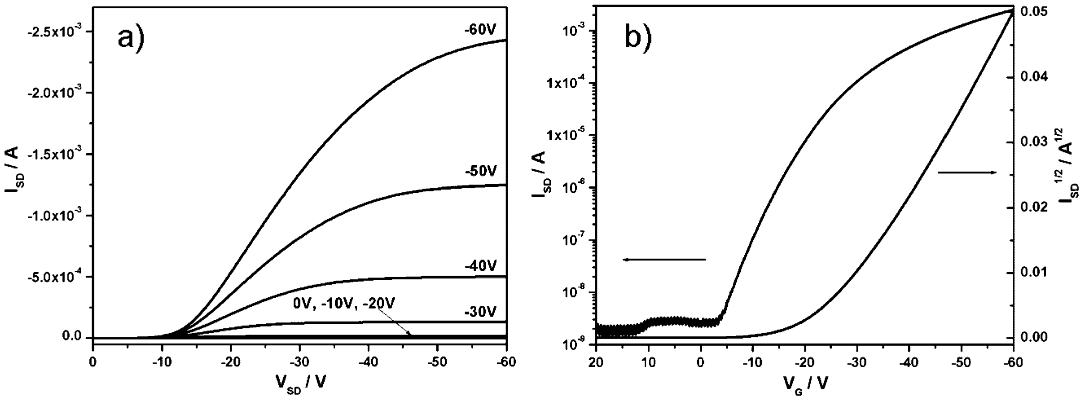

Figure 2.19: Shown are the output characteristics of CPDT-BT based OFET by Tsao et al. for different gate voltages (a). The transfer curve for a drain voltage of -60 V is shown in (b) [113].

PCPDTBT based on ethyl-hexyl side chains demonstrated a hole mobility as high as 2 x 10^{-2} $cm^2.V^{-1}.s^{-1}$. However, this did not account for uncorrected contact resistance of the source and drain [80]. The actual value was therefore expected to be higher. The work of Kettle et al. [107] demonstrated a hole mobility of 3 x 10^{-3} $cm^2.V^{-1}.s^{-1}$, for PCPDTBT with a substantially lower molecular weight of M_n = 15,000, as it was synthesised using Suzuki coupling. Peet et al. [81] reported a hole mobility of 1 x 10^{-3} cm^2 V^{-1} s^{-1}, using a greater molecular weight material of M_n = 50,000, also with ethyl-hexyl side chains.

Space-charge limited current (SCLC) devices provide an alternative method of measuring hole mobility. In OFET devices, the current travels in the plane of the film, which is parallel to the substrate. Current flow therefore differs significantly to that seen in OPV cells. SCLC devices, therefore, provide a more relevant value for charge-carrier mobilities, with respect to OPV cells. In undoped organic materials, the current flow depends upon injected charge carriers [115]. Therefore, for SCLC measurements, one electrode must efficiently inject the required charge carrier, while the other must block injection of charge carriers of the opposite polarity [109]. Assuming an infinite number of injected charges, leading to a drift current far exceeding the diffusion current, the organic material is space-charge limited (SCLC) [116, 117]. Current is, therefore, field dependent allowing the calculation of charge mobility for the bulk organic material. The only known report of PCPDTBT mobility measurements using SCLC devices was by Kettle et al. [118] A maximum hole mobility of 2 x

10^{-5} $cm^2.V^{-1}.s^{-1}$ was demonstrated for PCPDTBT. This value did not account for imperfect injection and was, therefore, deemed an underestimate. Mobilities measured using SCLC instead of OFET devices are lower, due to charge transport through a more disordered bulk material [115, 119].

2.5.3 Solar cell properties

In one of the first reports by Mühlbacher et al., PCPDTBT combined with $PC_{71}BM$ demonstrated a PCE of 3.2%, a J_{SC} of 11 $mA.cm^{-2}$, a FF of 47% and a V_{OC} of 0.650 V (see Figure 2.20). While the OPV cell possessed broad absorption, the EQE was only shown to be over 25% between 400 nm and 800 nm. The EQE peaked at around 38% between 700 and 800 nm, where the peak absorption of PCPDTBT occurs. PCPDTBT based OPV cells with $PC_{61}BM$ and $PC_{71}BM$ were shown to have a V_{OC} of 0.65 to 0.70 V respectively, which is to be expected based on the polymer HOMO and fullerene LUMO [120]. Considering that the charge-carrier mobility gave acceptable J_{SC}, the limited PCE was down to a low FF. The low FF was attributed to reduced free charge lifetimes and charge recombination due to unfavourable polymer-fullerene morphology [121]. This low FF was observed by applying a large negative bias, which generated a large photocurrent. It was concluded that PCPDTBT's absorption properties make it capable of generating sufficient free charge carriers to give a PCE of 7%, if the morphology can be optimised [80].

A major leap forward was reported by Heeger's group at Santa Barbara University, who solution processed PCPDTBT·$PC_{71}BM$ from chlorobenzene with the addition of a processing additive. Processing additive use is discussed further in section 2.5.4 but is shown to improve the active layer morphology substantially. In one work by Peet et al. [81], ODT gave the best performance by increasing the J_{SC} and FF. On average, cells had a V_{OC} of 0.62 V, J_{SC} of 16.2 $mA.cm^{-2}$, FF of 55% and a PCE of 5.2% (the highest was 5.5%).

Almost all works by Scharber, Scherf and Heeger groups have used Stille-coupled PCPDTBT. PCPDTBT has also been synthesised using direct heteroarylation polymerisation, where polymers with M_n of up to 40,000 were synthesised with yields up to 80%. However, no working OPV cells were demonstrated [105].

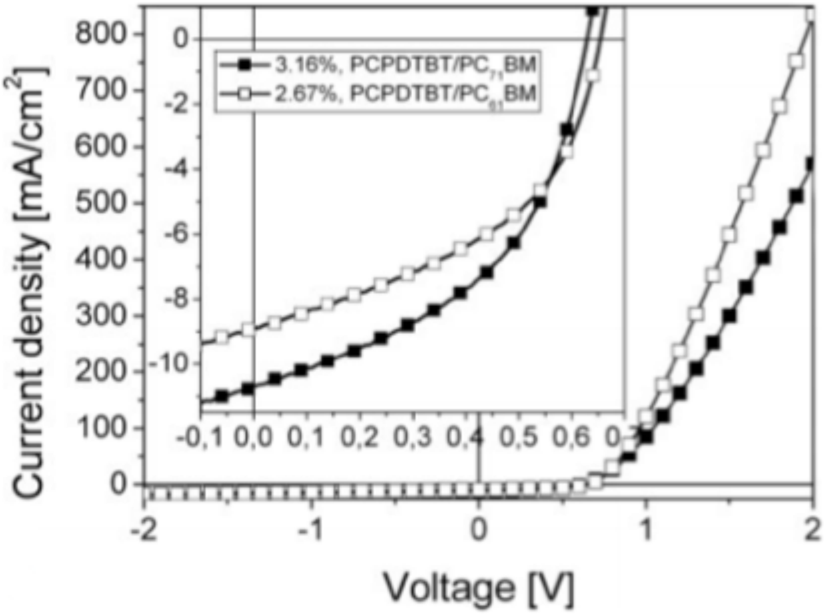

Figure 2.20: I-V characteristics of PCPDTBT with $PC_{61}BM$ or $PC_{71}BM$ as first reported by Scharber et al. [80].

The only other known work on PCPDTBT synthesis was by Kettle et al. [107], who reported the optimisation of OPV cell performance from PCPDTBT with 2-ethylhexyl side chains, prepared by Suzuki coupling. A maximum PCE of 4.5% was achieved. Discussed were the importance of polymer purification procedures, and the optimisation of cell performance by changes in material blend concentration, active layer thickness, and film drying conditions.

2.5.4 Control of the morphological properties

Thermal annealing is a simple technique for further increasing cell PCE for certain polymers. The heat input purges residual casting solvent, assisting with morphological control, enhancing crystallinity. For example, P3HT·PCBM solar cells show significant improvement for two reasons [122]. Firstly, the increased crystallinity of P3HT due to in-plane π–π stacking leads to efficient hole transport. Secondly, annealing causes PCBM aggregation in active layers, providing an enhanced pathway for electron transport [123]. Many analytical techniques have been used to study these changes in greater depth including Raman microscopy [124], energy filtered transmission electron microscopy (EFTEM) [125] and spectroscopic ellipsometry [126].

Another strategy used for morphological control is solvent vapour annealing (SVA) [127]. Tang et al. [128] treated films of P3HT·PCBM with the vapours of two different solvents. An initial tetrahydrofuran (THF) vapour application led to PCBM forming aggregates with sizes of approximately 30 nm. A second vapour treatment with carbon disulphide (CS_2) reduced the PCBM aggregates size to approximately 20 nm while substantially increasing P3HT crystallinity. This approach led to a cell PCE of 3.9% compared to 3.2% given by thermal annealing, demonstrating the technique's viability.

PCPDTBT performance was shown to decrease upon thermal annealing, with no known reports of SVA treatment. No SVA reports could be due to PCPDTBT's amorphous nature [129], or PCBM aggregation scales exceeding the exciton diffusion path length in PCPDTBT [130].

Another method of modifying the morphology is to use solution-based processing additives. The inclusion of small concentrations (typically 2 - 3% of the final solution) of functionalised alkanes assists with morphological control. Additives were firstly found to be useful in P3HT·PCBM based cells, and are also effective in PCPDTBT-based cells.

Peet et al. [81] demonstrated a cell PCE of up to 5.5%, for cells made with PCPDTBT·$PC_{71}BM$, cast from chlorobenzene and ODT (2.5%), due to increased J_{SC} and FF. The inclusion of ODT increased the EQE of PCPDTBT between 400 nm and 800 nm by a factor of 1.6. ODT led to an increase in charge-carrier lifetimes, thus photocurrent [131]. A similar study with ODT in P3HT·$PC_{61}BM$ OPV cells attributed the higher performance to increased crystallinity of the P3HT phase in the BHJ [81]. However, PCPDTBT was not shown to exhibit a high crystalline structure with or without functionalised alkane additives. In another study by Lee et al. [84] DIO was used with PCPDTBT·$PC_{71}BM$ based OPV cells, increasing PCE from 3.4% to 5.1%. As with other reports on additives, DIO increased charge lifetime, from 500 ns to 3 μs, leading to increased FF in solar cells [132].

Processing additives are selected for two primary reasons. Firstly, their boiling point must be greater than the host solvent. Secondly, one of the active layer components must be more soluble than the other. For most polymers (PTB7, PCDTBT, PCPDTBT), DIO was shown to lead to the highest performing OPV cells. Functionalised alkanes do not react chemically with the polymers nor $PC_{61}BM$ or $PC_{71}BM$, but dissolve PCBM selectively [84]. When a polymer-fullerene blend is spin-cast, several phases are formed. Since the processing additive has a higher boiling point than the host solvent, the PCBM remains in solution longer than the polymer [133]. The polymer formed a solid-state structure while the PCBM was still in solution, increasing the time available to form an optimum morphology. Figure 2.21 schematically shows how additives only solubilise the PCBM and not PCPDTBT. This selective solubility gives a level of control over the morphology. The morphology of PCPDTBT·$PC_{71}BM$ films in OPV cells using DIO was investigated using EFTEM. Areas showing energy losses were found to be rich in $PC_{71}BM$. Cells processed without DIO showed highly intermixed small-scale phase separation, whereas cells processed with DIO showed purer polymer and fullerene phase with domain sizes of 10 to 20 nm. The coarsening of the blend morphology indicated stronger polymer aggregation, and higher interchain and intrachain order within the polymer aggregates [132].

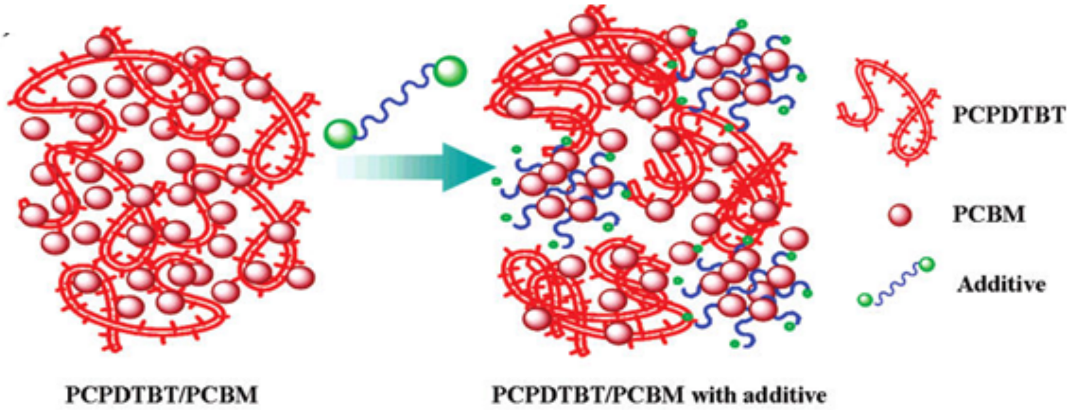

Figure 2.21: A schematic of how additives such as ODT and DIO selectively dissolve PCBM [84].

2.5.5 D-A-D polymers based on CPDT and BT

One novel attempt by Horie et al. [134] to improve solar cell performance was to use a polymer titled 'PC2B1'. PC2B1 based upon CPDT and BT units had a repeating structure of CPDT-BT-CPDT along the backbone. Repeating structures of donor-acceptor-donor (D-A-D) have been trialled for other materials, but this was the first report for CPDT-BT based polymers. Figure 2.22 shows the monomer of CPDT-BT-CPDT. An oligomer with 2-ethylhexyl side chains on CPDT with a ratio of CPDT:BT = 2:1 units (C2B1 from here onwards) led to a polymer with high solubility and high molecular weight polymer (M_n > 100,000). OFET devices demonstrated a maximum hole mobility in excess of 10^{-2} $cm^2.V^{-1}.s^{-1}$. This mobility is significantly higher than the PCPDTBT alternating copolymer (CPDT·BT = 1:1) with the same alkyl groups.

Although PC2B1 gave a higher hole mobility, its energy levels were not as optimal with respect to the HOMO and LUMO of PCBM, leading to slightly increased charge recombination. The main drawback of PC2B1 was a non-optimum morphology as a result of low molecule solubility. A solar cell performance of 2.3% compared to 2.1% (for PCPDTBT) was reported [134].

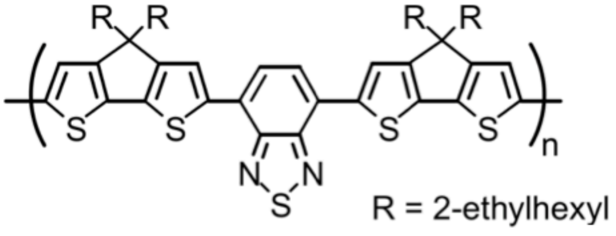

Figure 2.22: A donor-acceptor-donor (D-A-D) polymer based on CPDT-BT-CPDT, in a ratio of two parts electron-rich to one part electron-withdrawing groups [134].

2.6 Cross-linked active layer materials for OPV cells

Even though controlling factors such as casting solvent or annealing temperature can optimise the morphology of an OPV active layer, it exists in a metastable condition. Over extended operating times, maintaining a stable peak performance is difficult. Peak performance instability is due to phase segregation of blend components, accelerated with prolonged heat exposure [123].

Overcoming the morphological instability can be realised through active materials that cross-link through either photo- or thermal-initiation, and have been reported for numerous materials [135]. These reports include the development of a photo-cross-linkable derivative of the thieno[3, 4-c]pyrrole-4, 6-dione (TPD)-based polymer, which showed improved thermal stability during lifetime testing [135, 136]. Another attempt to cross-link active layer materials was undertaken by Cheng et al. [137, 138], who used fullerene derivative with thermally activated styryl cross-linkers. The group achieved improvements in PCE and lifetime for inverted OPV cells.

Cross-linking has not only been shown to increase stability, but reports have also shown increased transverse hole mobility. Increased stability through cross-linking also has the effect of decreasing the susceptibility of material dissolution. Other materials can, therefore, be solution processed without removing already cast cross-linked layers [139]. Shown in Figure 2.23 are two cross-linkable analogues of P3HT. Poly(3-(5-hexenyl)thiophene [P3HNT] and bromine-functionalised P3HT (P3HT-Br) [140], are cross-linked by thermal initiation between the π-bond and bromine. The cross-linking mechanism originates from the π-bond of P3HNT and the bromine atom of P3HT-Br.

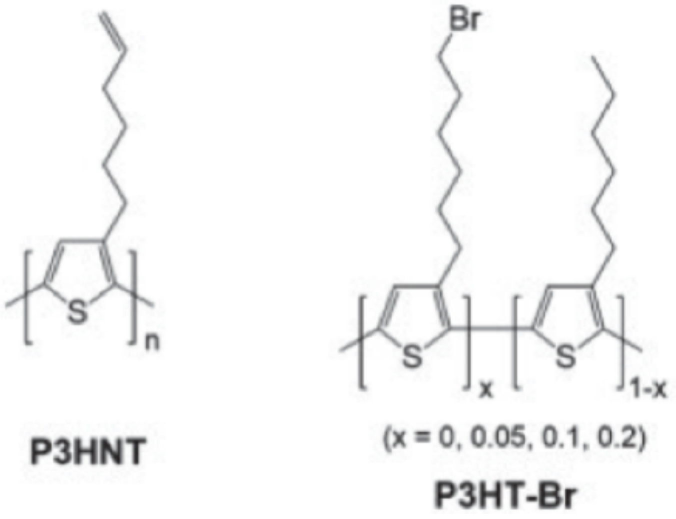

Figure 2.23: Two cross-linkable analogues of P3HT. Poly(3-(5-hexenyl)thiophene [P3HNT] and bromine-functionalised P3HT (P3HT-Br) [140].

2.7 Degradation in OPV cells

Optimising OPV cell lifetimes requires an understanding of device degradation during operation. OPV cells that rely on the interplay between several layers are sensitive to the smallest of changes, making their degradation study critical. In the following sections, the degradation mechanisms for the different layers are examined with a summary of the methods used for their monitoring.

2.7.1 Lifetime consensus standards

In 2008, several major research groups identified the lack of coherency for publishing OPV stability measurements, and developed guidelines based upon consensus. These guidelines were a culmination of three years of discussions at the International Summit on OPV Stability (ISOS) [141].

Most common testing protocols fit under “ISOS-L-1/2/3 Laboratory”, which is laboratory weathering of OPV cells under continuous illumination. Numbers 1/2/3 refer to basic, intermediate or advanced testing with the specifications shown in Table 2.4.

Table 2.4: Outlined are the testing protocols for ISOS-L-1/2/3 Laboratory. I-V sweep conditions are described for illuminated OPV cells. Light source, temperature and humidity are defined. Between characterisation under a solar simulator, the OPV cell is biased either at the maximum power point (MPP) or left disconnected from an external circuit [141].

	ISOS-L-1 Laboratory	**ISOS-L-2 Laboratory**	**ISOS-L-3 Laboratory**
Light source	Simulator	Simulator	Simulator
Temperature	Ambient	65/85°C	65/85°C
Relative-humidity (R.H.)	Ambient	Ambient	Near 50%
Environment/setup	Light only	Light, temperature	Light, temperature, R.H.
Characterisation light source	Solar simulator	Solar simulator	Solar simulator
Load	MPP or disconnected	MPP or disconnected	MPP

ISOS-L-1 Laboratory outlines a basic testing procedure, where an OPV cell is continuously illuminated with simulated light closely matching the AM1.5G spectrum (Class B solar simulator is acceptable). No other parameter, such as temperature or humidity, is controlled. Between characterisation, the cell may be left disconnected, or biased at its calculated maximum power point (MPP). ISOS-L-2 Laboratory requires control and recording of illumination and temperature. ISOS-L-3 Laboratory requires control and recording over illumination, temperature and humidity.

2.7.2 Illumination Source

OPV testing has been accomplished using a variety of light sources including natural sunlight [63, 141]. The illumination source is important since different technologies have different spectra and can, therefore, influence OPV performance. The UV part of the spectrum, from 250 to 400 nm, can induce chemical reactions such as photo-oxidation and photo-bleaching [142]. Wavelengths in the infrared region can lead to heating of the OPV cell, leading to morphological changes [123].

The most common light sources for accelerated testing are sulphur plasma, tungsten halogen, xenon arc and metal halide. Sulphur plasma and tungsten halogen provide an excellent AM1.5G match in the visible spectrum but do not overlap well at UV wavelengths. Tungsten halogen suffers from difficulties in achieving spatial uniformity [141].

Xenon arc and metal halide lamps with suitable filters provide an excellent AM1.5G match. The output spectra of both need monitoring, as UV emission from xenon arc lamps changes with operation life. Figure 2.24 shows the spectral overlap of AM1.5G, xenon arc and metal halide lamps with daylight filters. The presence or absence of certain parts of the spectrum affect degradation pathways [141]. ISOS standards allow for testing with any of the light sources discussed (metal halide, xenon arc, tungsten halogen and sulphur plasma).

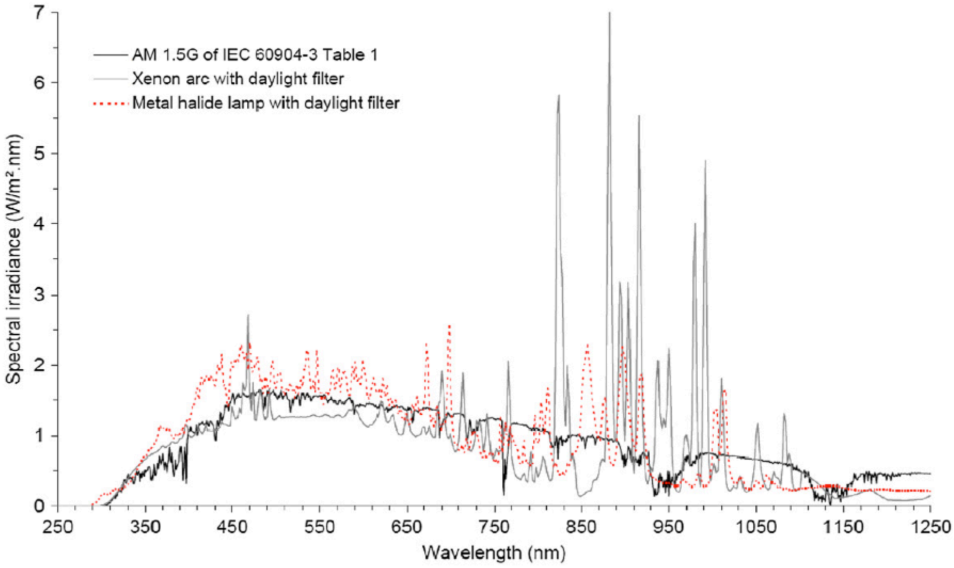

Figure 2.24: The spectral overlap of AM1.5G, xenon arc and metal halide lamps with daylight filters. Both lamp spectra show good overlap in the optical region of 400 – 800 nm, as well as the UV region below 400 nm [141].

2.7.3 Active layer degradation studies

Due to the various active layer compositions and methods of application, a number of analytical techniques have been applied to study OPV material degradation.

Neugebauer et al. [143] used Fourier transform infrared (FTIR) spectroscopy to investigate the degradation rates for films of MDMO-PPV·C_{60}. Films were illuminated for up to 8 hours in a pure oxygen environment. By observing the specific absorption bands at 1506 cm^{-1} for MDMO-PPV and 1182 cm^{-1} for C_{60}, the respective degradation rates could be determined. C_{60} degraded at a lower rate than MDMO-PPV. In another study, Paci et al. [144] examined changes in illuminated P3HT·$PC_{61}BM$ films with time. Bands at 1534 cm^{-1}, 1553 cm^{-1} and 1490 cm^{-1}, attributed to the aromatic C=C bonds in $PC_{61}BM$, shifted towards lower wavenumbers of 1525 cm^{-1} and 1456 cm^{-1}, suggesting PCBM clustering [144].

Hintz et al. [145] used UV-visible spectroscopy to map the degradation of P3HT films subjected to ozone or photo-oxidation conditions. UV-visible absorption decreased linearly with time under photo-oxidation but decreased exponentially with time under ozone conditions. Different rates of absorption reduction suggested that P3HT degraded via different mechanisms depending upon conditions. Degradation via ozone conditions indicated that P3HT exists with reduced conjugation in large numbers, due to the observation of absorption blue-shift. Another study of P3HT degradation by Manceau et al. [146] also observed a blue-shift in peak UV-visible absorption, along with the disappearance of spectral features, suggesting a change in interchain order.

Transient absorption spectrophotometry (TAS) is an extension of UV-visible spectrophotometry measuring a sample's photoconductivity. Reese et al. [147] used TAS to monitor films of P3HT and P3HT·$PC_{61}BM$, aged under inert and ambient environments. The films changed negligibly under inert condition over 1000 hours, whereas complete OPV cells showed a reduction of 60% in performance. It was concluded that under inert conditions, reduced OPV performance is solely caused by interface and electrode degradation. Ageing under ambient conditions showed a decrease in absorption, and photo-bleaching. Also, P3HT degraded quicker than a film of P3HT·$PC_{61}BM$, suggesting that $PC_{61}BM$ has a protective effect. In another study by Kumar et al. [148], P3HT films developed deep traps with photo-oxidation, leading to exciton quenching and charge recombination. Keivanidis et al. [149] determined that effective exciton dissociation and limited geminate recombination to be the dominant factors determining solar cell performance. The phase sizes of P3HT and $PC_{61}BM$ influenced exciton dissociation.

Wang et al. [150] used x-ray diffraction (XRD) to investigate changes in crystallinity for films of subphthalocyanine and C_{60} (SubPc·C_{60}) over time. Initial measurements showed no observable diffraction peak, indicating the material to be amorphous. With ageing under AM1.5G illumination, a diffraction peak developed, suggesting crystallisation over time.

Atomic force microscopy (AFM) with its ability to measure surface roughness with Ångström resolution has been used to monitor active layer profiles. AFM has assisted in providing information about active layer morphology, which is correlated to FF. AFM was used to image the contact surface, studying microscopic holes as a result of oxidation [151]. Griffini et al. [135] investigated the surface roughness of films based upon thieno[3, 4-c]pyrrole-4, 6-dione with bromine functionalised octyl side chains (TPD-Br16) and PCBM.

These films were stand-alone, and not part of complete OPV cells. Roughness values were compared for TPD-Br16 with $PC_{61}BM$ or $PC_{71}BM$. PCBM aggregates were observed, which were less pronounced for $PC_{71}BM$. It was suggested that the shape of the $PC_{71}BM$ molecule gave increased morphological stability. AFM studies have found that a film's surface becomes rougher with ageing and various stresses, through material aggregation [152–154].

2.7.4 XPS studies on polymer stability

X-ray photoelectron spectroscopy (XPS) is capable of quantitatively measuring the elemental composition and chemistry of materials. X-rays probe the surface of a material ejecting electrons towards an energy-dispersive detector. The energy required to eject the electrons gives an indication of the elements present and their environment, such as other bound atoms. XPS is ideal for studying degradation in OPV active layer materials, which a number of groups have already done.

Hintz et al. [145] used XPS to study P3HT exposed to oxygen under dark and illuminated conditions. The exposure of P3HT to the atmosphere under dark conditions resulted in no significant binding energy shifts for XPS spectra. Following illumination in the atmosphere, there were shifts for sulphur (S 2p), carbon (C 1s) and oxygen (O 1s) peaks, but these were reversible upon thermal annealing under vacuum. Reversible effects suggest that only minor chemical interactions are present, which leads to the p-doping of P3HT.

P3HT was also exposed to a high humidity atmosphere in both dark and illuminated conditions, and then thermally annealed under vacuum. P3HT under dark conditions showed a shift of C 1s and S 2p back to their initial positions, showing reversibility. Illuminated P3HT did not show the same recovery, indicating two oxygen species. A physisorbed oxygen forming a metastable charge-transfer complex, and oxygen contained in a photo-oxidised species.

Seo et al. [155] investigated P3HT films exposed to different levels of humidity. With increasing water content, the S 2p and C 1s peaks decreased in intensity. The O 1s peak increased, suggesting P3HT oxidation. Their literature review suggested the formation of sulphoxide (R-SO-R), from the sulphur atom of the thiophene ring (shown in Figure 2.25). No oxidised S 2p species as a result of P3HT ring opening were discerned from XPS spectra. Changes in oxidised C 1s were mostly attributed to C-OH (alpha-unsaturated alcohol) on the side chain, as shown in Figure 2.25.

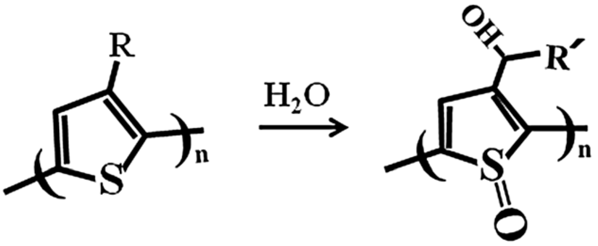

Figure 2.25: Following exposure to water, oxygen bonds to the sulphur atom, and to the aliphatic side chain. The ring structure is preserved [155].

Krebs et al. [156] were one of the few groups to study the long-term degradation of P3HT·PC$_{61}$BM and PEDOT·PSS samples using XPS; all kept illuminated at 100 mW.cm^{-2}. Data are shown in Figure 2.26. The peak broadening of S 2p was ascribed to chain scission between the thiophene units in the polymer backbone, or more likely the loss of side chains. At longer exposure times, the aromatic structure is more likely to break forming R-SOx. New C 1s peaks emerged due to oxygenated carbon species, particularly R-COOH.

Krebs et al. [156] also studied XPS spectra for inverted cells. OPV cells were exposed to vapours of $^{18}O_2 \cdot N_2$ and $H_2{}^{18}O \cdot N_2$ using the ^{18}O tracer. In contrast to other reports, XPS spectra showed no change between cells kept in a nitrogen glovebox under dark conditions and also illuminated in the presence of oxygen gas and moisture respectively. Oxygen contamination during fabrication was disregarded from the ^{18}O tracer, with data shown in Figure 2.27.

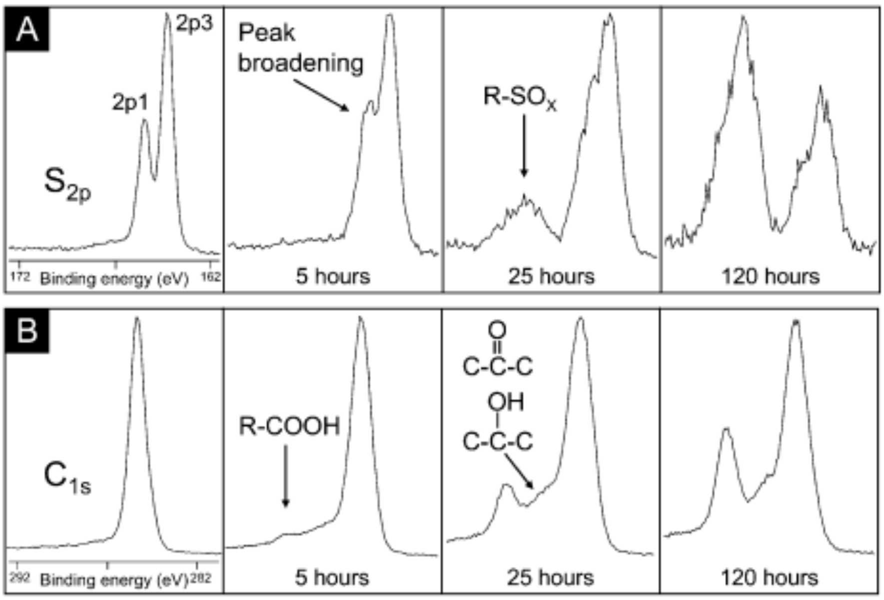

Figure 2.26: XPS spectra for P3HT, showing (A) S 2p peak and (B) C 1s peak as a function of time [156].

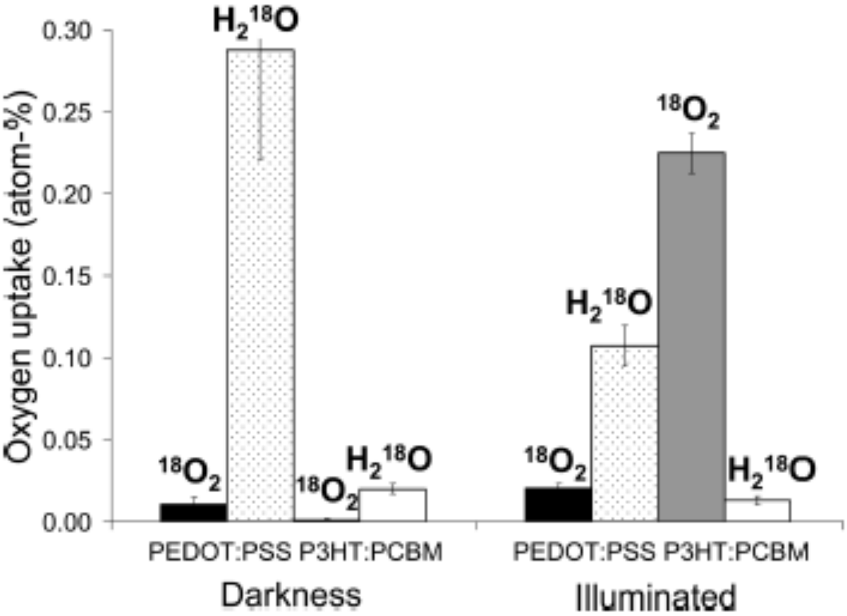

Figure 2.27: The uptake of isotopically labelled water and molecular oxygen for PEDOT·PSS and P3HT·PCBM films [156].

It was not known whether many mechanisms or a bottleneck was responsible for degradation. The low levels of water and oxygen uptake by P3HT·PCBM and PEDOT·PSS suggested that cell degradation was down to an interface phenomenon. If an interface phenomenon was the bottleneck, then the regular geometry of ITO/PEDO·PSS/P3HT·PCBM/Al would degrade rapidly in humid atmospheres. Water diffuses through the Al grains in the electrode, leading to aluminium hydroxide [$Al(OH)_3$] or aluminium oxide (Al_2O_3), which acts as an insulator. Molecular oxygen can also diffuse through pinholes in the Al, but this is a slower diffusion pathway than for water [157]. In an inverted cell, PEDOT·PSS acts as a protective layer against molecular oxygen and water penetration.

2.7.5 XPS studies on fullerene stability

Fullerene and fullerene derivatives are accepted to be stable at temperatures of up to 80°C in inert atmospheres [158]. However, upon exposure to oxygen, the fullerene electron mobility decreases by several orders of magnitude leading to reduced conductivity [159]. This problem is accentuated when exposed to UV radiation, typical of the AM1.5G spectrum, increasing oxygen atom diffusion into voids found in non-crystalline ordering. The formed oxygen-fullerene adducts take on an epoxide structure [160]. These oxygen atoms ultimately lead to fullerenes becoming electron charge quenchers. Also, the formation of $C_{60}O_2$ or $C_{60}O_4$ leads to an increased molecular size, resulting in active layer morphology changes. This has the effect of increasing phase segregation spacing [160]. Oxygen can also reduce the conductivity without chemically reacting with fullerene. Oxygen's presence leads to the formation of a charge-transfer state, decreasing the effective charge mobility and increasing recombination losses [161].

XPS has also been used to characterise fullerene derivative degradation. For example, to understand the effect of oxygen upon the fullerene derivative $PC_{61}BM$, Bao et al. [162] probed the material in its pristine state, and after exposure to molecular oxygen. XPS signals for C 1s and O 1s (see Figure 2.28) showed no new features, which would otherwise indicate new bonds are forming with the carbon and oxygen present within $PC_{61}BM$. However, oxygen content increased by approximately 8%. The ionisation potential was unchanged, suggesting that $PC_{61}BM$ had not undergone any chemical reaction with oxygen. All changes were reversible upon thermal annealing under vacuum.

$PC_{61}BM$ exposed to water vapour in a nitrogen atmosphere led to decreases in work function and ionisation potential, indicating a chemical reaction. XPS spectra also showed an oxygen uptake of 34% leading to new peaks (shown in Figure 2.28), including the broadening of C 1s due to C-O. In contrast to the results of oxygen exposure, these changes were not completely reversed by thermal annealing under vacuum [162].

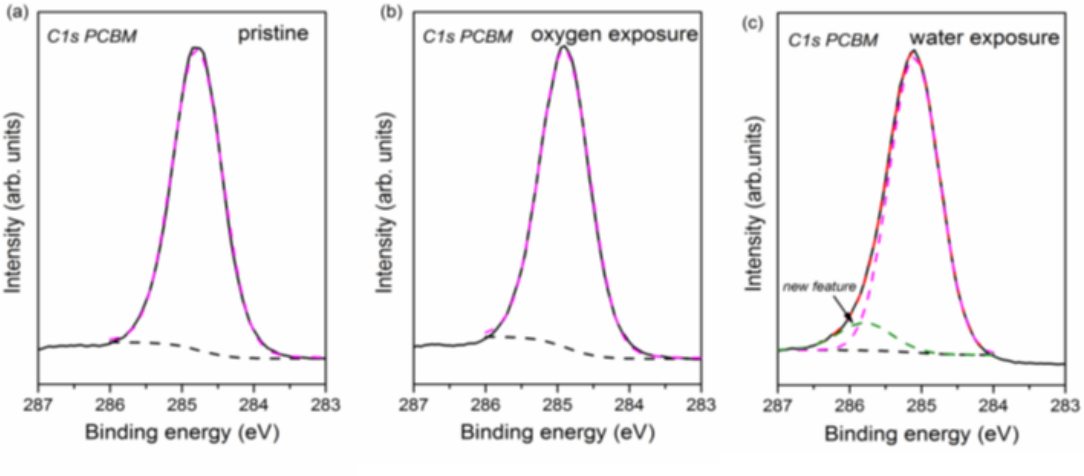

Figure 2.28: XPS spectra of C 1s signals for $PC_{61}BM$ in its pristine state and following exposure to molecular oxygen and water respectively. New features are present for $PC_{61}BM$ exposed to water (c), indicative of a chemical reaction [162].

Reports show that mixing a fullerene derivative with conjugated polymers leads to longer OPV cell lifetimes, as a result of increased stability. This behaviour has been explained by the fullerene derivative acting as a radical scavenger, and quenching the singlet state in P3HT [158]. This may be as a result of conjugated polymers being more susceptible to any oxygen present [163]. In terms of chemical changes, it is believed that only 1 to 10% of absorbed oxygen contributes to any chemical reaction, implying that the majority of performance loss is due to physical change [161].

2.7.6 Electrode degradation

Most laboratory OPV cells use a transparent conductive metal oxide (TCO) such as ITO, ZnO or NiO as an anode, and a conductive metal such as Al, Ag or Au as a cathode. [164].

There are two mechanisms when considering electrode degradation. The first leads to a decrease in the contact between the electrode and polymer active layer. Typical failure mechanisms include a reduced active electrode area, due to the formation of voids, or delamination. The other is chemical changes in the electrode, which includes the formation of electrically insulating regions within the electrode itself, impeding charge transfer [158]. A number of non-destructive techniques such as electroluminescence or thermography have studied both of these changes [165–167].

The most commonly used interfacial layer, which acts as a hole injector, is PEDOT·PSS. PEDOT·PSS is known to be acidic with an approximate pH of one [41]. When cast upon ITO, it can lead to etching, causing ions of indium and tin to become separated from the ITO layer, as reported by Sharma et al. [168, 169]. The migrated ions could result in degradation of the electrical performance by numerous mechanisms including the formation of electrical trap states in PEDOT·PSS or change of interface dipoles [168–170]. As well as contact improvement, interfacial layers can also reduce potential reactions between the TCO and active layer that may lead to a different mechanism of degradation.

2.7.7 Degradation prevention

Since OPV cells are likely to be deployed in outdoor environments under varying weather conditions, it is necessary that cells be suitably protected from environmental water and oxygen. Criteria often used for measuring barrier layer performance in devices such as OPV cells are oxygen transmission rates (OTR) and water vapour transmission rates (WVTR) [171].

The ingress of water through a barrier occurs at a faster rate than oxygen, making WVTR the reported figure of merit for barrier materials [172].

The most suitable environmental barrier is glass on glass. However, this is potentially costly and with limited flexibility. Low weight, although non-commercially available flexible glass has been announced by companies such as 3M [63]. If a glass layer is used as an encapsulant on top of an OPV cell, the likely source of ingress is at the edge seal. Glass on glass encapsulation demonstrates a WVTR of 10^{-6} $g.m^{-2}.day^{-1}$, which is the widely quoted requirement for OLED devices/OPV cells. This would lead to an operational lifetime in excess of 10000 hours in OLEDs [89].

The preferred barrier layers for OPV cells are typically made of plastic. Among these are polyethene terephthalate (PET) and polyethene naphthalate (PEN), which have WVTR of 0.2 $g.m^{-2}.day^{-1}$ and 10^{-3} $g.m^{-2}.day^{-1}$. PEN has the disadvantage of being more expensive than the more widely available PET material [173, 174].

A recent approach to providing an atmospheric barrier has been to use electron-beam deposition or ALD encapsulation of oxides on top of a layer such as PET or PEN. These oxides include silicon dioxide (SiO_2), titanium dioxide (TiO_2), Al_2O_3 and zirconium oxide (ZrO_2). Huang et al. [175] tested the ability of electron-beam deposited materials to isolate samples of calcium from atmospheric water and oxygen. Oxide layers from 10 nm to 50 nm were optimum, with Al_2O_3 and ZrO_2 being superior materials. Barrier layers in excess of 60 nm did not provide additional encapsulation as a result of crack formation, due to the significant residual stress of the oxide films.

In one example organosilicon and silicon oxide were alternately deposited onto PET [176]. A single deposition gave a WVTR of 0.22 $g.m^{-2}.day^{-1}$. An additional five depositions of organosilicon and silicon oxide gave a WVTR of less than 1 x 10^{-2} $g.m^{-2}.day^{-1}$, demonstrating suitable encapsulation for a flexible substrate.

Recent work by Sarkar et al. [177] deposited an 18 nm layer of Al_2O_3 around a completed OPV cell. This also had the effect of marginally increasing solar cell performance, since the encapsulation procedure acted as an annealing step. Al_2O_3 layers in excess of 10 nm have shown a WVTR of 5 x 10^{-5} g.m^{-2}.day^{-1} [178]. Figure 2.29 shows how Al_2O_3 was used to provide a barrier around an entire OPV cell.

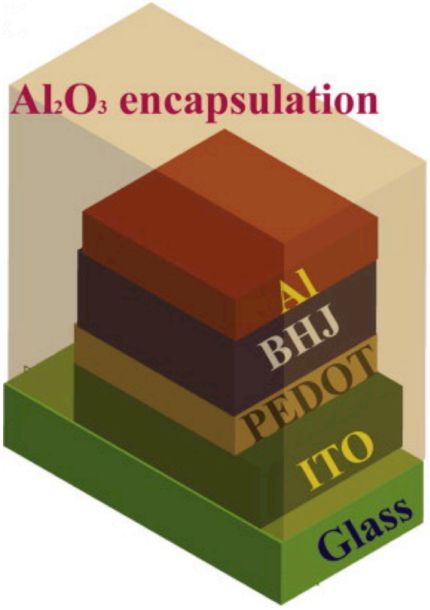

Figure 2.29: Al_2O_3 was deposited using ALD around a BHJ OPV cell, providing an environmental barrier. ALD also had the effect of increasing performance, as it introduces an annealing step [177].

2.8 Summary

This chapter briefly discussed the physics underpinning the operation of OPV cells, and how they may be characterised. Summarised were the different categories of materials used in OPV cells, including processing additives for active layer morphology control. Particular interest was paid to the material PCPDTBT, which has been predicted to give cells with a PCE as high as 7%.

Also reviewed were the testing procedures for characterising OPV cells, and data presentation. Finally, the degradation pathways of OPV cells were discussed, along with measures employed to remedy this problem. Interest in PCPDTBT led to particular attention being given to this material, with CPDT-BT based active layer materials being the focus of this thesis.

Little work exists on the long-term performances of OPV cells, with the prime focus being on that of initial PCE. No known reports on the lifetimes of PCPDTBT-based solar cells exist. Therefore it was decided to investigate this aspect of OPV properties.

Chapter 3 Experimental methods

3.1 Introduction

This chapter presents the experimental techniques used in this thesis. All cell fabrication and most characterisations were conducted at the School of Electronic Engineering, Bangor University. FTIR and UV-Vis spectroscopy, and WAXS (XRD) measurements were performed at the School of Chemistry, Bangor University. Dr U-Ser Jeng at the National Synchrotron Centre of Taiwan was responsible for GIWAXS/GISAXS measurements and curve fitting. Prof Graham Smith at the University of Chester was responsible for XPS measurements. For the latter experiments, the external collaborators handled operation, with data analysis and interpretation conducted by the author in collaboration.

3.2 Fabrication methods and materials

3.2.1 Laboratory environment

Materials and sample preparations were undertaken in a Class 1000 cleanroom. This included blend preparation, substrate cleaning, PEDOT·PSS deposition and ZnO sputtering. Cells were fabricated in a nitrogen-glovebox, which maintained oxygen and water concentrations as low as 0 parts per million (ppm) and removed solvent vapours.

3.3 Fabrication procedure

3.3.1 Active layer solution preparation

All active layers were deposited from solution unless otherwise stated. Donor polymer or oligomer and a fullerene were dissolved in anhydrous chlorobenzene with the desired blend ratio, to give a concentration of 30 mg.mL^{-1} (unless otherwise stated). The solutions were kept in sealed vials on a hot plate at 50°C in the glovebox, dissolving for at least 48 hours. Magnetic stirring was used to improve dissolution.

The SCLC and OFET devices used active layer solutions containing only the donor polymer (without a fullerene). The solutions used for SCLC and OFET devices were made to concentrations of 30 mg.mL^{-1} and 10 mg.mL^{-1}, to give active layer thicknesses of approximately 100 nm and 20 nm. All active layer donor polymers and oligomers were synthesised and supplied by Dr. Masaki Horie's group at Tsing Hua University in Taiwan, and are described in further detail in chapters 4, 5 and 6. Poly(3-hexylthiophene-2,5-diyl) [P3HT] (regioregular, M_n 54,000 – 75,000) with a purity of 99.995% was synthesised by Plextronics Inc. and supplied by Sigma-Aldrich. Nano-C Inc. supplied the fullerenes PC$_{61}$BM and PC$_{71}$BM, with purities of 99.99%.

3.3.2 Solution-processed OPV fabrication

Substrates of pre-patterned ITO electrodes on glass were jet washed with deionised (DI) water, propanone, and propan-2-ol, and dried using nitrogen gas. These substrates were UV/ozone treated for five minutes, removing any residual solvent and changing the surface energies.

Two device architectures were used in this thesis: inverted and non-inverted. Fabrication flowcharts for both non-inverted and inverted architectures are shown in Figure 3.1 (a) and (b), along with a schematic of the cell stacks (c) and (d).

Initially, non-inverted cell substrates were coated with PEDOT·PSS (Heraeus Clevios™ P VP AI 4083), and spin-cast at a speed of 5000 RPM for 30 seconds, giving an approximate layer thickness of 45 nm. PEDOT·PSS coated substrates were transferred to a nitrogen glovebox, and thermally annealed for 20 minutes at 120ºC, removing any residual water.

For inverted cell substrates, the substrates were cleaned in the same manner, but an initial layer of ZnO was sputtered to give a thickness of 20 nm. The substrates were removed from the sputter coater, transferred to a nitrogen glovebox, and annealed for 30 minutes at 200ºC removing any residual water.

On top of the PEDOT:PSS (non-inverted) or ZnO (inverted), an active layer blend was spin-cast for the required speed and time. The substrates were thermally annealed at the required temperature and duration and allowed to cool.

The substrates were transferred to a holder with suitable shadow masks and placed in a thermal evaporator located inside the glovebox. In turn, layers forming the cathode (non-inverted) or anode (inverted) were evaporated at a base pressure of approximately 10^{-6} mBar. The most commonly used combination for non-inverted cells was 8 nm of Ca followed by 80 nm of Al. Initial work in this thesis used 3 nm of LiF followed by 80 nm of Al. For inverted cells, 10 nm of MoO_3 was evaporated followed by 100 nm of Ag. These processes are outlined in Figure 3.1 for non-inverted (a) and inverted (b). Schematics of completed cells are also shown in Figure 3.1 for non-inverted (c) and inverted (d) cells.

SCLC devices were fabricated using the same procedure for non-inverted cells, with the cathode, in this case, consisting only of 80 nm of Au.

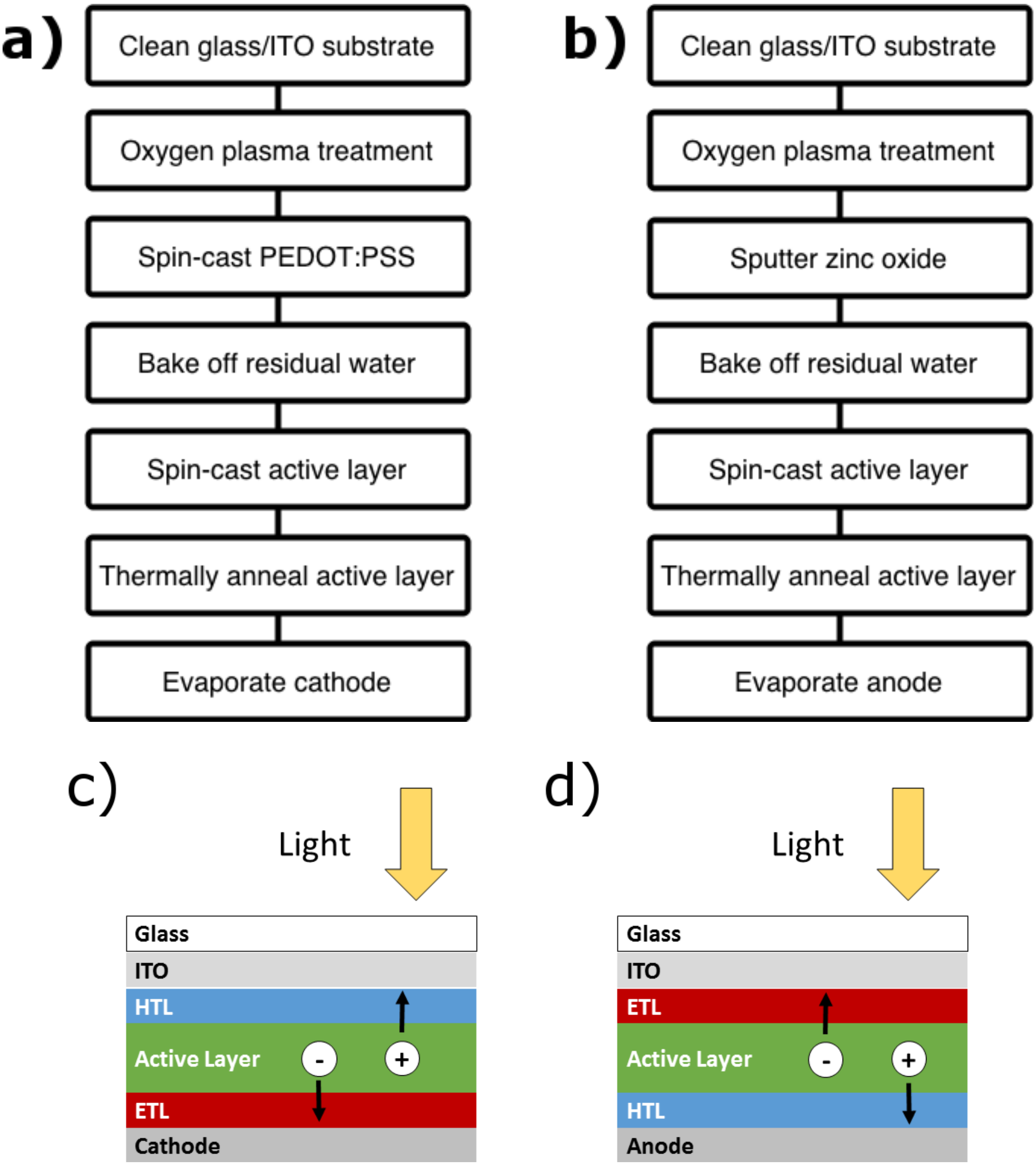

Figure 3.1: The sequence of steps used for the fabrication of OPV cells using non-inverted (a) and inverted (b) structures. The resulting structures of non-inverted (c) and inverted (d) cells. Light propagates through the glass, towards the active layer. Some light, which is not absorbed, is reflected from the back cathode/anode.

3.3.3 ITO patterning, shadow mask design and encapsulation

Two separate OPV configurations were used. The first configuration consisted of six pixels and used for most OPV cells in this thesis. Due to the difficulty of obtaining an effective barrier, a second design with only three pixels allowed the entire active layer to be encapsulated, limiting water and oxygen ingress. These designs are termed *six pixel* and *three pixel* cells from here onwards. The ITO layers were bought pre-patterned from Psiotec Ltd UK. The three pixel OPV cell design required photolithography to etch away ITO. Etching was done in pure hydrochloric acid (HCl), which took approximately five minutes followed by a rinse with DI water.

OPV cell active areas of 0.07 cm^2 for six pixel and 0.14 cm^2 for three pixel cells were defined by the overlap of the ITO and the top electrode. The top electrode was evaporated through a shadow mask. Figure 3.2 shows the patterned ITO and top electrode application for the six pixel design, with the top and bottom electrode overlap defining the active area.

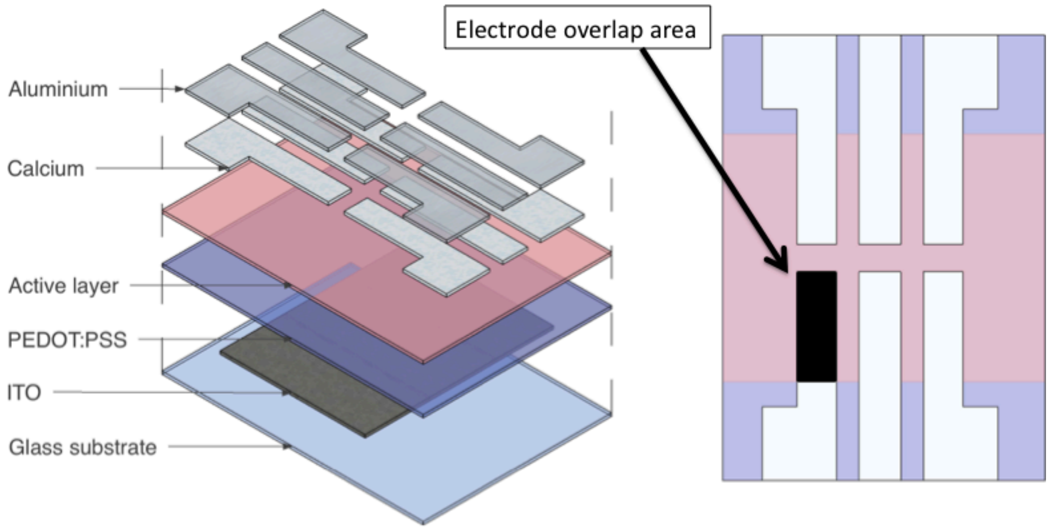

Figure 3.2: Overall cell design for six pixel OPV cells. The expanded structure (left) shows the shape of the ITO electrode, with the view from above (right) showing the overlap of the top electrode.

For certain experiments, OPV cells were encapsulated under inert conditions inside the nitrogen glovebox. Upon removal from the thermal evaporator, a small amount of UV-curable epoxy resin (supplied by Polymetronics Ltd. UK) was placed on the top surface of the OPV cell with a pipette. Tweezers were used to apply a cover slip gently on top of the epoxy resin, removing any air pockets. The OPV cell was then placed under a UV lamp (λ = 355 nm) for three to five minutes until the epoxy resin had set. UV light was deemed not to reach the photoactive region, due to the blocking effect of the top electrode and absorption by the epoxy.

3.3.4 Evaporated OPV cells

Substrates of ITO on glass were solvent cleaned, and ozone treated before being transferred to a thermal evaporator located in a nitrogen glovebox. Once a base pressure of 10^{-6} mBar had been achieved, 10 nm of MoO_3 was evaporated at 0.1 Å.s^{-1}, followed by the desired donor material and C_{60}. The cathode consisted of 8 nm of Ca followed by 80 nm of Al, both also evaporated.

3.3.5 OPV characterisation

OPV cell photoelectric characteristics were evaluated by conducting I-V sweeps, where a voltage was applied, and the resulting photocurrent measured. Data collected from I-V sweeps determined V_{OC}, J_{SC}, FF and PCE, as shown in Figure 2.4.

Cells were subjected to a voltage sweep from -0.5 V to 1 V, equivalent to approximately $-V_{OC}$ to $+2V_{OC}$. The sweep incremented in steps of 20 mV, with step interval and measurement for a duration of 100 ms each, accounting for bulk material relaxation times due to capacitive effects [141]. Initial cell characterisation used a Class AAA Newport xenon arc lamp, with a spectrum matching AM1.5G and 100 mW.cm^{-2}.

Following initial characterisation, cells to be lifetime tested were placed under a Class BAA halogen-bulb commercial light soaking system, supplied by GB-Sol Ltd. Taff's Well, Wales. I-V measurements swept using the previous range were conducted every 30 minutes for up to 1000 hours, with the cells disconnected between measurements. Outlined in

Table 3.1 are the illumination Class specifications, with pictures of the illumination sources shown in Figure 3.3. During testing, the temperature and humidity were measured but not controlled as 50 ± 5ºC and 40 ± 5%. These testing procedures conformed to the ISOS-L-2 standard [141], as outlined in Table 2.4.

Table 3.1: American Society for Testing and Materials (ASTM) class specifications for solar simulators. A solar simulator with AAA rating would have a spectral match, irradiance spatial non-uniformity and temporal instability of class A.

Classification	Spectral match	Irradiance spatial non-uniformity (%)	Temporal instability (%)
Class A	0.75 – 1.25	2	2
Class B	0.60 – 1.40	5	5
Class C	0.40 – 2.00	10	10

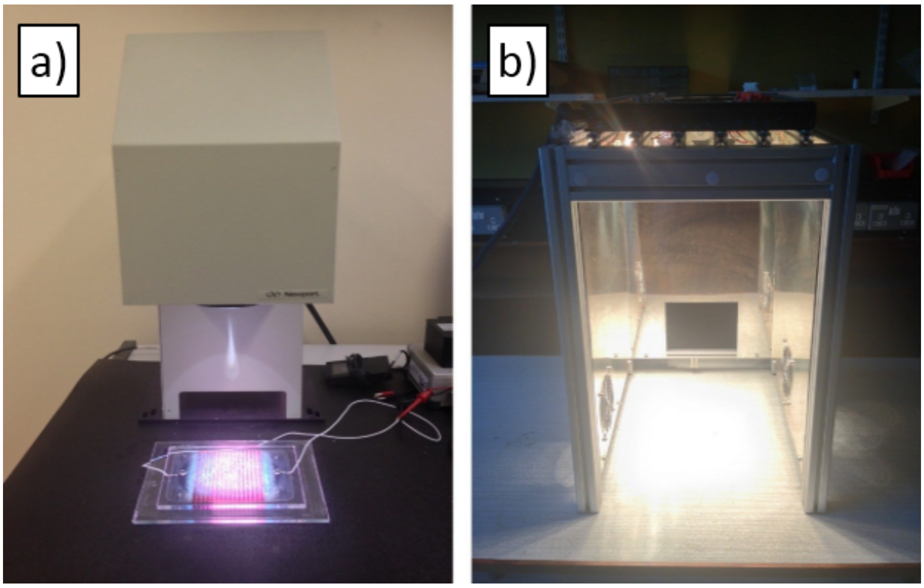

Figure 3.3: Class AAA AM1.5G illumination (a) gave focussed illumination with an intensity of 100mW/cm2. Class BAA tungsten halogen bulb light-soaker (b), was used for light soaking experiments.

3.3.6 OFET device fabrication

OFET devices have previously been used for the calculation of maximum hole mobilities for analogues of CPDT-BT based materials [80, 81, 112, 113, 118]. Therefore, OFET devices were fabricated to enable comparison of the mobility with previously published results. Bottom-gate top-contact OFET devices were fabricated, due to higher reported mobilities for this configuration [110].

Substrates of *n*++ doped silicon (Si) with a silicon dioxide (SiO_2) insulating layer were solvent cleaned with DI water, propanone, and propan-2-ol respectively and dried with nitrogen gas. The silicon substrates were ozone treated for five minutes, removing any residual surface contaminants.

Octadecyltrichlorosilane (OTS) was used to treat the surface of SiO_2, changing its wetting properties. The active layer blend was then spin cast at velocities ranging from 1000 to 3000 RPM for 60 seconds and thermally annealed at the desired temperature and duration. Cooled substrates were transferred to a substrate holder with the required shadow mask and placed in a thermal evaporator located inside the glovebox. A 100 nm Au electrode was evaporated through a shadow mask, giving channels of 60 µm length and 2000 µm width. Figure 3.4 shows a schematic of the OFET devices used in this thesis.

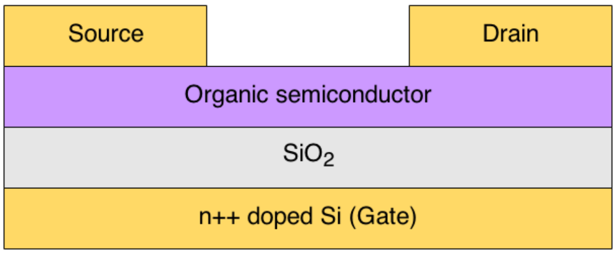

Figure 3.4: Bottom-gate top-contact FET structure, as used for hole mobility calculations.

3.3.7 Hole mobility calculations using OFET devices

OFET devices were electrically characterised to determine the hole mobility, when operated in the saturation regime. The transfer characteristics were measured by applying a constant source-drain voltage (V_{DS}), and varying the gate voltage (V_G) from +40 to -80 V. The output characteristics were measured by using a V_G of +20 to -100 V, in 20 V intervals, and varying the V_{DS} from +20 to -80 V. Both sets of measurements were conducted under dark conditions.

An OFET's saturation (active) region is reached when $V_{DS} > (V_G - V_T)$, where V_T is the threshold voltage [179]. In this region of operation, the drain-source current, I_{DS}, is defined by the equation

$$I_{SD} = \left(\frac{W}{2L}\right)\mu_{SAT}C_i(V_G - V_{TH})^2 \tag{3.1}$$

where W is the channel width, L is the channel length, μ_{SAT} is the saturation hole mobility, C_i is the capacitance per unit area of the silicon dioxide dielectric, V_G is the gate voltage, and V_T is the threshold voltage. Equation (3.1) is derived from the gradual channel approximation [180]. The gradual channel approximation assumes that the field-effect mobility is independent of the gate voltage, the source-drain contacts are Ohmic, more charge traps are filled, and that current flow is uniform. The value of C_i was determined from other reports (using C-V measurements) as 10.8 nF.cm^{-2} [181]. Hole mobility was directly extracted from the slope of linearly fitting the square root of I_{DS} versus V_G.

3.3.8 Hole mobility calculations using SCLC devices

During this project, OFET performances were initially used to measure hole mobility. However, after 12 months it was decided that SCLC (hole only) devices would be used for mobility measurements. Therefore, from section 4.5.3 onwards, SCLC devices were used.

SCLC devices were fabricated using the same procedure for non-inverted cells in section 3.3.2, To summarise; an ITO substrate was coated with PEDOT:PSS. The polymer was then deposited on top, followed by the electrode deposition (80 nm of Au). SCLC devices were biased from -2 to +10 V, incrementing at 25 mV, under dark conditions. The resulting space-charge limited current was measured [182]. Shown in Figure 3.5 is the relationship between the logarithm of measured current versus the logarithm of applied voltage for an organic semiconductor, sandwiched between two high work function electrodes. At low voltages, charge carriers are thermally generated demonstrating Ohmic behaviour. As more holes are injected into the organic material, the injected current dominates, with the current now space-charge limited. With increasing hole injection, charge traps are slowly filled until they become saturated, which occurs at the trap-filled limit, shown as V_{TFL}. Beyond the V_{TFL}, trap-free space-charge limited current behaviour is observed [183]. For all conditions, diffusion current is neglected.

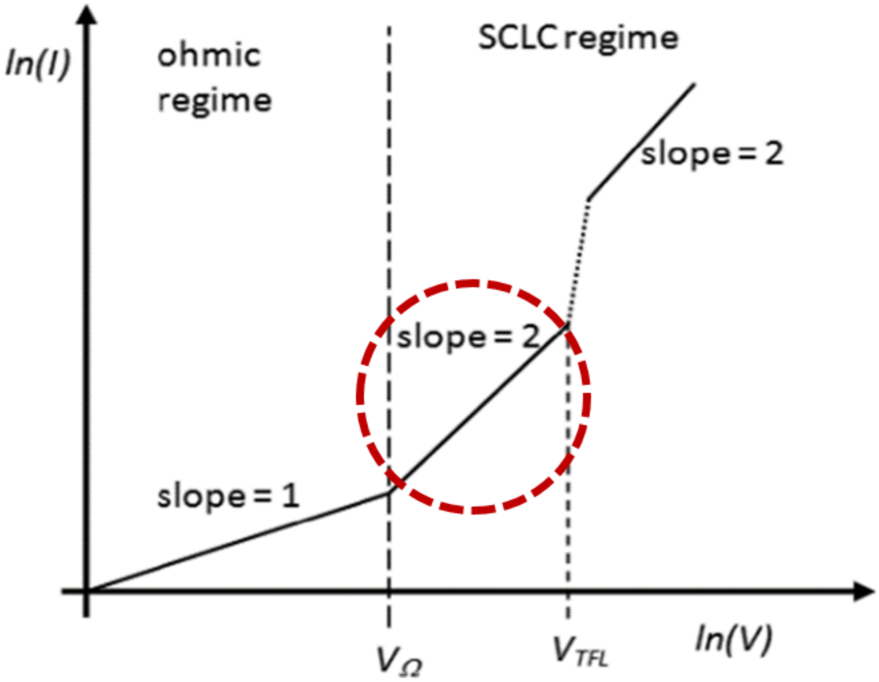

Figure 3.5: Shown is an exemplary plot of logarithm(current) versus logarithm(voltage). With increasing voltage, a SCLC device in the Ohmic region exhibits a linear increase in current. Secondly shallow trap states are slowly filled up, with the device current proportional to V^2. The gradient is twice that of the Ohmic region. [184]

Hole mobility was calculated from space-charge limited currents using the Mott-Gurney law, which is defined by the equation

$$J(V) = \frac{9}{8}\varepsilon_0\varepsilon_r\mu\frac{V_{EFF}^2}{L^3} \tag{3.2}$$

where J(V) is the current density, ε_0 is the permittivity of free space, ε_r is the relative permittivity of the organic material, μ is the hole mobility, V_{EFF} is the effective voltage, and L is the layer thickness. V_{EFF} is given by deducting the built-in potential, as a result of work function mismatch, from the applied bias.

A proportion of the injected holes are likely lost to charge-traps, therefore μ in Equation (3.2) represents the effective mobility, where the actual mobility is higher.

Although not representative of the absolute value, it does give an indication of relative mobility.

The effective voltage was calculated by deducting the built-in potential, given by the work function difference, from the applied bias. Work function values of 4.8 eV [185] and 5.3 eV [186] for ITO and Au were used, giving a built-in potential of 0.5 V. The data range used for mobility calculations were from the region circled in Figure 3.5, demonstrating I proportional to V^2 behaviour. Previously reported PCPDTBT ε_r of 3.4 and ε_0 of 8.85 x 10^{-12} F.m^{-1} were used [187, 188]. Based upon AFM thickness measurements, a value of 100 nm was used for L.

3.3.9 External Quantum Efficiency (EQE) Measurements

EQE measurements were conducted using the apparatus setup shown in Figure 3.6. A tungsten halogen light source was coupled to a monochromator. Light from the source was directed towards a servo-controlled diffraction grating, enabling selection of a particular wavelength. Light output from the monochromator then passed through an optical chopper, before being focused onto the sample, where the photocurrent was measured. The optical chopper was synchronised with a lock-in amplifier to improve the signal-to-noise ratio of the measured photocurrent.

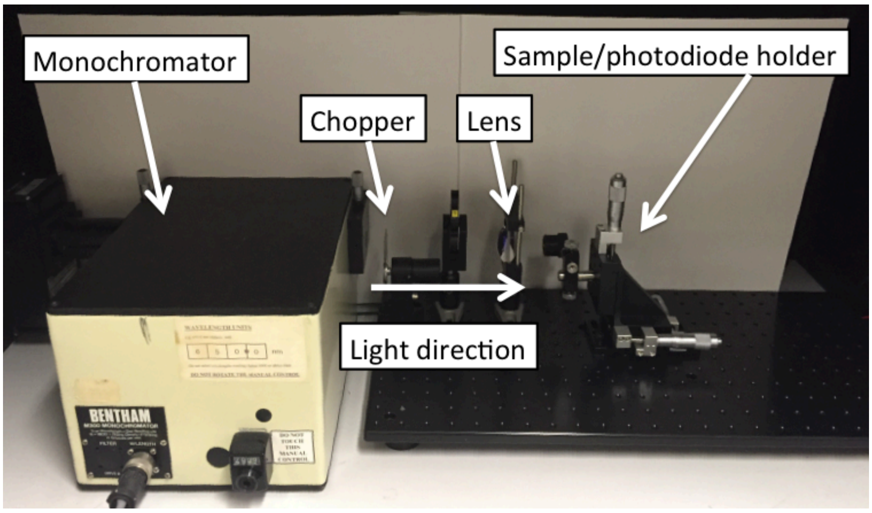

Figure 3.6: The apparatus and setup used for EQE measurements. A computer controlled the diffraction grating on the monochromator, incrementing the light wavelength, and subsequently measuring photocurrent either at a calibrated diode reference or for an OPV cell. Monochromatic light wavelengths incremented in 1 nm steps from 375 to 900 nm.

Initially, a photodiode with calibrated responsivity was mounted in place of the sample, measuring input power as a function of wavelength. The photodiode was replaced with an OPV cell, and the resulting photocurrent measured and used to calculate the EQE. EQE(λ) is defined by the equation

$$EQE(\lambda) = \frac{I_{SC}(\lambda)}{P_{IN}} \times \frac{hc}{e\lambda} \tag{3.3}$$

where $I_{SC}(\lambda)$ is the measured photocurrent, P_{IN} is the power of incident light calibrated from the photodiode, h is Plank's constant, c is the speed of electromagnetic radiation, e is the electronic charge, and λ is the wavelength of the incident light.

3.4 Material characterization

3.4.1 UV-Visible Spectrophotometry

UV-visible (UV-vis) spectroscopy was used for characterising the absorption of radiation as a function of wavelength for OPV active layers. The system used was an Ocean Optics UV-Vis (350 to 1100 nm) Spectrophotometer 4800, mounted beneath a Class AAA Newport xenon arc lamp (AM1.5G spectrum, 100 mW.cm^{-2}). A measurement of a glass or quartz substrate and the light source were collectively used to define a background absorption spectrum. A material's absorption spectrum was calculated by the difference between background and sample spectra.

3.4.2 Infrared Spectroscopy

Infrared (IR) spectroscopy was used to probe for particular chemical bonds within polymers, using a Varian 610-IR FTIR microscope. Glass substrates are highly absorbent in the IR region. Therefore, polymer films were cast upon potassium bromide (KBr) substrates, purchased from Fisher Scientific UK.

3.4.3 Atomic Force Microscopy

Atomic force microscopy (AFM) was conducted using a Digital Instruments Nanoman V, operated in the tapping mode. The tapping mode offers high lateral resolution with reduced forces, preventing damage to soft surfaces during imaging. AFM was primarily used to image the morphology of active layer thin films. An average of three scans were used to calculate the arithmetic mean (R_A) and quadratic mean (R_Q) surface roughness. AFM was also occasionally used to measure film thickness, by imaging the step across a slice in the layer.

3.4.4 X-Ray Diffraction

X-rays and resulting diffraction patterns were used to study active layer crystallography. Since atomic spacing is of order 10 x 10^{-10} m, crystals or molecules can act as a three-dimensional diffraction grating for x-rays. X-ray waves leave the source in phase but can be detected out of phase due to different path lengths. Variations in path lengths are a result of the difference in distance from the x-ray source to the scattering source, and from the scattering source to the detector. Bragg's Law for first-order diffraction patterns is defined as

$$\lambda = 2d \sin\theta \tag{3.4}$$

where λ is the x-ray wavelength, d is the atomic spacing, and θ is the angle of both incident and reflected x-rays (see Figure 3.7).

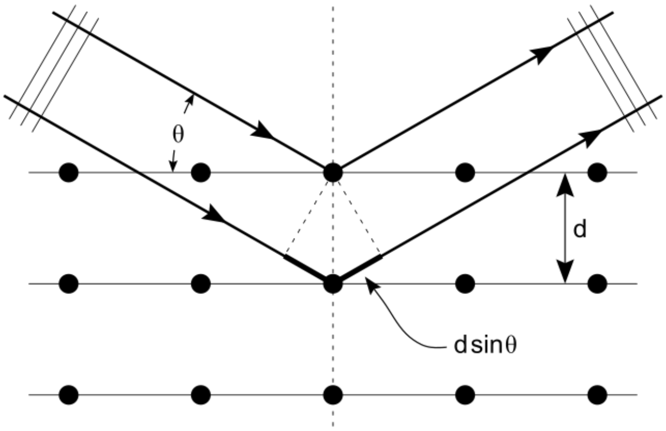

Figure 3.7: A representation of how the angle of reflected X-rays is governed by the atomic spacing of the sample.

X-ray diffraction can probe an organic film in two ways. A scattering vector is normal to the plane (q_z), with the observed intensity describing the periodicity out of the substrate plane [Figure 3.8 (a)]. A scattering vector points along the sample plane (q_{xy}) and the diffracting lattice planes are perpendicular to the sample, where an x-ray beam is grazed above the surface – grazing incidence X-ray scattering (GIXS) [Figure 3.8 (b)].

Using the first set-up, wide-angle x-ray scattering (WAXS) was used for studying the crystallography. It was primarily used to give an indication of the relative order, and determine the lattice spacing of observable peaks in polymer layers.

An evolution of GIXS is grazing incidence small angle x-ray scattering (GISAXS), which is used for probing the morphology of donor-acceptor blends.

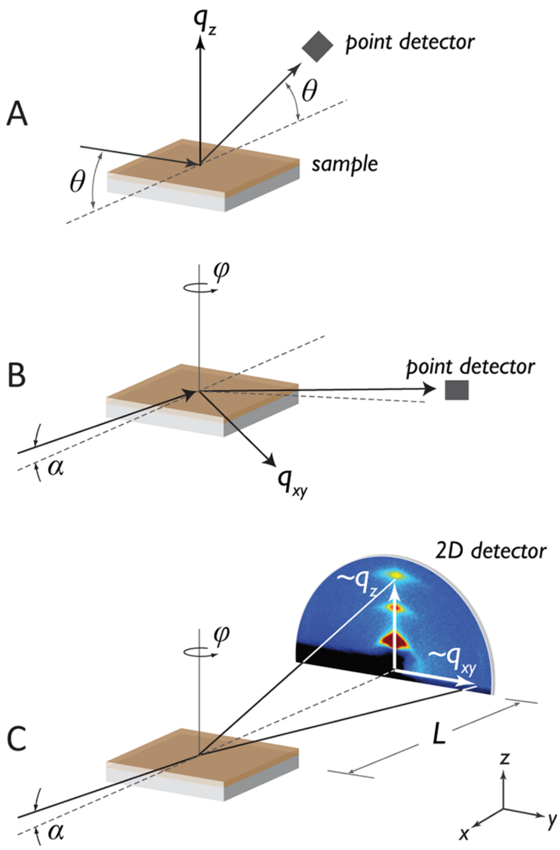

Figure 3.8: A) shows WAXS where an x-ray source and point detector are varied by the same angle. Constructive interference peaks are mapped to the angle. B) shows GIXSAXS where x-rays are grazed across the surface. C) shows grazing x-rays with a 2D detector that facilitates time-resolved measurements [189].

GIXSAXS combined with a 2D detector [Figure 3.8 (c)] was used to study structural changes in polymers with time. OPV bulk heterojunctions are made up of segregated phases of either differing polymers or polymers and fullerene. Within these polymer or fullerene-rich phases are smaller crystallites of highly ordered material. It is possible to use GISAXS to compare the order of crystallites and their scattering behaviour, and see if PCBM in the active layer is aggregating or changing in morphology.

3.5 Summary

This chapter outlined the procedures used for fabricating non-inverted and inverted OPV cells. Also discussed were the steps necessary for OPV cell encapsulation. The methods for characterising electrical, optical, and chemical and physical behaviours were also discussed and how they were used for obtaining results in this thesis.

Chapter 4 CPDT-BT based oligomers and polymers

In this chapter, two new materials based upon CPDT and BT monomers were characterised and used to fabricate OPV cells. Initial work focussed on the D-A-D oligomer of this material. Both evaporated bilayer and solution-processed BHJ structures were studied, and their performances compared. The second material studied was a D-A polymer synthesised via direct arylation. While the performance of this material has been previously reported, the novelty of the work was that the polymer was synthesised using a newer, easier, approach (conducted by Prof Masaki Horie). To the author's knowledge, this is the first time a functioning device (OFET, OLED or OPV cell) has been reported using a material obtained with this synthetic route.

4.1 Introduction to CPDT-BT-CPDT (C2B1) testing

OPV cells are classified as either polymer or oligomer (small molecule) cells, depending on the number of repeating units in the donor material utilised in the active layer. Conjugated polymers are typically processed from a solution into a BHJ for OPV cells, whereas oligomers can be processed from solution or by vacuum deposition [190–194]. Up until three to four years ago, solution processable oligomers were considered to give poor active layer [195]. This was due to molecular nucleation giving non-uniform films.

4.2 Synthesis of C2B1

The C2B1 oligomer was initially synthesised by a Pd catalysed Suzuki coupling reaction of equimolar mono-brominated diethyl cyclopentadithiophene and diboronic acid pinacol ester benzothiadiazole, as shown in Figure 4.1. C2B1 was isolated by column chromatography and recrystallisation, giving a product yield of 60%. Ethyl groups were used as side chains, facilitating solution processing.

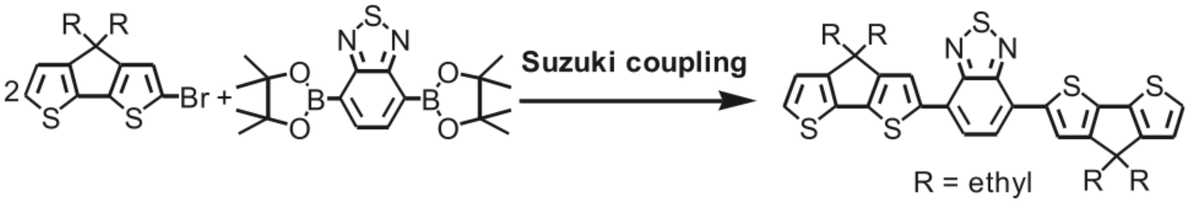

Figure 4.1: Shown is a Suzuki coupled reaction of mono-brominated diethyl cyclopentadithiophene and diboronic acid pinacol ester benzothiadiazole, giving a C2B1 yield of 60%.

C2B1 was examined using CV measurements by Masaki Horie, before being sent to Bangor University. The electrochemical HOMO and LUMO for the compound were estimated to be -5.2 and -3.0 eV. These levels are ideal for fabricating OPV cells in combination with PCBM, affording 4.5% on Scharber's diagram for OPV PCE prediction [17].

4.3 Charge mobility characterisation

The OFET performance of C2B1 was investigated using bottom-gate top-contact devices, on octadecyltrichlorosilane (OTS)-treated SiO_2/p++Si substrates. These devices were used to examine the hole mobility in the material. Two processing techniques of the active layer were applied: evaporation under vacuum, and solution processing through spin coating. The results of OFET characterisation using these two techniques are discussed below.

4.3.1 Evaporated OFET devices

C2B1 was thermally evaporated at 1.0 $Å.s^{-1}$, giving a final thickness of 15 nm, with the results summarised in Table 4.1. The hole mobility was extracted from OFET transfer characteristics when operated in the saturation regime, as shown in Figure 4.2 (left). The best performing devices gave a maximum hole mobility of 3.2×10^{-4} $cm^2.V^{-1}.s^{-1}$. This mobility is approximately two orders of magnitude lower than for the corresponding solution processed polymer, which has been reported as 3.7 x 10^{-2} $cm^2.V^{-1}.s^{-1}$. [118].

Table 4.1: The OFET characteristics of C2B1 on OTS-SiO_2/Si substrates. [a] saturated hole mobility, [b] threshold voltage, [c] hysteresis voltage, [d] on/off current ratio

Process conditions	μ_h [cm^2 V^{-1} s^{-1}]^a	V_T[V]^b	V_h[V]^c	$I_{ON/OFF}{}^d$
Solution (Room temperature annealing)	1.1 x10^{-3}	-8.40	-	3 x10^5
Solution (100°C annealing)	5.0x10^{-3}	-9.43	10.45	8.5x10^5
Thermal evaporation (with annealing)	3.2x10^{-4}	-4.07	16.10	2.4x10^5

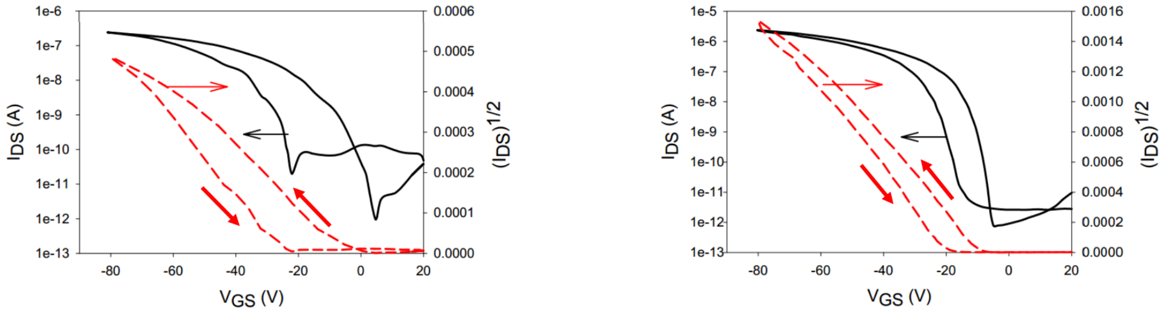

Figure 4.2: The OFET transfer characteristics of C2B1 (15 nm), evaporated at 1 Å.s^{-1} onto OTS-treated SiO2/*p*++ Si substrates (left). OFET transfer characteristics of C2B1 (20 nm), fabricated from 1% weight chlorobenzene solution on OTS-treated SiO_2/*p*++Si substrates (right).

4.3.2 Solution processed OFET devices

Due to the low performance of the evaporated C2B1, OFET performances were also tested for solution processed C2B1. C2B1 was dissolved at a concentration of 10 mg.mL^{-1} in anhydrous chlorobenzene and was spin-cast to form a ~20 nm film. The maximum hole mobility measured for C2B1 was 5 x 10^{-3} $cm^2.V^{-1}.s^{-1}$, which was achieved after annealing the film at 100°C inside a nitrogen glovebox (the results are summarised in Table 4.1). The hole mobility in the oligomer processed from solution is therefore 16 times higher than when processed using evaporative methods, but still 7.5 times lower than the polymer equivalent. This agrees with other reports on the difficulties in using oligothiophenes for high performing devices. The limited mobility of C2B1 is possibly due to unfavourable π-stacking. After annealing, the hole mobility increases by a factor of 1.5. This effect is contrary to the results published by other groups, who showed that annealing CPDT-BT based materials to lead to a decrease in performance. The increase in hole mobility is not significant and could be attributed to the removal of residual solvent in the film. While it has been reported that very little change in crystalline structure is observed in CPDT-BT based polymers [134, 196], the small enhancement in mobility might suggest increased molecular order, improving charge transport [197].

Solution processing C2B1 leads to improved OFET performance, and can be explained by a number of reasons. Firstly, the transfer characteristics of thermally evaporated C2B1 are noisier than for spin-cast C2B1. Such patterns are usually indicative of poor connections at the source, drain or gate, though could also be attributed to poor shielding during measurements. The testing of all devices was, therefore, conducted in a shielded environment to eliminate this problem, but this did not resolve the issue. Secondly, the stability of C2B1 for thermal evaporation at high temperatures is unclear, and the author did not possess equipment to study chemical changes or degradation that might occur during vacuum sublimation.

C2B1 also shows hysteresis on the backwards sweep of the transfer characteristics [198], indicated by the hysteresis voltage arising from threshold voltage shift due to bias stress. An increased hysteresis voltage for evaporated OFET devices may be attributed to the disorder of C2B1, which also affects charge transport. One of the greatest factors in determining charge-transport effects with oligomer sublimation is the molecular configuration during growth. The interface between evaporative nucleation sites had been shown to act as charge traps, effectively hindering charge-transport [199]. It is highly probable that the C2B1 deposited using evaporative methods possesses a less optimum morphology.

4.4 OPV cell characterisation

4.4.1 Optical absorption measurements

UV–visible absorption spectra for C2B1 dissolved in common solvents were measured and are shown in Figure 4.3. These solutions showed solvatochromism; pink in non-polar solvents such as hexane and purple in polar solvents such as chloroform. The solution peak absorption position (λ_{max}) shifted to longer wavelengths with increasing solvent polarity. The hexane solution of C2B1 showed λ_{max} at 555 nm that shifted to a longer wavelength of λ_{max} = 564 nm in chloroform solution. Solvatochromism behaviour has been reported for D-A polymers, where intramolecular charge-transfer between donor and acceptor groups is greater. This stronger structure is in a more excited state when in polar solvents than in non-polar solvents, leading to a longer wavelength shift of λ_{max} [200–204]. The peak absorption observed in thin films shifts to a slightly longer wavelength of λ_{max} = 566 nm compared to that in the solutions. Based upon the absorption spectra data in Figure 4.3, the optical energy gap ($E_{G\ OPTICAL}$) of C2B1 films was estimated to be 1.8 eV from the onset of the absorption. This energy gap is slightly higher than the polymer equivalent of 1.46 eV [81], which is to be expected as oligomers have shorter conjugation lengths.

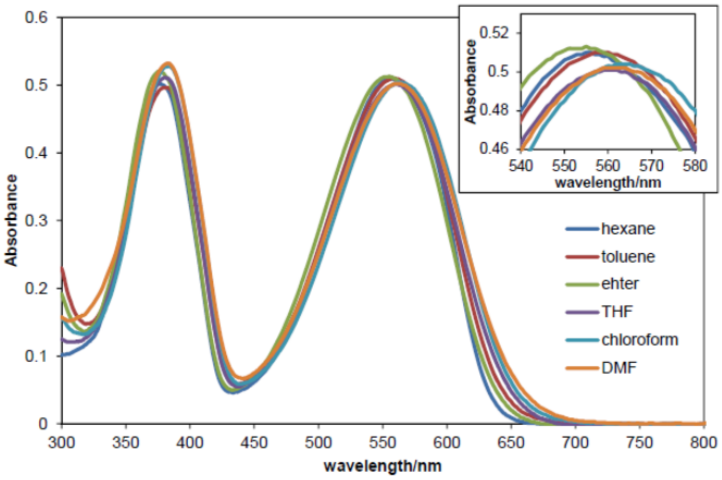

Figure 4.3: UV–visible absorption spectra of C2B1 in hexane and toluene, ether, THF, chloroform and DMF solutions. Inset is a close-up of the absorption peaks about 550 nm.

4.4.2 Evaporated OPV cells

As the absorption spectra indicated that C2B1 was a promising material, six pixel OPV cells were initially fabricated by evaporating C2B1 followed by the acceptor material, C_{60}. As the optimum thicknesses of the C2B1 and C_{60} layers were unknown, a range was evaporated onto glass substrates with ITO and PEDOT·PSS anodes. C2B1 thicknesses of 5 nm, 15 nm and 50 nm and C_{60} thicknesses of 5 and 15 nm were used. These were chosen as 5 and 15 nm are at the upper and lower values for reported exciton diffusion path lengths. A thickness of 50 nm was used to maximise absorption. The cathode electrodes consisted of 3 nm of LiF followed by 80 nm of Al, defining active areas of 0.07 cm^2.

The best performing I-V curve (under AM1.5G illumination) of evaporated C2B1 and C_{60} is shown in Figure 4.4. Data for all experiments are summarised in Table 4.2. The best performing cells were given by 50 nm of C2B1 and 15 nm of C_{60}, where a maximum PCE of 0.02% was measured.

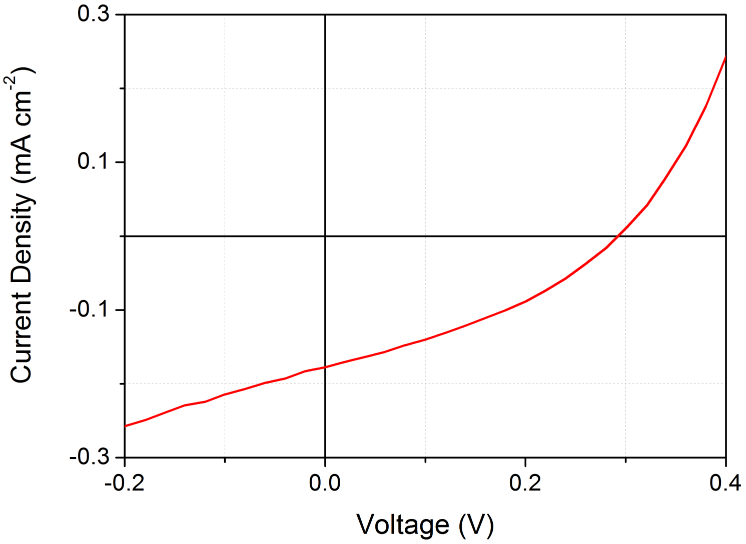

Figure 4.4: I-V characteristics of the best-performing cell, fabricated by thermal evaporation of C2B1 (50 nm) and C_{60} (15 nm).

Table 4.2: OPV results for thermally evaporated C2B1 followed by C_{60}. The best performing cells were given by evaporating 50 nm of C2B1 followed by 15 nm of C_{60}, giving a maximum PCE of 0.02%. All cells were characterised under AM1.5G illumination (100mW.cm^{-2}). Note: FF values could not be calculated for all cells.

Layer thickness (nm) (C2B1, C_{60})	**V_{OC} (V)**	**J_{SC} (mA.cm^{-2})**	**FF (%)**	**PCE (%)**
5, 5	1.05×10^{-3}	-3.68×10^{-4}	-	5.54×10^{-6}
5, 15	8.98×10^{-4}	-3.61×10^{-3}	-	4.63×10^{-5}
15, 5	2.29×10^{-4}	-2.4×10^{-4}	-	8.01×10^{-7}
15, 15	0.58	-2.34×10^{-5}	-	3.08×10^{-4}
50, 5	0.12	-4.05×10^{-3}	28.88	2.00×10^{-3}
50, 15	0.30	-1.244×10^{-2}	33.79	1.8×10^{-2}

All cells gave poor performance, with only two showing photovoltaic behaviour. It can be seen from Table 4.2 that the thicker the C2B1 layer, the better the solar cell performance. Photons leading to exciton generation are mostly absorbed in the C2B1 layer, as C_{60} has reduced absorption. A trade-off between thickness and performance is often seen in evaporated OPV cells. If the donor layer is too thin, the performance is limited by reduced absorption, whereas if the donor layer is too thick (i.e. greater than the exciton diffusion length), the performance is limited by exciton recombination, as the holes and electrons recombine before reaching the electrodes. Based upon the data in Table 4.2, it is likely that the peak performance has not been reached. A thicker C2B1 layer could yield further improvements in PCE. It is worth noting that limited quantities of C2B1 were available for fabricating and testing OPV cells. Thickness calculations were made from scratching the layer and measuring the step height using an AFM. It is therefore possible that some level of uncertainty is present in the thickness calculation. Exciton diffusion path lengths are approximately 1 to 20 nm in organic materials, meaning that C2B1 and C_{60} layers should not be greater than 20 nm in thickness respectively [130]. It would, therefore, be expected that OPV cells with C2B1 and C_{60} layers thinner than 20 nm to have increased PCE. C2B1 and C_{60} thicknesses of 50 nm and 15 nm respectively gave the best performance, through increased J_{SC} as a result of increased photon absorption. This could also be as a result of the non-optimised parameters used for C2B1, giving a different actual thickness.

As with the OFET devices fabricated in section 4.3, there is a need for greater fabrication process optimisation. Planar bilayer OPV cells are limited by their single donor-acceptor interface. It is, therefore, natural to progress to introducing further donor-acceptor interfaces and exercise control over the morphology of the active layer. The available facilities could only evaporate either C2B1 or C_{60} at any given time, preventing the co-evaporation needed to form bulk heterojunctions via evaporative methods.

4.4.3 Solution processed OPV cells

Due to the poor performance of evaporated active layers, six pixel C2B1 OPV cells were fabricated by solution processing on glass substrates with an ITO and PEDOT·PSS anode. Active layers of C2B1 with either $PC_{61}BM$ or $PC_{71}BM$ were spin-cast from chlorobenzene solutions to form BHJs; the fullerene content was varied. The cathode electrodes consisted of

3 nm of LiF followed by 80 nm of Al. OPV cell fabrication parameters were optimised by varying the blend concentration, film thickness and annealing conditions. Once again, annealing CPDT-BT-based films at slightly elevated temperatures did not lead to a decrease in performance, however an optimum was observed.

4.4.3.1 Effect of blend concentration

To optimise the blend concentration, the mass fraction (*w*/*w*) ratio of donor to acceptor was varied between 33% and 86% PCBM weight content. This range was chosen for two reasons; firstly the optimum for polymeric C2B1 OPV cells has previously been reported in this range, and secondly the charge-carrier mobilities when compared to PCPDTBT-based OFET devices vary only slightly. It was, therefore, possible to optimise OPV performance knowing that the bipolar charge transport properties remain relatively constant [118].

The results of this study are shown in Figure 4.5, Table 4.3 and Table 4.4. For C2B1·$PC_{61}BM$, no cells were fabricated with 86% fullerene content, as limited quantities of the oligomer were available for this work.

Under AM1.5G illumination (100 mW.cm^{-2}), a J_{SC} of up to -6.03 mA.cm^{-2} and -6.05 mA.cm^{-2} was achieved for cells of C2B1 with $PC_{61}BM$ or $PC_{71}BM$ respectively. The V_{OC} varied significantly for all measurements (0.65 V to 0.86 V), with optimal performance reached using a 1:3 blend of C2B1·$PC_{71}BM$. For C2B1·$PC_{61}BM$, the V_{OC} is higher than the electrode work function difference (~0.4 eV). V_{OC} is therefore determined by the effective energy gap between C2B1 and $PC_{61}BM$, inferring a better Ohmic contact with the electrodes [21]. The low J_{SC} from all cells suggest that although excitons are generated, they're not dissociated into free charge carriers, possibly due to limited donor-acceptor interfaces. This also applied to C2B1·$PC_{71}BM$. These losses are also demonstrated by the relatively low FF for all devices.

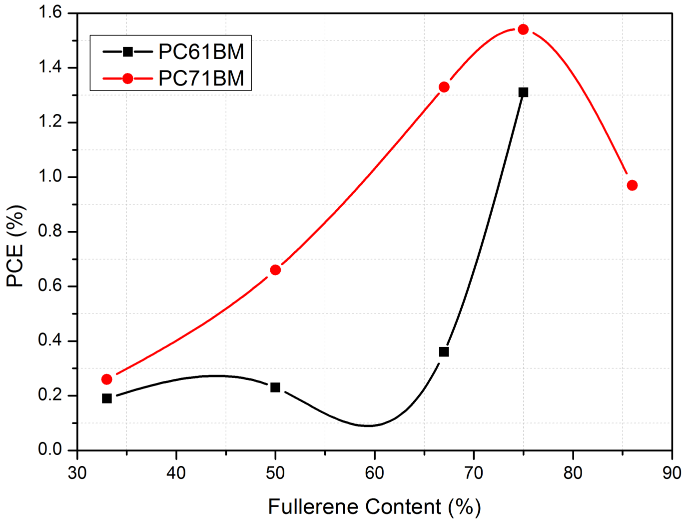

Figure 4.5: The variation in PCE as a function of fullerene content for $PC_{61}BM$ and $PC_{71}BM$. PCE peaks at a fullerene content of 75%.

Table 4.3: A summary of results for C2B1·$PC_{61}BM$ based OPV cells, under AM1.5G illumination (100 mW.cm^{-2}). The content of $PC_{61}BM$ was varied.

$PC_{61}BM$ content (%)	**V_{OC} (V)**	**J_{SC} (mA.cm^{-2})**	**FF (%)**	**PCE (%)**
33	0.86	-0.95	23.19	0.19
50	0.55	-1.53	27.26	0.23
67	0.80	-2.03	22.14	0.36
75	0.72	-6.03	30. 05	1.31

Table 4.4: A summary of results for C2B1·$PC_{71}BM$ based OPV cells, under AM1.5G illumination (100 mW.cm^{-2}). The content of $PC_{71}BM$ was varied.

$PC_{71}BM$ content (%)	**V_{OC} (V)**	**J_{SC} (mA.cm^{-2})**	**FF (%)**	**PCE (%)**
33	0.88	-1.27	23.24	0.26
50	0.65	-3.38	30.01	0.66
67	0.80	-4.96	33.52	1.33
75	0.76	-6.05	33.48	1.54
86	0.67	-3.70	39.06	0.97

4.4.3.2 Effect of film thickness

C2B1 blended with $PC_{61}BM$ or $PC_{71}BM$ were spin-cast at different speeds, to obtain different active layer thicknesses. Varying the spin speed affects a number of properties including absorption, film morphology, drying conditions and film uniformity. A maximum thickness normally exists for BHJ active layers, with thicker layers having increased absorption. Conversely, non-geminate recombination increases for thicker layers, as free charge carriers recombine before reaching their respective electrodes.

Spin speeds were varied from 1500 RPM to 3000 RPM for both C2B1 with $PC_{61}BM$ or $PC_{71}BM$, with a fullerene content fixed at 75%. This led to a surprisingly small variation in measured thickness, ranging from 105 nm to 135 nm. An optimum film thickness of 125 nm was found by spin-casting at 2250 RPM for 60 seconds (measured with Dektak surface profilometer in OMIC, University of Manchester). Based on this film thickness and fullerene content, the annealing conditions were also varied. It was found that the optimum annealing temperature was 80°C, which is similar to that reported for the polymer of this oligomer, PC2B1 and also PCPDTBT [134].

Figure 4.6 shows the I-V characteristics for the best performing $C2B1{\cdot}PC_{61}BM$ and $C2B1{\cdot}PC_{71}BM$ cells under AM1.5G illumination after optimisation. The best performing blend ratio was with a fullerene content of 75%, where PCEs of 1.31% and 1.54% were measured for $PC_{61}BM$ and $PC_{71}BM$. These values were obtained from OPV cells without active layer processing additives for morphological control. It is, therefore, possible that PCE could be increased by a factor of two, when considering the effect of processing additives for other materials.

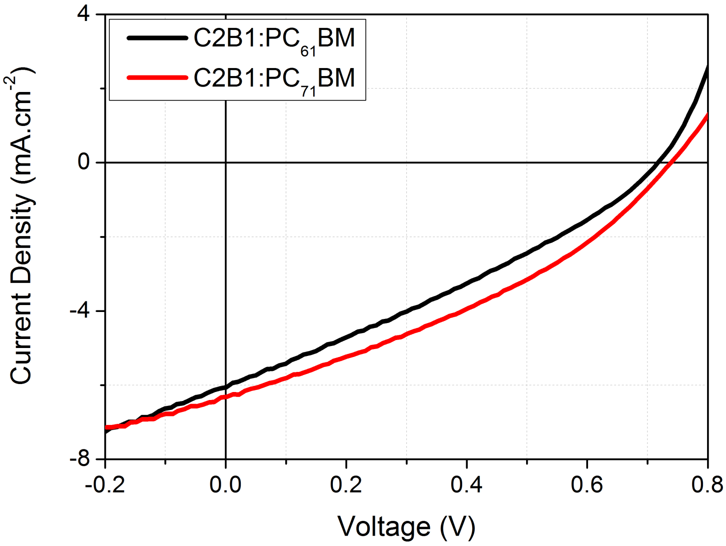

Figure 4.6: I-V characteristics of the best-performing cells deposited from solutions of C2B1 with PC$_{61}$BM or PC$_{71}$BM under AM1.5G conditions. C2B1·PC$_{71}$BM has increased V_{OC}, J_{SC} and FF. Both cells were cast from anhydrous chlorobenzene solution (30 mg.mL^{-1}) and filtered prior to coating.

4.4.4 Morphological studies using AFM

To understand the variations in performance, surface roughness measurements of C2B1 OPV cells were made using AFM topography scans. Figure 4.7 shows the different surface morphologies for the best performing cells of C2B1 with PC$_{61}$BM or PC$_{71}$BM, and thermally evaporated C2B1 and C_{60}.

The roughness of the spin-cast films are similar with R_A of 0.333 nm and R_Q of 0.267 nm, and R_A of 0.425 nm and R_Q of 0.315 nm for C2B1 with PC$_{61}$BM and PC$_{71}$BM, respectively. AFM topographic scans were also taken of the top surface of a thermally evaporated C2B1:C_{60} bilayer, and showed a R_A of 1.36 nm and R_Q of 1.06 nm. It is clear that the evaporated bilayer OPV cell exhibits a much higher surface roughness, which is likely to be a factor in the reduced performance.

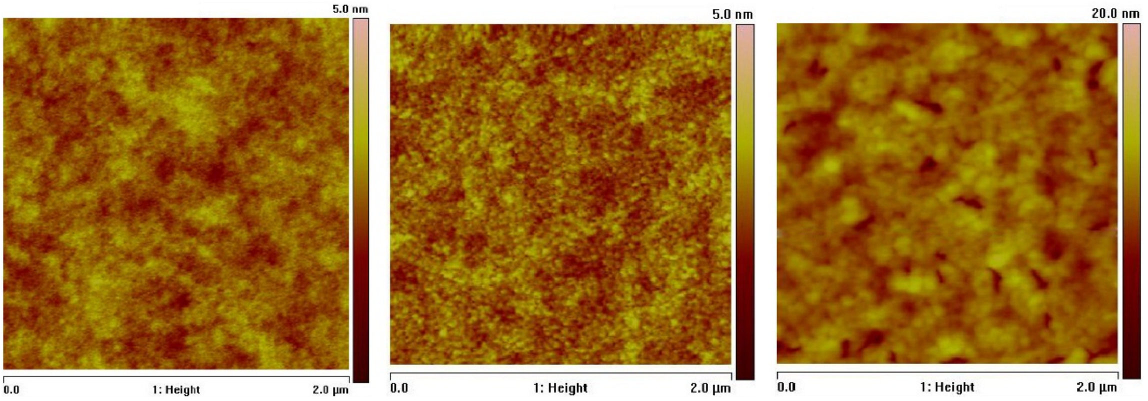

Figure 4.7: Comparison of AFM topography of best performing cells of C2B1·$PC_{61}BM$ (left); C2B1·$PC_{71}BM$ (middle); C2B1 and then C_{60} thermally evaporated (right). AFM data give similar surface roughness values for C2B1·$PC_{61}BM$ (R_A = 0.333 nm, R_Q = 0.267 nm) and C2B1·$PC_{71}BM$ (R_A = 0.425 nm, R_Q = 0.315 nm). Thermal evaporation of C2B1 and C_{60} yielded a surface roughness values of R_A = 1.36 nm and R_Q = 1.06 nm.

4.4.5 Morphological studies using WAXS

WAXS was used to investigate the nature of the molecular stacking and structure of C2B1 thin films, pristine and blended with $PC_{61}BM$. Crystallographic studies on CPDT-based polymers have been of heavy recent interest, and it was hoped that by studying the properties of C2B1, an insight into polymer crystallography could be obtained. Data from the Cambridge Crystallographic Data Centre (CCDC) were used to simulate the expected diffraction patterns for C2B1, comparing them to the obtained WAXS measurement. The simulated model is shown in Figure 4.8. (The simulation was developed by Masaki Horie and Jeff Kettle.)

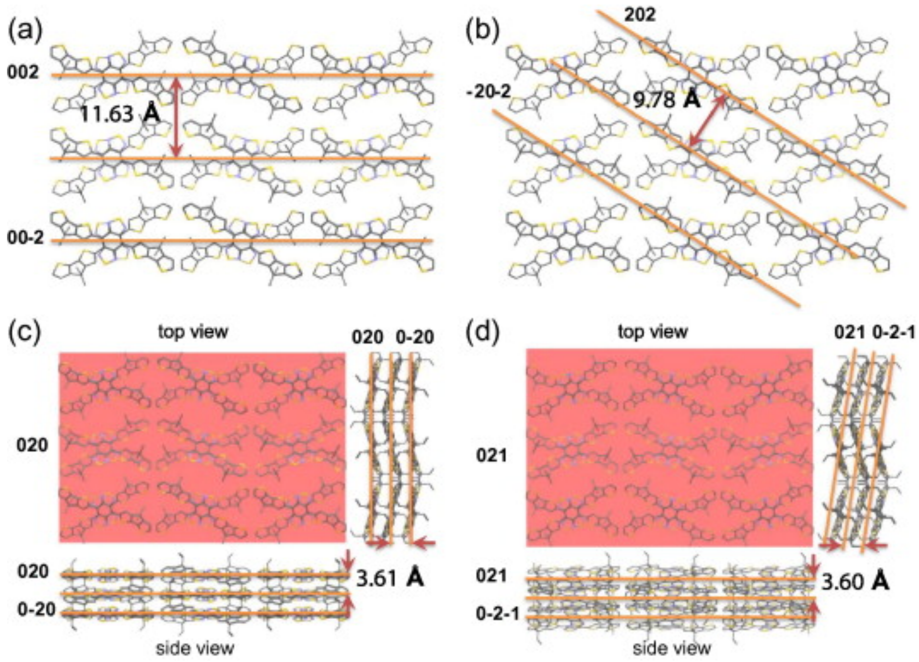

Figure 4.8: The packing structure of C2B1 and corresponding Miller indices. a) and b) show the top view, whereas c) and d) show the side views. Simulation work is by Masaki Horie.

Pristine films of C2B1 were spin-cast on Corning glass substrates and measured with WAXS. Data is shown in Figure 4.9. The films showed a broad feature with peaks at 2θ = 9° and 23°, corresponding to 9.7 Å and 3.9 Å, respectively. Based on correlating the Bangor experimental data with the simulation from Masaki Horie and Jeff Kettle, the peak at 2θ = 9° is attributed to Miller indices (002) and (202), corresponding to the vertical intermolecular spacing. The peak at 2θ = 23° is mainly attributed to Miller indices (020) and (021), corresponding to the horizontal π-stacking between oligomers. The relative peak intensity at $2\theta = 23^{o}$ increased slightly for films of C2B1·$PC_{61}BM$, whereas it decreased slightly for $2\theta = 9^{o}$, inferring the formation of stronger π-stacking and weaker vertical interaction because of bulky $PC_{61}BM$. Peaks corresponding to (212) and (213) planes at 2θ = 15° and 18° were not significant, probably due to weakened long-range π-π stacking in thin films. The XRD patterns of the polymer equivalent showed peak positions at $2\theta = 9^{o}$ and 23^{o} [134], similar to C2B1. It was therefore concluded that a similar packing structure for C2B1 is maintained even in the related polymers.

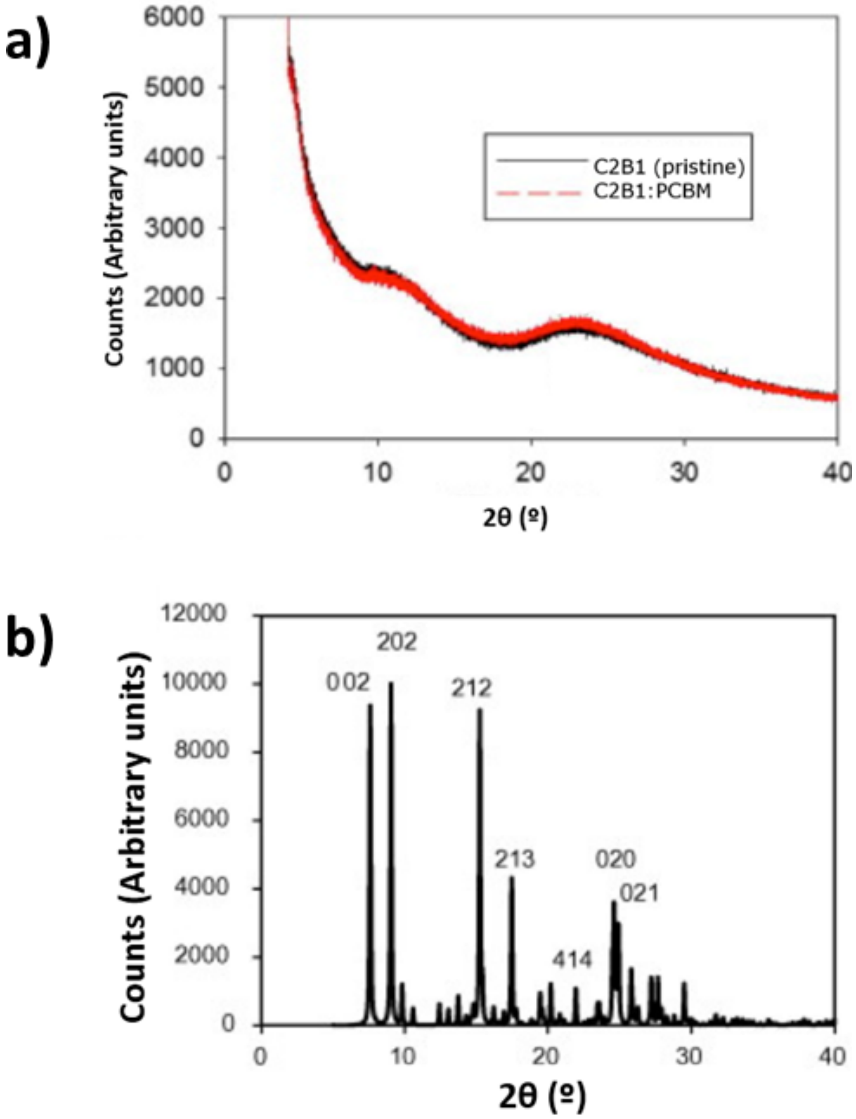

Figure 4.9: Comparison of XRD patterns of C2B1 and C2B1·$PC_{61}BM$ films respectively, spin cast from chlorobenzene solution and dried at room temperature in a glovebox (a). Simulation work using CCDC data showing the expected interference patterns of C2B1 (b).

4.5 PCPDTBT synthesised by direct arylation

Section 4.1 focused on the use of oligomers as donor materials in OPV cells. This was an attempt to see if oligomers could provide an alternative to polymers for CPDT-BT solar cells. However, the performance was low, and no further work was undertaken on oligomers during this thesis. As the focus of the thesis was on lifetime testing, large quantities of reproducible materials were needed for experiments. Therefore, the remainder of this chapter is focussed on testing polymer based OPV cells using direct-arylated polymer.

In this section of the thesis, OPV cell data for PCPDTBT synthesised via Pd catalysed direct arylation between CPDT and BT is reported. For the first time, OPV cell characteristics of direct arylation polymers are compared to those synthesised via Suzuki coupling.

4.5.1 OPV cells processed without additives

Initial experiments with PCPDTBT synthesised using direct arylation, were conducted on OPV cells without the ODT processing additive. OPV cells including processing additives are difficult to optimise, since an additional variable is introduced. PCPDTBT was received using slightly modified synthetic routes. Over 20 polymers were received for testing, however, material filtering was conducted to ensure only those with molecular weights (M_n) in excess of 10,000 were used to make OPV cells. A summary of OPV cell performance is given in Table 4.5. Entry **1** gave the best performance and was shown to be superior to the PCPDTBT control polymer, synthesised using the more commonly used Suzuki-coupling route.

The working devices made from entries in Table 4.5, are the first known report of working OPV cells using directly arylated polymers. The highest PCE was observed for the polymer with the highest molecular weight (PCE = 2.24%, M_n of 38k in entry 1), representing a moderate enhancement in performance over the Suzuki-coupled polymer (2.01%). For many materials, a higher molecular weight of conjugated polymers is one crucial factor in obtaining high-performing organic electronic devices. Previous reports of PCPDTBT with larger molecular weights ($M_n > 30,000$) have shown the best performing OPV cells. Apart from entry **1**, all other polymers exhibited $M_n < 20,000$. There was no consistency in how M_n affects OPV cell performance at these low values, as the synthetic routes probably left slightly different impurity residues, or required further synthetic optimisation. It is unlikely that a polymer with M_n < 20,000 could exceed the performance of entry **1**, even with further device processing optimisation.

Table 4.5: Shown are the molecular weight, product yield and OPV cell performance for polymers synthesised using direct arylation techniques. Reaction condition dictates the polymer characteristics.

a) Calculated from gel-permeation chromatography (GPC). Measurements carried out using THF as the solvent and calibrated by polystyrene standards. M_n, after Soxhlet extraction is noted in brackets.

b) Yield before Soxhlet extraction is shown.

c) Average PCE (with standard deviation) from a minimum of 8 six pixel cells was obtained from OPV cells fabricated from chlorobenzene solutions of PCPDTBT and $PC_{71}BM$ (1:3 weight ratio) with a structure of ITO/PEDOT·PSS/PCPDTBT·$PC_{61}BM$/Ca/Al under AM1.5G conditions in air at room temperature. Best PCE value is noted in brackets.

Entry	M_n [a)]	**Yield (%)** [b)]	λ_{MAX} **(nm)**	**PCE with $PC_{71}BM$ (%)** [c)]
1	37700 (71700)	76	704 (732)	2.01 ± 0.15 (2.24)
2	18000 (22400)	87	703 (734)	1.78 ± 0.20 (1.95)
3	18500 (22400)	76	697 (720)	1.48 ± 0.19 (1.62)
4	15700	70	708 (722)	1.76 ± 0.21 (1.95)
5	18100	76	704 (731)	1.21 ± 0.09 (1.27)
6	15800	98	694 (717)	1.39 ± 0.11 (1.48)
Suzuki	15300	83	693 (722)	1.95 ± 0.11 (2.01)

4.5.2 OPV cells processed with additives

Polymers obtained in entries **1** and **2** in Table 4.5 were blended with $PC_{71}BM$ at 3% weight and dissolved in chlorobenzene, with the addition of 2.5% weight of ODT. These solutions were used to fabricate OPV cells where entry **1** yielded a PCE of 4.23% (see Figure 4.10), which is slightly higher than for the polymer synthesised *via* Suzuki reaction (3.89%) reported previously [118]. Entry **2** did not work as well, demonstrating a maximum PCE of 3.1% from OPV cells made with the material. The improvement in performance over the control polymer is attributed to the higher molecular weight, which is accomplished by the direct arylation synthetic route. Table 4.6 summarises the average performance of PCPDTBT-based OPV cells, synthesised using Suzuki or direct arylation coupling.

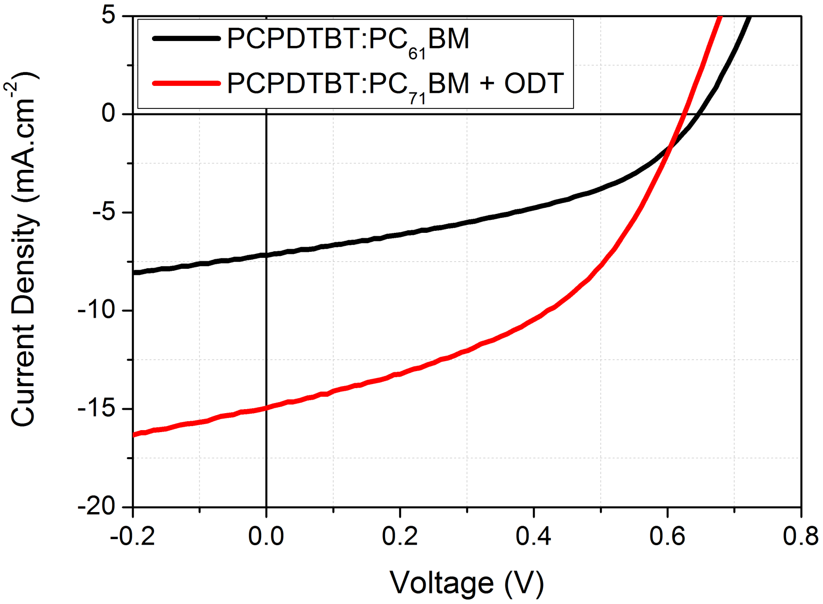

Figure 4.10: I-V characteristics under AM1.5G (100 mW.cm^{-2}) of the polymer from entry **1** in Table 4.5, deposited from solution with PC$_{71}$BM without (2.01%) and with 25 mg.mL^{-1} of ODT (3.98%) under AM1.5G illumination. Cells were cast from anhydrous chlorobenzene solution (30 mg.mL^{-1}).

In an attempt to further improve the performance, active layer thicknesses of directly-arylated PCPDTBT were varied. Figure 4.11 (a) shows how when V_{OC} and FF remains relatively constant, that PCE is mostly determined by the J_{SC}, [Figure 4.11 (b)], hence photon absorption. The optimum thickness of entry **1** in Table 4.5 for PCPDTBT·PC$_{71}$BM, with ODT, was approximately 120 nm. The lack of variation in V_{OC} is unsurprising, but it is for the FF. Variations in active layer thickness would be expected to result in different series and shunt resistances, affecting FF. This could be as a result of the polymer's higher molecular weight.

Table 4.6: The average performance of PCPDTBT-based OPV cells made using Suzuki or direct arylation coupling. A comparison of performance with and without the ODT processing additive is also shown. All cells were fabricated at the same time and characterised under AM1.5G illumination (100mW.cm^{-2}). An average of 6 cells is used for all data.

Synthesis	Processing Additive	V_{OC} (V)	J_{SC} (mA.cm^{-2})	FF (%)	PCE (%)
Suzuki (M_n = 15300)	No ODT	0.611	-6.92	43.8	1.95
	ODT	0.640	-12.71	46.0	3.74
Direct arylation (M_n = 71700)	No ODT	0.606	-7.98	41.1	2.01
	ODT	0.627	-13.92	45.5	3.98

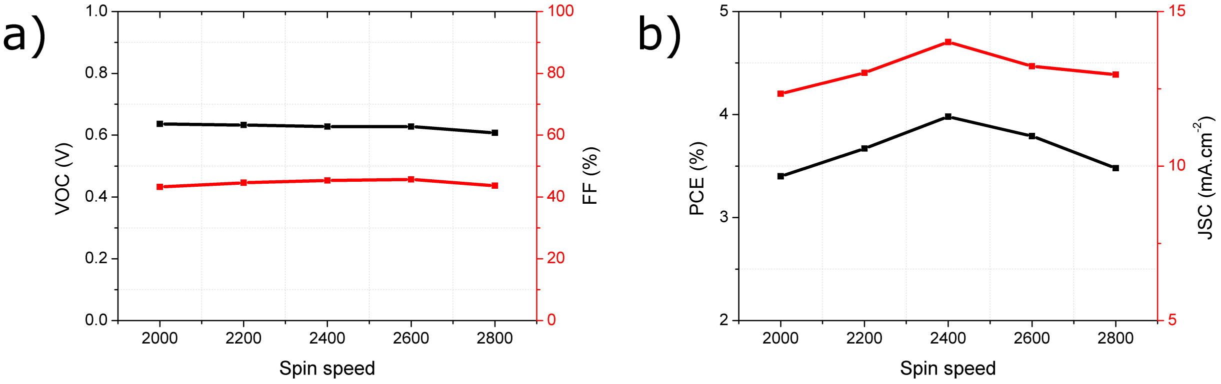

Figure 4.11: The V_{OC} FF (a), and J_{SC} and PCE (b) are shown as a function of active layer thickness for PCPDTBT·PC$_{71}$BM with ODT. A peak is found at 120 nm, given by spin casting at 2400 RPM. Below 120 nm, insufficient photons are absorbed. Above 120 nm, electrons and holes recombine before collection.

4.5.3 Hole mobility measurements

Finally, hole mobility measurements were conducted on the polymer from entry **1**. Previous measurements of hole mobility in C2B1 were conducted using OFET devices, enabling comparison with other published data for CPDT-BT analogues [80, 81, 112, 113, 118]. For the remainder of this thesis, SCLC devices were used. OFET charge carriers move from the source to the drain, parallel to the substrate, along the plane of the organic film. OPV cell charge moves between the electrodes in a direction perpendicular to the substrate. It was therefore decided to focus on SCLC devices, as the charge transport is in an identical direction to that seen in OPV cells [205].

Directly arylated PCPDTBT films in SCLC devices were annealed at different temperatures, to determine the conditions needed to obtain the maximum hole mobility. SCLC devices were biased from -2 to + 10 V under dark conditions, and the resulting current measured. Figure 4.12 shows a plot of the logarithm (base 10) of the measured current against the logarithm (base 10) of effective voltage. It was possible to apply linear fits showing the linear (red) and SCLC (blue) regions, as described in section 3.3.8. Figure 4.12 demonstrates that current is space-charge limited, facilitating the use of the Mott-Gurney law.

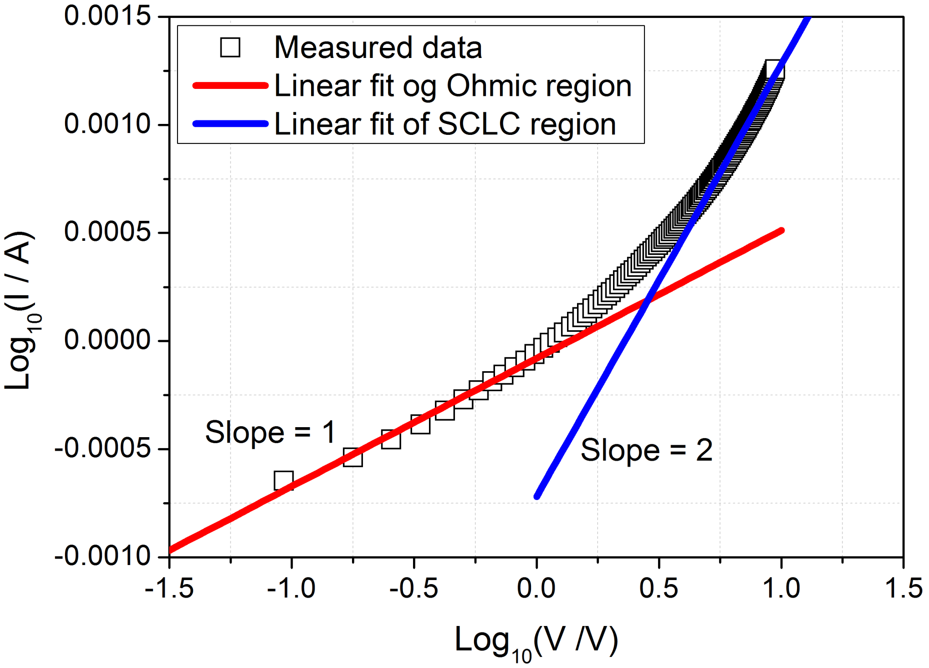

Figure 4.12: The current flow in SCLC devices is space-charge limited, as demonstrated by the gradient of the linear fit for the SCLC region (Slope = 2) being twice that of the gradient for the fit of the Ohmic region (Slope = 1). Films annealed at 25°C demonstrated a maximum hole mobility value of 1 x 10^{-5} $cm^2.V^{-1}.s^{-1}$ (b). Similar results were observed for SCLC devices annealed at other temperatures (not shown).

A maximum hole mobility of 1.1 x 10^{-5} cm^2 V^{-1} s^{-1} was measured, for films dried at 120°C for 1 hour (see Figure 4.13). Drying conditions have an effect on the morphology of the active layer and subsequent mobility. Figure 4.13 shows the effect of drying conditions on mobility. Interestingly, very little change in mobility is observed with increasing temperature, which contradicts previous reports for this material. This could be as a result of the higher molecular weight, which increases the polymer entanglement, ensuring it is less susceptible to changes at high temperatures. Drying conditions have a moderate effect on the polymer morphology and subsequent mobility, with ~25% relative change over the temperature range. Kettle et al. [118], have shown Suzuki-coupled PCPDTBT to possess a mobility of 2 × 10^{-5} $cm^2.V^{-1}.s^{-1}$, when measured using SCLC devices, indicating slightly superior charge transport properties.

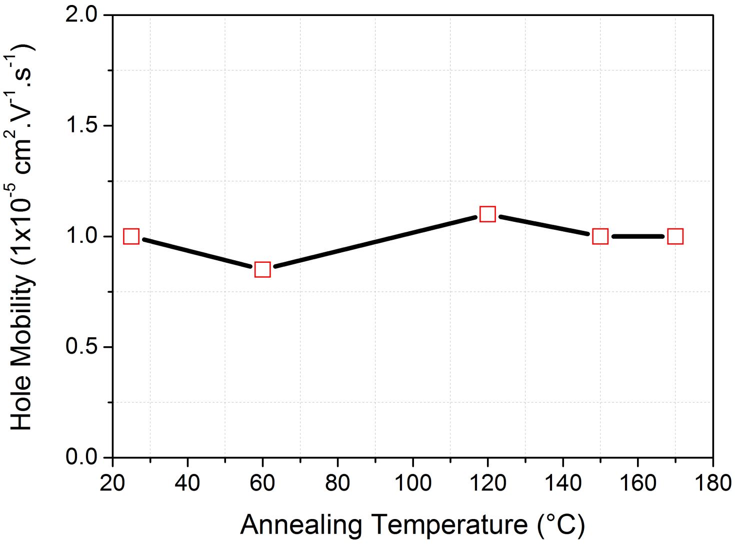

Figure 4.13: The change in mobility as a function of drying temperature (1 hour dry time). It can be seen that the hole mobility of directly-arylated PCPDTBT is relatively stable across a range of temperatures.

4.6 Summary

In this chapter, materials based on CPDT and BT units were analysed and used to fabricate OPV cells. In the first part, the work focused on the use of D-A-D oligomer as a donor material in OPV cells. The optical absorption measurements of CPDT-BT-CPDT (C2B1) indicate an energy gap of 1.8 eV, indicating the material capable of 4.5% PCE in an OPV device. Solvatochromism behaviour was also observed in this oligomer. Evaporated and solution-processed OFET devices made using this material and measured in the saturation region yielded hole mobilities of 3.2×10^{-4} cm^2 V^{-1} s^{-1} and 5.0×10^{-3} cm^2 V^{-1} s^{-1}, respectively. Subsequently, evaporative OPV devices were fabricated, using C_{60} as the acceptor material leading to very low maximum PCE of 0.04%. Topographic AFM scans showed the evaporative layers to be very rough. Due to the low performance, C2B1 was blended with $PC_{71}BM$ and cast from solution, leading to a PCE of 1.57%. The best performing solution processed cells for every case had an optimum oligomer to fullerene ratio of 1:3 and active layer thickness of approximately 125 nm. WAXS was also performed on films of C2B1 with and without $PC_{71}BM$. Masaki Horie's model along with data from the Cambridge Crystallographic Data Centre (CCDC) was used to assist in identifying the peaks attributed to vertical intermolecular spacing and horizontal π-stacking. $PC_{71}BM$ inclusion leads to weaker vertical interaction and stronger π-stacking, due to the bulkiness of this molecule. C2B1 gave diffraction patterns similar to PCPDTBT, inferring similar molecular packing.

Due to the poor performance of oligomers, the remainder of this work focused on polymer based cells. Directly-arylated PCPDTBT was characterised and used to fabricate SCLC and OPV devices. The best performing polymer materials demonstrated a PCE of 2.24%, compared to the Suzuki-coupled, which was measured at 1.98%. This corresponded to the polymer with the highest molecular weight (M_n = 38k). The performance was increased by blending the polymer with $PC_{71}BM$ and ODT, which led to a PCE of 4.23%. It appears that the optimal processing conditions for directly arylated PCPDTBT were similar to those used for the control material, despite the variation in molecular weight between the two materials.

Chapter 5 Lifetime studies of PCPDTBT based solar cells

5.1 Introduction

In this chapter, the lifetimes of PCPDTBT-based OPV cells were studied using a combination of device data and analytical techniques. Most investigations on OPV cell lifetimes have focused on the donor materials P3HT [55, 206, 207], PCDTBT [46, 208, 209], CuPc [210–212], or polyfluorene [213]. Therefore, the work here provides insight into degradation characteristics and mechanisms for a new OPV material.

For most reported high-performing OPV cells, processing additives, normally based on functionalised alkanes, are used to optimise the active layer morphology. The previous chapter showed that processing additives such as ODT increases the PCE of PCPDTBT-based cells by almost a factor two. This improvement has been shown in almost all prominent papers on OPV cells, with other active layer materials such as P3HT, PCDTBT and PTB7 [81, 214, 215]. To date, no work has looked at how the use of processing additives affects OPV cell lifetime. This is critical if processing additives are to be used in the commercialisation of the technology.

In this chapter, the effect of additives was investigated, and its influence on PCPDTBT-based solar cells is reported. As the lifetime is shown to decrease when processing additives are included in the initial blended solution, strategies to improve stability using alternative naphthalene-based additives have been trialled. The fabrication of inverted cells has also been undertaken, with lifetime again shown to be poorer when additives are used. For all OPV cells, failure was defined as when performance reached 10% of its original value ($T_{10\%}$). Finally, a number of analytical techniques are used to investigate chemical and physical degradation routes in PCPDTBT-based OPV cells.

5.2 Effect of processing additives upon lifetime

5.2.1 Lifetimes of non-encapsulated cells

Six-pixel OPV cells were made with P3HT·$PC_{61}BM$, and PCPDTBT·$PC_{71}BM$ with and without ODT. Initial cell characterisation was conducted under AM1.5G illumination (100 mW.cm^{-2}), and light soaking performed using a halogen light source. During testing, the temperature and humidity were measured but not controlled as 50 ± 5ºC and 40 ± 5%. The initial performances under AM1.5G are shown in Table 5.1, with lifetime data normalised from starting values shown in Figure 5.1. P3HT·$PC_{61}BM$-based cells were included as a comparison, providing a relative benchmark for PCPDTBT stability during light soaking experiments.

Figure 5.1 shows the relative change in the V_{OC}, J_{SC}, FF and PCE for cells made with active layers of P3HT·$PC_{61}BM$, and PCPDTBT·$PC_{71}BM$ with and without ODT. The PCE of PCPDTBT-based solar cells with and without ODT appear to decrease quicker than for P3HT:$PC_{61}BM$-based solar cell, indicating they have a lower overall stability. OPV cell half-life ($T_{50\%}$) is defined as the time taken for the PCE to halve from its original value. This is estimated as 126 hours for P3HT:$PC_{61}BM$, 46 hours for PCPDTBT:$PC_{71}BM$, and 25 hours of PCPDTBT:$PC_{71}BM$ with ODT.

Table 5.1: The mean initial parameters for typical cells made with P3HT·$PC_{61}BM$, PCPDTBT·$PC_{71}BM$, or PCPDTBT·$PC_{71}BM$ with ODT respectively, tested under AM1.5G illumination (100mW.cm^{-2}). Data are averaged from a minimum of six cells.

	P3HT·$PC_{61}BM$	**PCPDTBT·$PC_{71}BM$**	**PCPDTBT·$PC_{71}BM$ with ODT**
V_{OC} (V)	0.50 ± 0.10	0.63 ± 0.01	0.63 ± 0.01
J_{SC} (mA.cm^{-2})	-11.41 ± 2.47	-8.11 ± 0.46	-13.26 ± 1.33
FF (%)	52.12 ± 16.54	43.04 ± 0.57	46.43 ± 0.71
PCE (%)	3.05 ± 0.69	2.20 ± 0.12	3.89 ± 0.34

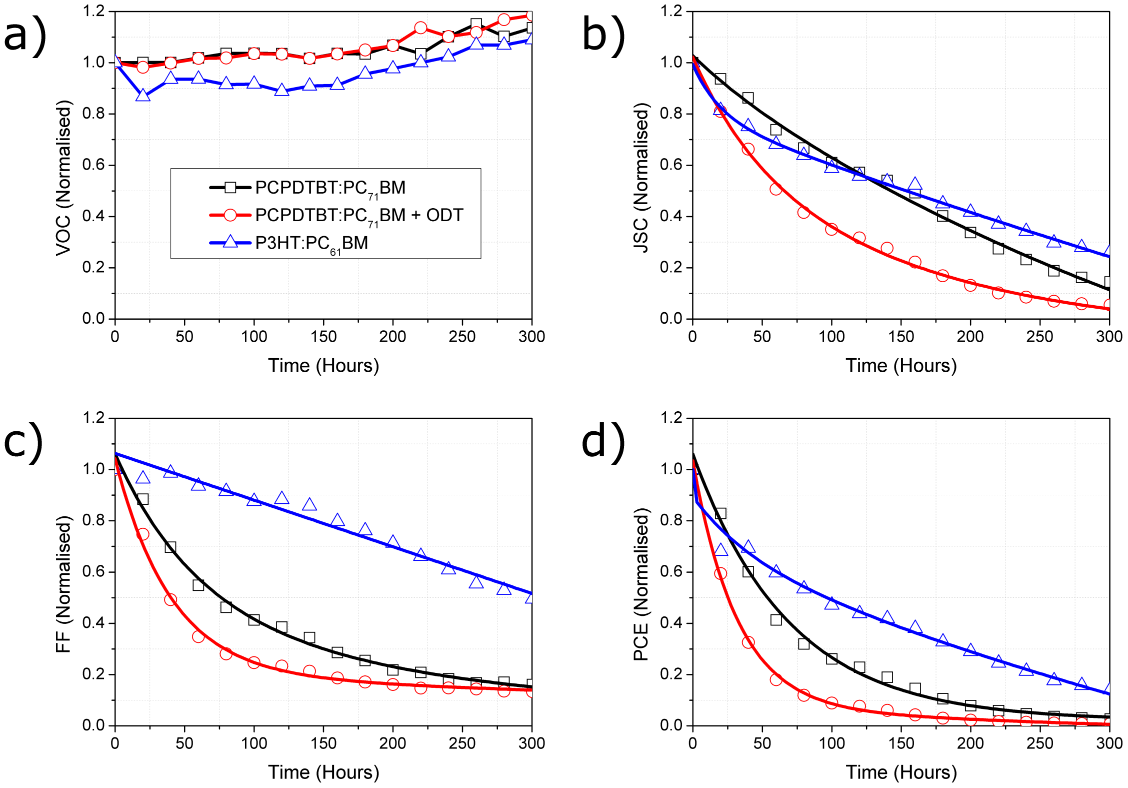

Figure 5.1: OPV cell performance during light soaking over a 300 hour period, under 1 Sun of irradiance at 50°C ± 5°C. Showing a) V_{OC}, b) J_{SC}, c) FF and d) PCE for six-pixel cells made with P3HT·$PC_{61}BM$, PCPDTBT·$PC_{71}BM$, and PCPDTBT·$PC_{71}BM$ with ODT. The parameters are normalised to their starting values.

Considering the individual solar cell parameters, V_{OC} appears to increase slowly with time for all cells, with both PCPDTBT cells matching each other's degradation characteristics closely. Since the P3HT- and PCPDTBT-based cells used the same interfacial layers and electrodes, the change in V_{OC} is likely to be as a result of a chemical change in the donor active material. This change has also been witnessed in other polymer-fullerene solar cells. An increasing V_{OC} infers that the HOMO of the polymer (in this case PCPDTBT) is lowering with time. A lowering of the HOMO could be a result of several factors, such as the formation of new species as a result of reactions with water or molecular oxygen, or the loss of conjugation from polymer scission [23].

Although the degradation characteristics of V_{OC} for both PCPDTBT-based cells are similar to one another, the changes in J_{SC} and FF are very dissimilar. Both the FF and the J_{SC}

of PCPDTBT·$PC_{71}BM$ with ODT decrease faster with time compared to the cells without ODT.

Both devices without and with ODT were tested under the same conditions. ODT acts as a solvent for PCBM and is not known to be chemically reactive with either PCBM or PCPDTBT. The greater drop in FF with time suggests that the morphology of the active layer with ODT is less stable. This is important to note, as processing additives are widely reported in literature, due to its ability to improve initial PCE. Differential scanning calorimetry (DSC) indicates that PCPDTBT does not morphologically change significantly upon heating, even up to 220°C [216]. Additionally, no obvious changes in the colour of the cells were observed following light soaking suggesting no increase in photo-bleaching or loss of optical absorption. This suggests that the loss in performance is due to morphological changes as a result of the presence of ODT.

A metric often used to evaluate OPV stability is the cell half-life ($T_{50\%}$), which is defined as the time taken for the PCE to halve from its original value. This is calculated as 46 hours for the PCPDTBT·$PC_{71}BM$ cells and 25 hours for the cells of PCPDTBT·$PC_{71}BM$ with ODT. Although OPV cells made from PCPDTBT·$PC_{71}BM$ with ODT exhibit reduced stability compared to those without ODT, their initial performance (when measured under AM1.5G illumination) is much higher. Therefore, a more suitable metric to evaluate their relative performance could be to calculate the total power generated over a cell's lifetime. Over the lifetime of the fabricated cells (defined as $T_{10\%}$), the power output of those without ODT was 150 $mWh.cm^{-2}$, while the cell with ODT generated the lesser amount of 131 $mWh.cm^{-2}$. Despite the initial performance of cells made with ODT being much greater, the faster degradation leads to lower power output over its lifetime. In fact, after only 47 hours of operation during light soaking experiments, the power generation of cells made without overtook those with ODT.

5.2.2 Encapsulation and modification of shadow mask

To evaluate if ambient air influences the stability of OPV cells made with processing additives, light soaking experiments were conducted using an encapsulated three-pixel design. Three pixel OPV cells were encapsulated in a glovebox prior to light soaking, using UV curable epoxy.

5.2.3 Lifetimes of encapsulated cells

Three pixel OPV cells made with P3HT·PC$_{61}$BM, and PCPDTBT·PC$_{71}$BM with and without ODT were also stability tested after encapsulation. As in section 5.2.1, the architecture consisted of ITO/PEDOT·PSS/active layer/Ca/Al, along with an identical lifetime test procedure. Data are shown in Table 5.2 and Figure 5.2. P3HT·PC$_{61}$BM-based cells were included as a comparison and provided a relative benchmark for the stability of PCPDTBT during light soaking.

Table 5.2: Mean initial parameters for typical encapsulated cells of P3HT·PC$_{61}$BM, PCPDTBT·PC$_{71}$BM, and PCPDTBT·PC$_{71}$BM with ODT respectively, when tested under AM1.5G illumination. Data are averaged from a minimum of six cells.

	P3HT·PC$_{61}$BM	**PCPDTBT·PC$_{71}$BM**	**PCPDTBT·PC$_{71}$BM with ODT**
V_{OC} (V)	0.59 ± 0.01	0.57 ± 0.07	0.60 ± 0.01
J_{SC} (mA.cm^{-2})	-13.01 ± 1.52	-7.37 ± 0.87	-13.06 ± 1.07
FF	0.57 ± 0.02	0.39 ± 0.04	0.46 ± 0.01
PCE (%)	4.38 ± 0.60	1.78 ± 0.18	3.78 ± 0.22

Table 5.2 shows the initial OPV cell under AM1.5G illumination (100 mW.cm^{-2}). When comparing data with that in Table 5.1, encapsulation and the change from six to three pixel OPV configuration had little if any effect on performance. Figure 5.2 shows the relative

change in V_{OC}, J_{SC}, FF and PCE for cells made with P3HT·PC$_{61}$BM, PCPDTBT·PC$_{71}$BM, and PCPDTBT·PC$_{71}$BM with ODT. The experiment was run for 1000 hours, with no cells dropping to 10% of their original PCE, demonstrating the integrity of the encapsulation procedure.

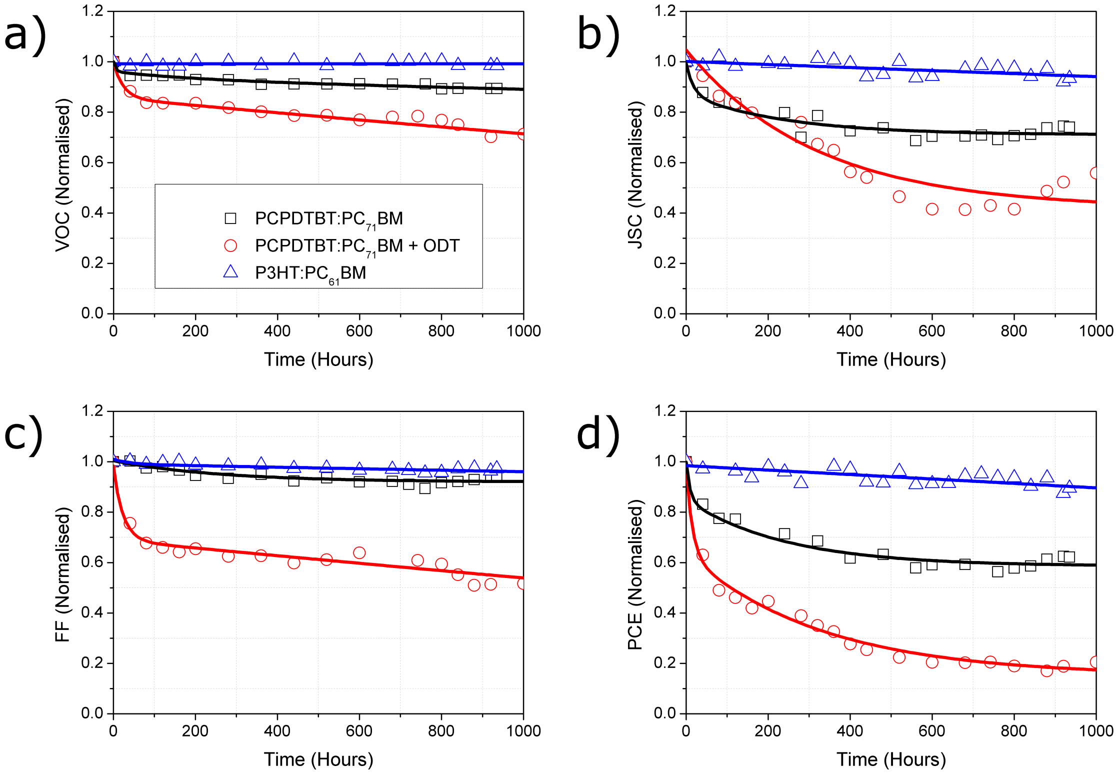

Figure 5.2: OPV cell performance during light soaking for 1000 hours under 1 Sun of irradiance at 50°C ± 5°C. Showing a) V_{OC}, b) J_{SC}, c) FF and d) PCE for three pixel cells using P3HT·PC$_{61}$BM, PCPDTBT·PC$_{71}$BM, and PCPDTBT·PC$_{71}$BM with ODT. The parameters are normalised to their starting values.

For P3HT·PC$_{61}$BM OPV cells, V_{OC}, J_{SC}, FF and PCE remain very stable. However, PCPDTBT·PCBM based OPV cells show different degradation pathways. There is a distinct difference in the change of FF over time between cells made with PCPDTBT·PC$_{71}$BM and those with PCPDTBT·PC$_{71}$BM including ODT. The significant change in FF with time once again suggests that the active layer, which includes ODT, is more prone to changes with times.

Cells of PCPDTBT·PC$_{71}$BM and PCPDTBT·PC$_{71}$BM with and without ODT exhibit a reduction in J$_{SC}$, with a more pronounced change during the first 200-300 hours. This is not observed for P3HT·PC$_{61}$BM cells. This drop has been observed by other groups, who reported that amorphous polymer-based solar cells have a noticeable burn-in phase [209, 217]. This phenomenon was demonstrated to be an interface effect, where a reaction between the cathode and active layer led to the formation of hole traps. Even after the *burn-in* period, degradation continues and is likely to be due to photo-oxidation by molecular oxygen and water, degradation of the electrodes or other factors.

The V$_{OC}$ appears to be stable for P3HT·PC$_{61}$BM, but somewhat unstable for PCPDTBT-based cells. PCPDTBT·PC$_{71}$BM based OPV cells exhibit a small decrease in V$_{OC}$, with the cell of PCPDTBT·PC$_{71}$BM with ODT showing a greater change.

Overall due to the changes in V$_{OC}$, J$_{SC}$ and FF, the PCE of cells made using the ODT additive exhibit the worst lifetimes, which is consistent with the cells tested in section 5.2.1. When comparing the overall power generation during the lifetime, OPV cells made without ODT exhibit better performance as well, despite the lower initial efficiency. Over 1000 hours operation, cells with ODT generated 840 mWh.cm^{-2}, whereas those without ODT generated 1457 mWh.cm^{-2}.

Since the overall trends for encapsulated and non-encapsulated cells were similar, it was therefore decided not to encapsulate further OPV cells for this thesis. This also gave an opportunity to directly probe the active layer surface of OPV cells with time, using techniques such as AFM.

5.2.4 External quantum efficiency (EQE)

In addition to I–V characterisation, a series of EQE measurements were made as part of the lifetime study on the non-encapsulated cells. As measurements needed to be conducted at varying times of the day, Dr Jeff Kettle assisted in acquiring EQE data. EQE allowed the spectral response of the active layer to measure the amount of free charge carriers per photon per wavelength. OPV cells were fabricated, left under a light soaker and periodically measured. Between measurements, the cells were disconnected, and periodic I-V characteristics were not taken (as in sections 5.2.1 and 5.2.3). Due to the absence of electrical stressing from repeated I-V sweeps, the cells exhibited improved lifetimes, indicating that electrical stressing is another cause of degradation.

Spectral response was recorded as a function of time. The EQE of cells made from PCPDTBT·PC_{71}BM without and with ODT were compared. Figure 5.3 shows EQE as a function of time. The general shape of the curve at zero hours similar to previous reports for this material [84, 218], and shows the effect of PCPDTBT, which enables photo-absorption up to 900 nm. The inclusion of ODT increases the photocurrent across the visible [219–221].

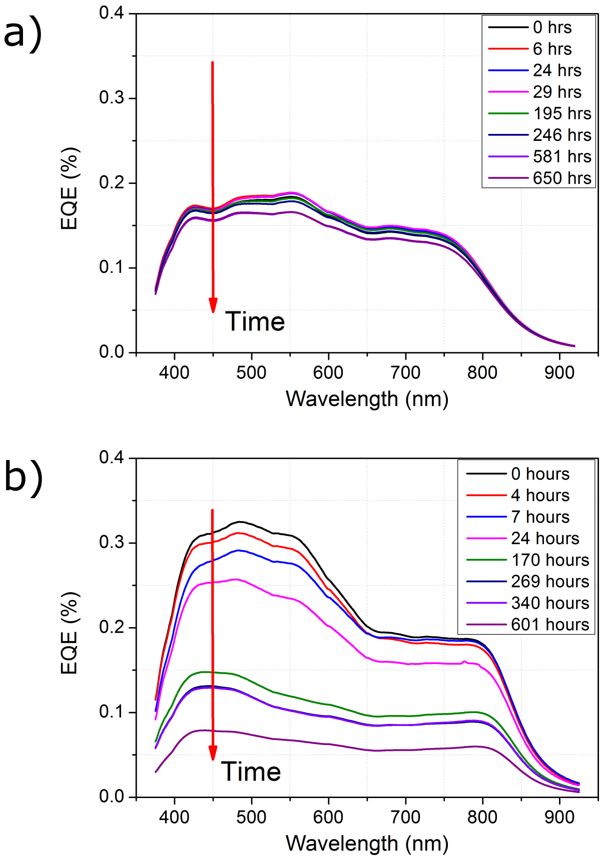

Figure 5.3: EQE change with time during light soaking, for OPV cells of PCPDTBT·PC_{71}BM made without (a) and with ODT (b). Overall the spectral response across the optical region is greater for the cell with ODT. With time, the cell without ODT remains relatively stable while the inclusion of ODT leads to dramatic changes,

During light soaking tests, the general shapes of the curves changed only slightly, with the overall spectral features present at 0 hours still recognisable after 600 hours. Based on the data in Figure 5.3, the EQE response at the peak PCPDTBT and $PC_{71}BM$ absorption wavelengths (793 nm and 483 nm respectively) are plotted as a function of time. It can be seen that cells made without ODT show good overall stability. Both PCBM and PCPDTBT degrade a little, at a similar rate, demonstrating that one component is not changing quicker than the other. Cells made with ODT possess a much lower intrinsic stability, degrading more rapidly than cells without ODT. Both PCPDTBT·$PC_{71}BM$ cells showed slower degradation at $\lambda = 793$ nm (corresponding to the peak PCPDTBT absorption), than at $\lambda = 483$ nm. Therefore, $PC_{71}BM$ is shown to be the lesser stable component of the active layer. This infers that the loss in photocurrent is a result of physical rather than chemical changes, since ODT does not react with either of the active layer constituents.

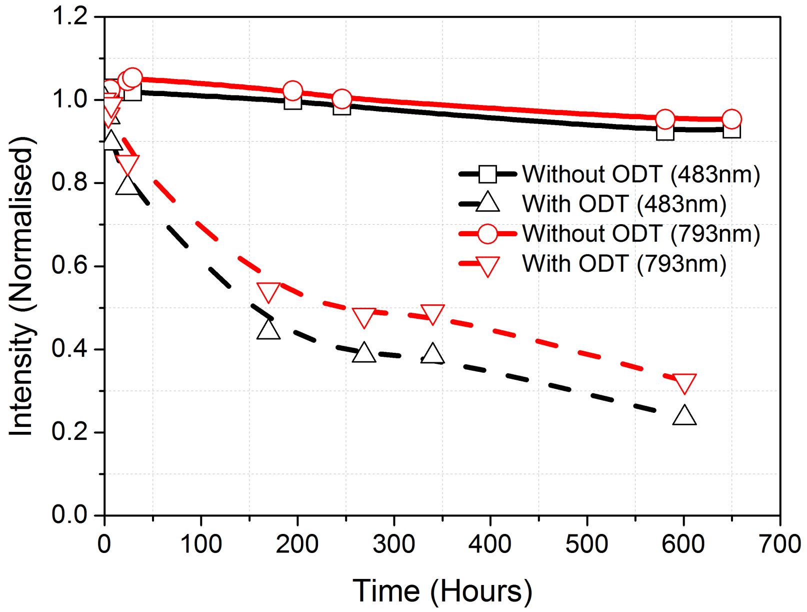

Figure 5.4: The change in EQE with time at wavelength 793 nm and 483 nm during light soaking experiments, corresponding to the peak absorption of PCPDTBT and $PC_{71}BM$. The inclusion of ODT results in cells with reduced intrinsic stability.

5.2.5 Morphological studies using AFM

Atomic force microscopy (AFM) was used to probe the surface roughness of non-encapsulated active layers of PCPDTBT·PC$_{71}$BM with and without ODT, before and after light soaking. AFM images were collected at 0 and 300 hours respectively, as shown in Figure 5.5. The first 300 hours corresponds to a timeframe when non-encapsulated OPV cells have generally reached less than 10% of their original performance.

Films of PCPDTBT:PC$_{71}$BM with ODT had initial surface (R_A) and peak-to-peak (R_{MAX}) roughness of 1.11 nm and 9.35 nm. After light soaking for 300 hours, these were reduced to $R_A = 0.63$ nm and $R_{MAX} = 7.08$ nm, relative decreases of 44% and 25% respectively. For comparison a cell without ODT had $R_A = 0.55$ nm and $R_{MAX} = 7.83$ nm prior to light soaking, which was reduced to $R_A = 0.47$ nm and $R_{MAX} = 7.62$ nm, relative changes of 16% and 3%, respectively. The smaller changes for cells without compared to those with ODT, suggest a more stable morphology during light soaking experiments.

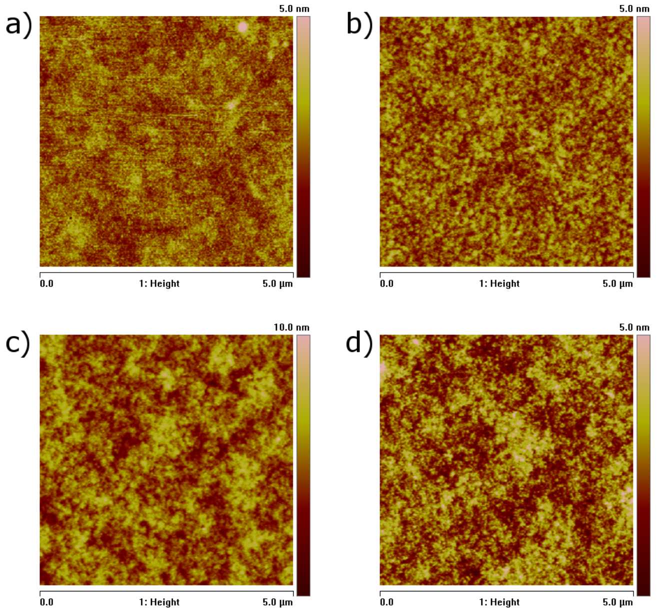

Figure 5.5: Atomic Force Microscope (AFM) topography of PCPDTBT·PC$_{71}$BM OPV cells without ODT (a) before and (b) after light soaking and PCPDTBT·PC$_{71}$BM OPV cells with ODT (c) before light soaking and (d) after light soaking. From measurements of surface roughness, a larger relative change in morphology of cells fabricated with ODT is observed.

5.2.6 Morphological studies using GISAXS/GIWAXS

Investigating the physical properties of PCPDTBT·$PC_{71}BM$ based OPV cells, such as photoconductivity and surface roughness, is limited as these are symptoms of more fundamental reactions. Therefore, small- and wide-angle x-ray scattering (GISAXS/GIWAXS) were used to provide an insight into the causes at a molecular scale. Using facilities at the National Synchrotron Radiation Research Centre of Taiwan and the assistance of Dr U-Ser Jeng, the effect of light soaking on morphology was investigated. The experimental setup is briefly discussed in Chapter 3 and is a replication of those used by other groups [221, 222]. Samples were prepared at Bangor University and delivered within 48 hours in nitrogen sealed containers to Dr U-Ser Jeng. Films of PCPDTBT·$PC_{71}BM$ with and without ODT were cast upon PEDOT·PSS coated silicon, using the same procedures for preparing OPV cells.

Figure 5.6 (a) shows in-plane GISAXS profiles for the active layers of PCPDTBT·$PC_{71}BM$ with and without ODT, before and after light soaking in air for 300 hours. Dr U-Ser Jeng had previously investigated the competition between fullerene aggregation and P3HT crystallisation in BHJs, which was supported by TEM measurements [223]. OPV cell performance was correlated to morphological changes. The model used to describe PCBM aggregation was adjusted and fitted to the measured data. The data correlated to a model of spherical $PC_{71}BM$ aggregates, with an average diameter 14 ± 2 nm, for q_{xy} greater than 0.01 $Å^{-1}$. Prior to light soaking, the GISAXS profiles of active layers with and without ODT very closely overlap. From the GISAXS data in Figure 5.6 (a) it can be seen that light soaking results in an increased scattering intensity for both layers with and without ODT, inferring $PC_{71}BM$ aggregation [223, 224]. For the films processed with ODT, the scattering intensity for q_{xy} greater than 0.01 $Å^{-1}$ increases substantially, corresponding to smaller and compact $PC_{71}BM$ aggregates with an average size of 14 nm, as revealed by the sphere model fitting shown in Figure 5.6 (a) [222, 223, 225]. It is evident that the morphology of active layers processed with ODT is relatively unstable during light soaking.

Figure 5.6 (b) shows the corresponding normal-to-plane GIWAXS profiles for the same samples. The peak at 1.30 $Å^{-1}$ for the film processed without ODT moves to 1.15 $Å^{-1}$

for the film with ODT, inferring an increase in the intermolecular distance of $PC_{71}BM$ from 4.8 Å to 5.5 Å [223]. This effect may be attributed to less aggregated (or more dispersed) $PC_{71}BM$ in the film when spin coated with ODT [223]. After light soaking, the intermolecular distance for the sample with ODT decreased from 5.5 Å to 5.3 Å (the peak moved from 1.15 to 1.20 $Å^{-1}$) in Figure 5.6 (b), together with an increase in intensity. This change suggests increased $PC_{71}BM$ aggregation. In contrast, there is less change in the peak for the film processed without ODT. Once again, this indicates that films containing ODT lead to greater $PC_{71}BM$ aggregation during light soaking experiments. Overall, the film processed with ODT exhibited larger local and global morphological changes associated closely with $PC_{71}BM$.

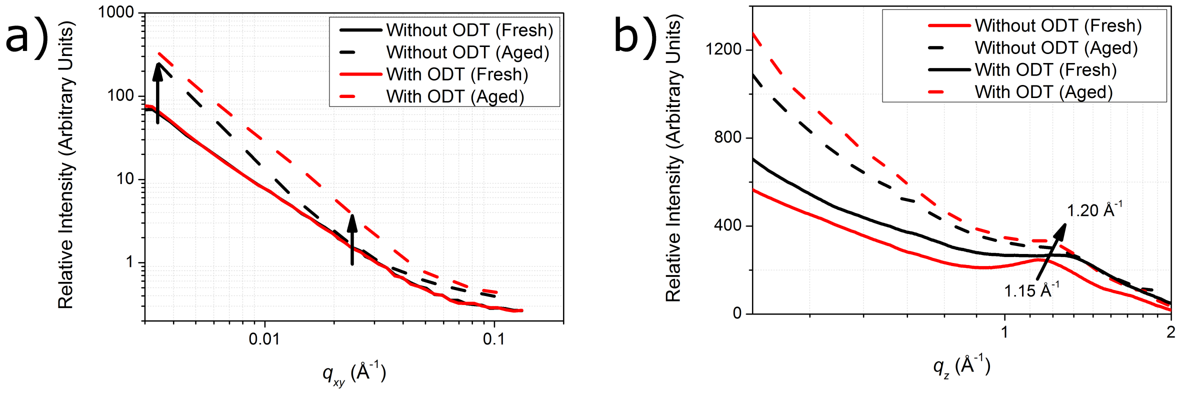

Figure 5.6: (a) GISAXS and (b) GIWAXS profiles of $PCPDTBT{\cdot}PC_{71}BM$ active layers with and without ODT, before and after light soaking for 300 hours. The arrows in (a) and (b) depict the scattering intensity growths in different in-plane q_{xy}-region and normal-to-plane q_z as a result of light soaking. GISAXS data for the light soaked film with ODT in (a) are fitted (solid curve) with a model of spherical PCBM aggregates.

5.2.7 Summary of morphological measurements

OPV cell light soaking data, AFM data and morphological measurements, indicate that $PCPDTBT{\cdot}PC_{71}BM$ layers made with ODT are less stable than those without. ODT possesses a boiling temperature of 270°C and is unlikely to evaporate at the low processing temperatures used during cell fabrication, or even under the high vacuum required for Ca/Al cathode evaporation. It is, therefore, probable that ODT resides in the active layer up to the point of testing. This conclusion is supported by Cho et al. [226], who showed that ODT was not completely removed from active layer films when subjected to high vacuum (10^{-6} Torr).

Based on these observations, residual ODT in the active layer will selectively dissolve the $PC_{71}BM$ component, leading to increased aggregation. Increased aggregation ultimately leads to a reduction in the connectivity of $PC_{71}BM$ percolation networks, limiting the amount of charge extracted from the active layer [84]. EQE measurements helped support this conclusion, by showing PCBM to be the lesser stable component of the active layer. Therefore, in order to fabricate stable PCPDTBT·$PC_{71}BM$ cells made with ODT, it might be necessary to remove the ODT after processing. This could pose difficulties as ODT has a high boiling temperature, and PCPDTBT·$PC_{71}BM$ based OPV cells tend to decrease in performance with increased temperatures [118].

5.3 Alternative processing additives for enhanced stability

5.3.1 Introduction

PCPDTBT with ODT was shown to increase the PCE of OPV cells in Chapter 4, as a result of *controlling* active layer morphology, leading to enhanced J_{SC} and FF. PCE increases have also been observed for other processing additives, such as octane (C_8H_{18}), DIO ($I\text{-}C_8H_{16}\text{-}I$), dibromooctane ($Br\text{-}C_8H_{16}\text{-}Br$) and dichlorooctane ($Cl\text{-}C_8H_{16}\text{-}Cl$). Performance increases with these processing additives are often less than those obtained with ODT. The previous section showed that these processing additives have a negative impact on OPV cell lifetimes. Therefore, this section investigates the use of alternative processing additives to investigate if efficiency can be increased, without compromising OPV cell lifetime. In particular, the work is targeted at lower boiling-point processing additives, as these are more likely to evaporate than ODT.

5.3.2 I-V characterisation

Two new processing additives were trialled for PCPDTBT:$PC_{71}BM$ based OPV cells. Separate solutions of PCPDTBT:$PC_{71}BM$ with 2.5% of 1-chloronaphthalene (ClN) or 1-bromonaphthalene (BrN) were prepared, with chlorobenzene remaining as the host solvent. Both ClN and BrN are shown to be good solvents for PCBM [227]. The film thickness (as a function of spin casting speed) was optimised using the same procedures used in Chapter 4.

PCPDTBT·$PC_{71}BM$ with ClN or BrN were spin-cast and subjected to different annealing condition. These were: 80ºC or 140ºC for one hour. Previous work on PCPDTBT·$PC_{71}BM$ with ODT has indicated that 80ºC led to the optimum morphology and solar cell performance. Since ClN and BrN have boiling points (B.P.) of 111ºC and 133ºC respectively, annealing at 140ºC was chosen to ensure removal of all processing additive solvent.

Table 5.3 shows the OPV cell performance obtained from PCPDTBT:$PC_{71}BM$ with ODT, ClN or BrN under AM1.5G conditions (100mW.cm^{-2}). For all three processing additives, the best performance was obtained using annealing at 80ºC. Annealing at 140ºC led to a decrease in PCE of approximately 20% for all cells.

Table 5.3: Mean and standard deviation value for PCPDTBT·$PC_{71}BM$ based cells cast with 1-chloronaphthalene (ClN) and 1-bromonaphthalene (BrN) processing additives respectively. PCPDTBT·$PC_{71}BM$ cast with ODT was included as a control. OPV cells were characterised under AM1.5G conditions (100mW.cm^{-2}).

	ClN	BrN	ODT
V_{OC} (V)	0.64 ± 0.01	0.63 ± 0.01	0.62 ± 0.00
J_{SC} (mA.cm^{-2})	-7.71 ± 0.29	-7.20 ± 0.28	-9.05 ± 0.38
FF (%)	46.53 ± 1.04	38.00 ± 2.78	51.05 ± 0.88
PCE (%)	2.30 ± 0.07	1.72 ± 0.20	2.95 ± 0.10
Boiling point (ºC)	111	133	270

As can be seen with data in Table 5.3, the difference in PCE between the cells made with different processing additives is largely determined by variations in FF, suggesting considerable morphological variance. OPV devices with ODT yielded the highest PCE, due to increased J_{SC} and FF compared to those that included ClN or BrN. It is worth noting that the performances of these cells are slightly lower than the previous section due to issues with the glovebox, resulting in high oxygen levels.

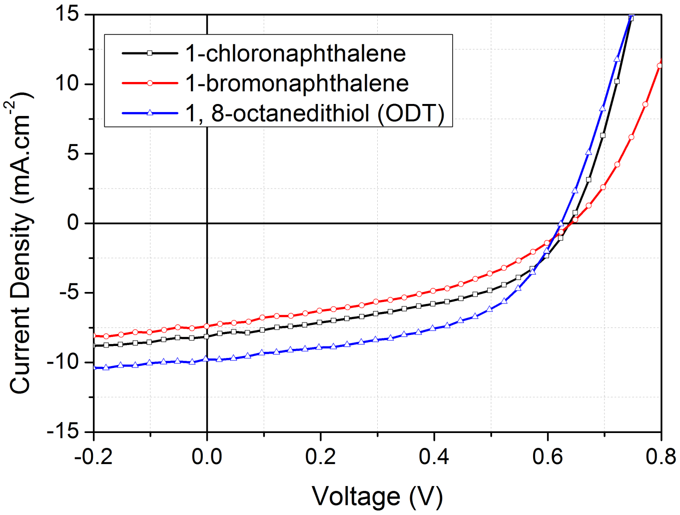

Figure 5.7: I-V characteristics under AM1.5G for the best performing cells of PCPDTBT·PC_{71}BM made with 1-chloronpahthalene, 1-bromonaphtahlene or ODT.

5.3.3 Lifetime analysis

In addition to optimising fabrication conditions, OPV cells of PCPDTBT·PC_{71}BM with ClN or BrN were tested for stability. Experiments were conducted in an identical manner to section 5.2. All OPV cells were light soaked with I-V measurements performed every 30 minutes.

Figure 5.8 shows how the V_{OC}, J_{SC}, FF and PCE changed with time for cells made using ClN or BrN. It appears that layers made with BrN gives the greatest stability. Unfortunately, this gives the lowest initial PCE (see Table 5.3). The $T_{50\%}$ for the best performing cells made with ClN and BrN was measured to be 90 hours and 115 hours. Cells made with ODT had a $T_{50\%}$ of 25 hours. The most stable OPV cells made with ClN and BrN were obtained by annealing at 80°C. This shows that 'over-annealing' to remove as much of the processing additive as possible from the active layer does not necessarily lead to improved stability. Higher temperature annealing may instigate a different degradation mechanism.

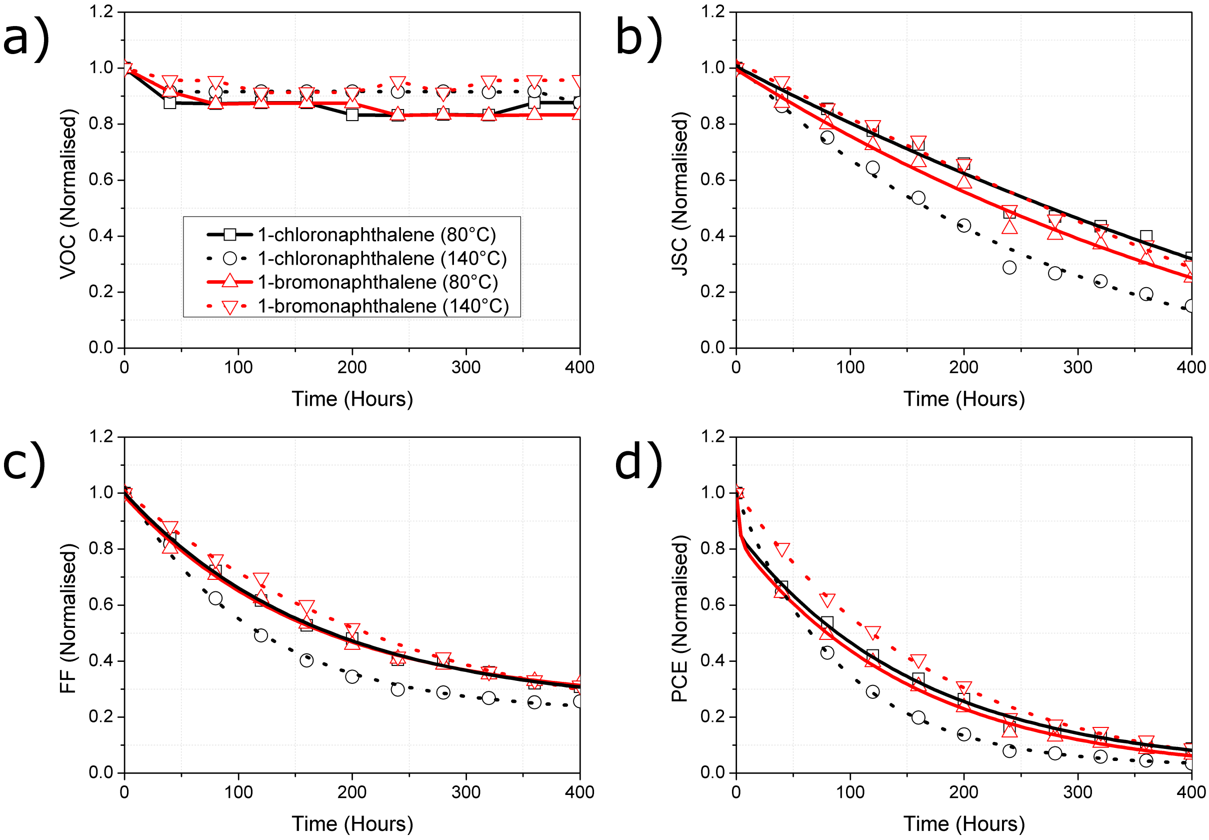

Figure 5.8: OPV cell characteristics for PCPDTBT:$PC_{71}BM$ made with ClN or BrN processing additives. Shown are the variations of the V_{OC} (a), J_{SC} (b), FF (c) and PCE (d) with time, all normalised from their starting values. Although changes in the J_{SC} and FF are observed, the greater fall in the FF suggests that morphological changes are the primary cause of performance reduction.

Table 5.4 shows the change in PCE with time for the best performing PCPDTBT·$PC_{71}BM$ cells, with ClN, BrN and ODT respectively. The variation in PCE with time for OPVs made with ClN, BrN and ODT is shown in Figure 5.9, which provides a more succinct summary of the stability improvements by moving to naphthalene-based additives.

The data for PCPDTBT·PC$_{71}$BM cells with ODT is taken from section 5.2.1. In Figure 5.9, it is evident that the cells made with ODT possess substantially worse stability. Although ODT shows reduced stability, its initial PCE is at least twice that of cells using either ClN or BrN. Therefore, the total power generation over the individual cells' lifetime is again considered. A cell's lifetime is defined as between the period of zero hours until T$_{10\%}$ is reached and this data is shown in Table 5.4. From the data in Table 5.4, it is observed that devices made with ClN exhibit the best power generating capabilities. While devices made with BrN have a greater stability, and those made with ODT possess higher PCE, the use of ClN appears to give the best trade-off between stability and performance.

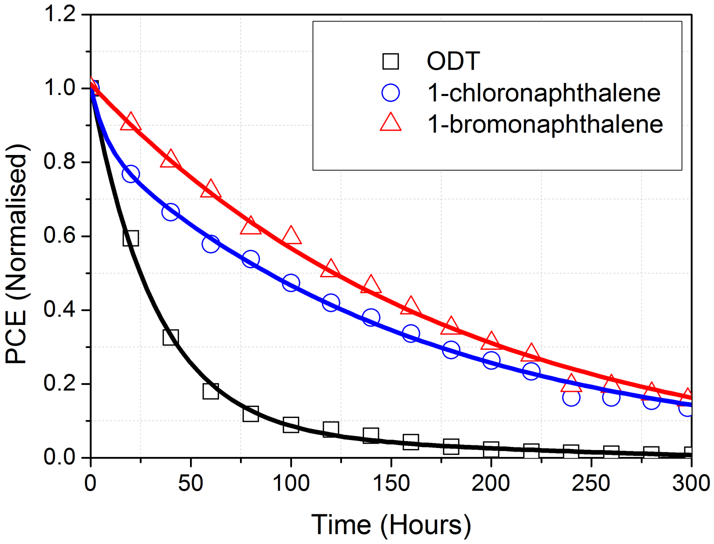

Figure 5.9: The change in PCE with time for the best performing cells of PCPDTBT·PC$_{71}$BM cast with 1-chloronaphthalene, 1-bromonapthalene and ODT respectively. Too few data are available to demonstrate a trend, mostly due to the significant difference in physical properties of ODT and naphthalene-based additives.

Table 5.4: The sum of the electrical power generated over the first 1000 hours of PCPDTBT·$PC_{71}BM$ cells, made with 1-chloronaphthalene, 1-bromonaphthalene and ODT respectively. Also included are the approximate times until total OPV cell failure, and additive boiling temperatures (B.T.).

Additive	**Time to reach 50% of initial PCE ($T_{50\%}$) [hours]**	**Estimated electrical power generated until $T_{10\%}$ ($mWh.cm^{-2}$)**	**B.P. (°C)**
1-chloronaphthalene	88.63	292.56	111
1-bromonaphthalene	121.47	260.58	139
ODT	24.75	130.93	270

5.3.4 Morphological studies using AFM

AFM analyses were conducted on the surfaces of PCPDTBT·$PC_{71}BM$ based films, which had been cast with ClN, BrN or ODT. Figure 5.10 shows topographical images of these films for scan areas of 5μm x 5μm. It can be seen from Figure 5.10 (a) and (b) that films made with ClN exhibit the greatest surface roughness. This would suggest less optimum morphology due to the aggregation of PCPDTBT and PCBM phases, which explains the lower PCE of these cells.

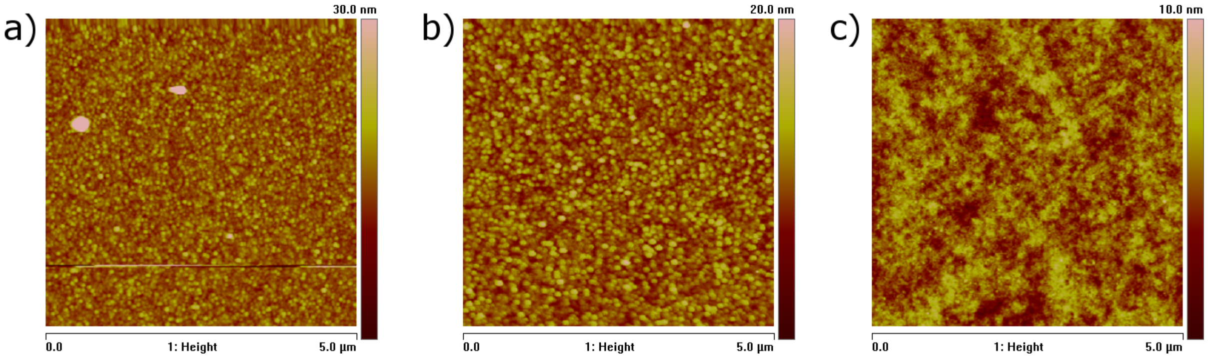

Figure 5.10: Topographic scans using AFM for films of PCPDTBT·$PC_{71}BM$ with 1-chloronaphthalene (a), 1-bromonaphthalene (b), or ODT (c).

After 300 hours of light soaking, films made with ClN had a surface roughness (R_A) of 2.47 nm and a peak-to-peak roughness (R_{MAX}) of 68.3 nm; BrN had R_A = 1.91 nm and R_{MAX} = 16.9 nm; and ODT had R_A = 0.78 nm and R_{MAX} = 6.78 nm. PCPDTBT·$PC_{71}BM$ cast with ODT shows the smoothest topographies, whereas PCPDTBT·$PC_{71}BM$ with ClN is the roughest. A trend can be seen of smoother topographies with increasing boiling temperature (111ºC, 133ºC and 270ºC for ClN, BrN and ODT respectively), likely related to additive volatility.

5.4 Inverted PCPDTBT-based OPV cells

5.4.1 Introduction

All cells fabricated and tested so far used a *non-inverted* structure, where the HTL was in contact with the ITO electrode and the ETL/cathode in contact with air. As both Ca and Al are low work function materials, they are more susceptible to oxidation and, therefore, undesirable for long-term stability. *Inverting* the OPV cell structure ensures that the high work function HTL and anode now act as the air-facing electrode, reducing the susceptibility of devices to environmental degradation [228].

5.4.2 I-V characterisation

In order to construct *inverted* OPV cells, ZnO was used as the ETL. To determine the optimum ZnO layer thickness, several thicknesses were sputtered upon ITO covered glass, which were then used to make OPV cells. PCPDTBT·$PC_{71}BM$ was spin cast, with MoO_3 and Ag thermally evaporated to give a top electrode. The optimum ZnO thickness was found to be 20 nm, with mean and standard deviation values for 12 cells shown in Table 5.5.

Thicker ZnO layers led to a reduction in performance, as a result of decreased FF from higher series resistances. It was not possible to fabricate working OPV cells with thinner ZnO layers due to high shunts, suggesting a discontinuous film. The J_{SC} is similar for all cells, implying similar photon absorption and charge generation, which is a function of the active layer. This also demonstrated the transparency of ZnO across the visible spectrum, regardless of thickness.

Table 5.5: I-V characterisation of PCPDTBT·$PC_{71}BM$ based OPV cells made with ZnO of varying thickness. 20 nm was found to be the optimum due to the increased FF, hence more efficient charge extraction.

ZnO Layer Thickness (nm)	**20**	**40**	**60**
V_{OC} (V)	0.64 ± 0.02	0.58 ± 0.09	0.61 ± 0.04
J_{SC} (mA.cm^{-2})	-7.91 ± 0.18	-8.05 ± 0.29	-8.08 ± 0.33
FF (%)	42.17 ± 2.28	40.37 ± 2.09	38.13 ± 2.61
PCE (%)	2.13 ± 0.17	1.91 ± 0.38	1.88 ± 0.25

5.4.3 Lifetime analysis

ITO covered glass with 20 nm of ZnO were used to fabricate cells with active layers of PCPDTBT·$PC_{71}BM$ with and without ODT. These active layers were cast using the same method as in section 5.2.1. The I-V characteristics of these cells under AM1.5G illumination (100 mW.cm^{-2}) are shown in Table 5.6. OPV cell performance is slightly lower than previous reports due to a poorer glovebox atmosphere. These cells were subsequently light soaked using the same procedure in section 5.2.1 (see Figure 5.11).

Table 5.6: Shown are the I-V characteristics of inverted cells using 20 nm of ZnO with PCPDTBT·$PC_{71}BM$, with and without ODT.

	PCPDTBT·$PC_{71}BM$	**PCPDTBT·$PC_{71}BM$ with ODT**
V_{OC} (V)	0.61 ± 0.04	0.58 ± 0.00
J_{SC} (mA.cm^{-2})	-8.68 ± 0.27	-12.98 ± 0.15
FF (%)	40.57 ± 1.93	47.59 ± 1.21
PCE (%)	2.14 ± 0.17	3.57 ± 0.10

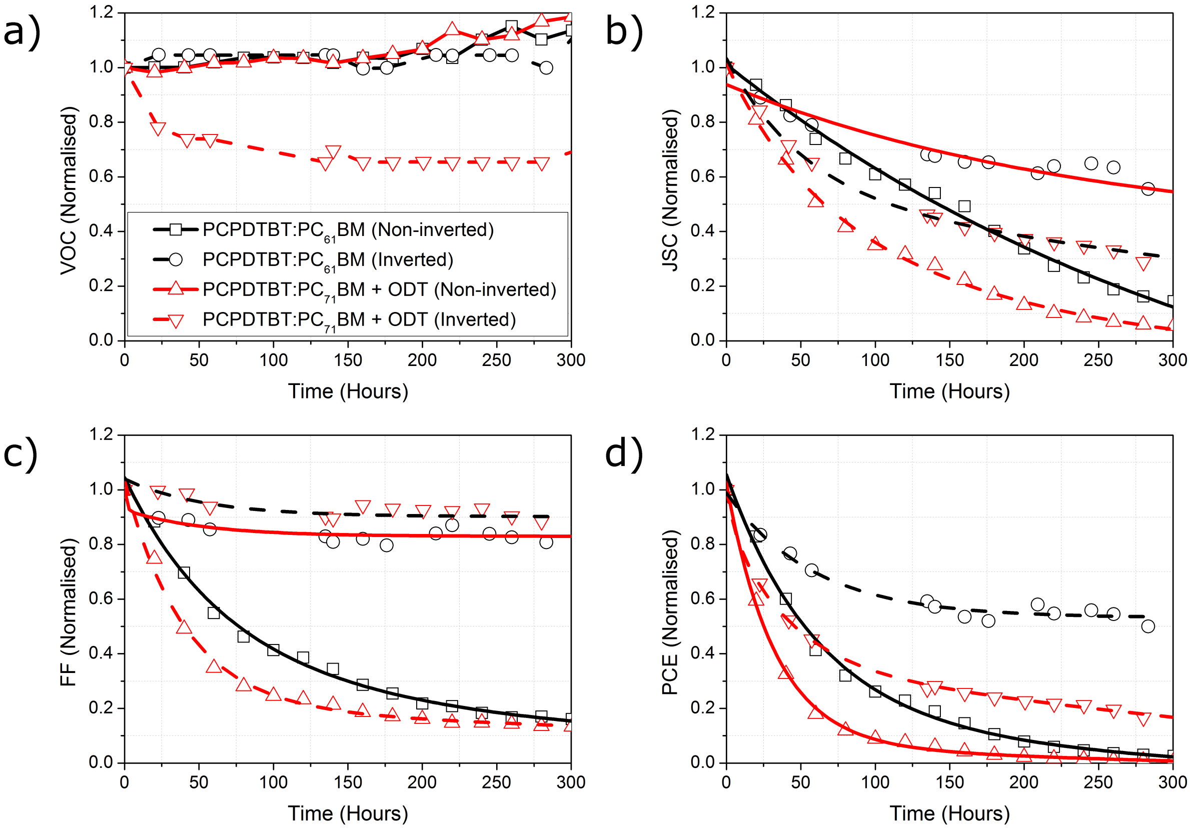

Figure 5.11: Comparisons of V_{OC}, J_{SC}, FF and PCE for cells of PCPDTBT·PC_{71}BM, with and without ODT respectively, using non-inverted and inverted structures. The inverted structure demonstrates significantly increased stability over the non-inverted structure.

Figure 5.11 shows how the main performance parameters for inverted cells change as a function of time, overlaid with data from section 5.2.1 for non-inverted cells. Immediately noticeable are two main trends. Firstly, inverted cells possess greater intrinsic stability and secondly, the inclusion of the ODT processing additive has a detrimental effect.

Considering firstly the effect of inverting the OPV architecture, PCPDTBT:PC_{71}BM-based with and without ODT show increased J_{SC} and FF stabilities, compared to their non-inverted equivalent. Several possibilities could be accountable for the improved stability of the J_{SC}. The MoO_3 and Ag may form a more effective seal directly above the area responsible for photocurrent. Water and oxygen have been found to diffuse through Al electrodes, via material grains [229]. The absence of Al and the use of Ag is likely to have the effect of impeding the diffusion of oxygen and water through to the active layer. The change in FF with time is also significantly reduced for inverted cells. This is likely to be due to the removal of reactive HTL and ETL. Both PEDOT·PSS and calcium are likely to degrade with environmental conditions causing the series resistance to increase, thus FF to reduce.

Inverted OPVs made with ODT are also shown to degrade quicker than those without, mirroring the trend observed for non-inverted devices in section 5.2.1. The dominant effect is that cells made with ODT exhibit a quicker reduction in J_{SC} and FF, presumably also as a result of PCBM aggregation.

One interesting result from Figure 5.11 is that the inverted device processed with ODT, shows a fall in V_{OC} with time, in contrast with data from the other three devices. Few reports on the stability of the PCPDTBT:PCBM-based solar cells are available. However, it is known from other materials such as P3HT, that a drop in V_{OC} can be attributed to a lowering of the polymer's HOMO, which is normally caused by oxygen absorption. As shown in the XPS data in section 5.5, ODT use led to a higher proportion of PCPDTBT at the top surface. PCPDTBT is, therefore, the most susceptible component of the active layer to oxidation. For non-inverted OPV cells, the ETL is deposited on top of the active layer. Any oxygen ingress is likely to react with the Ca first, which *protects* PCPDTBT from substantial oxidation, keeping the V_{OC} relatively constant. For inverted OPV cells, the air-stable MoO_3 is deposited on top of the active layer. Therefore, any oxygen ingress is likely to react with the polymer first, leading to increased polymer oxidation and drop in V_{OC}.

Table 5.7 shows the time taken for non-inverted and inverted cells of PCPDTBT·$PC_{71}BM$ with and without ODT respectively, to fall to 80% and 50% of their initial PCE ($T_{80\%}$ and $T_{50\%}$). The estimated total extractable electrical power until device failure ($T_{10\%}$) is also shown. Inverted cells are shown to generate more electrical power over their lifetimes, due to enhanced stability. When considering PCPDTBT:$PC_{71}BM$-based cells with ODT, the time taken to reach $T_{80\%}$ are similar for inverted and non-inverted architectures. However, the time taken to reach $T_{50\%}$ is greatly increased for devices made without ODT. This may suggest that the *burn-in* step is occurring due to changes in the active layer, rather than at the interfaces.

Table 5.7: The time elapsed for OPV cell PCE to fall to 80% and 50% of their initial values for non-inverted and inverted cells of PCPDTBT·PC$_{61}$BM, and PCPDTBT·PC$_{71}$BM with ODT respectively. Also shown is the total extractable electrical power of these cells for the first 1000 hours of accelerated lifetime tests.*Obtained from curve fitting for up to 2000 hours.

	PCE $T_{80\%}$ (Hours)	**PCE $T_{50\%}$ (Hours)**	**PCE $_{T10\%}$ (Hours)**	**Estimated electrical power generated until $T_{10\%}$ (mWh.cm^{-2})**
PCPDTBT·PC$_{71}$BM with ODT (Non-inverted)	8.48	24.75	92.28	131
PCPDTBT·PC$_{71}$BM with ODT (Inverted)	8.78	46.38	448.93	259
PCPDTBT·PC$_{71}$BM (Non-inverted)	19.28	52.28	184.56	150
PCPDTBT·PC$_{71}$BM (Inverted)	30.70	552.00	2847.06	2600*

5.5 XPS analyses of PCPDTBT based active layers

XPS is a useful tool for understanding the changes of chemical structures. In this section, data are presented to show the chemical changes evolving in illuminated PCPDTBT, in the presence of air. PC$_{61}$BM and PC$_{71}$BM were also studied, to understand the changes occurring in active layers as a whole.

The XPS results support previous studies in this chapter, showing the impact of processing conditions on the stability of PCPDTBT-based solar cells. The measurements for this work were conducted in collaboration with Professor Graham Smith at the University of Chester, with laboratory assistance by the author. Analysis was performed at Chester by Prof Graham Smith and the author over the duration of a fortnight. Upon data acquisition, CASA XPS software (Chester University licence) was used to fit curves to the observed signals. Curve intensities with respect to their binding energies were then compared to reference signals reported in literature for pure elements and common simple molecules. The exact references to use were advised in personal communications with Prof Graham Smith. It is worth noting that analysed films were not part of OPV cells and surfaces were, therefore, not sealed from the atmosphere by electrodes. This meant that the films were more exposed to atmospheric moisture and oxygen.

5.5.1 $PC_{61}BM$ and $PC_{71}BM$

Initial work focussed on using XPS to understand the chemical changes occurring in fullerene derivatives. Films of $PC_{61}BM$ and $PC_{71}BM$ were cast from a chlorobenzene solution onto PEDOT:PSS coated Corning glass substrates. The films were then light soaked under a halogen illumination source for 300 hours.

Table 5.8 shows the % atom concentration for PCBM at 0 and 300 hours. Stoichiometry suggests an oxygen concentration of 2.4 to 2.7% for both $PC_{61}BM$ and $PC_{71}BM$, present in the side chains. A slightly higher level of 3.6 to 3.7% was recorded suggesting some oxidation. Although film preparation was in a nitrogen glovebox, oxygen may have been introduced during transit to the XPS system.

After light soaking, there is a significant oxygen uptake in both $PC_{61}BM$ and $PC_{71}BM$, with an increase by a factor of 6.7 and 5.6 respectively. The highest oxygen uptake is observed in $PC_{61}BM$. Additionally, the nitrogen content goes from a negligible level that is beyond the sensitivity of the XPS system to 1.77% and 1.06% for $PC_{61}BM$ and $PC_{71}BM$. Sulphur also increases, with the signal just within the scope of the system’s sensitivity. It is inferred that $PC_{71}BM$ has greater stability, due to its lower uptake of oxygen, nitrogen and sulphur.

Table 5.8: The relative atom concentrations of $PC_{61}BM$ and $PC_{71}BM$ are shown for both fresh and aged cells. Overall nitrogen and oxygen increase in concentration, resulting in a proportional decrease in carbon and sulphur.

	Atom % concentration			
	0 hours		**300 hours**	
Name	**$PC_{61}BM$**	**$PC_{71}BM$**	**$PC_{61}BM$**	**$PC_{71}BM$**
O 1s	3.69	3.6	24.66	20.26
N 1s	-	-	1.77	1.06
C 1s	96.24	96.34	73.33	78.52
S 2p	0.07	0.06	0.24	0.16

The exact chemical changes, hence degradation mechanisms, can be deduced from the individual spectra for the respective elements. Figure 5.12 (a) shows the XPS spectrum for fresh carbon (C 1s), with a sharp and defined peak at 285 eV, corresponding to C-C bonds. The Gaussian-Lorentzian fitted curve has 70% Lorentzian behaviour, which is typical of partially ordered graphite-like materials [230]. There are also peaks at 286.7 eV and 288.8 eV, corresponding to O-C=O and –O-CH_3.

After light soaking, the intensities of the smaller peaks seen in fresh C 1s [Figure 5.12 (a)] have increased considerably, and can be seen prominently in aged C 1s [Figure 5.12 (b)]. The main peak at 285 eV has split up into two components of sp2 and sp3 carbon (from s1), corresponding to graphite-like and hydrocarbon-like carbon. These two components indicate the breaking of the C_{60} and C_{70} fullerenes and loss of molecular shape. Other peaks present with increased intensities have binding energies of 286.7 eV, 288 eV and 289.2 eV, corresponding to C-O, C=O and COO- respectively. Although present in non-aged films, their significant increase indicates strong oxidation of both $PC_{61}BM$ and $PC_{71}BM$.

XPS spectra for fresh and aged oxygen (O 1s) [Figure 5.12 (c) and (d)] show the same two components at 532 eV and 533.5 eV for C=O and C-O, but with different intensities. After light soaking the peaks have widened, suggesting C-O and C=O bonds present in a range of positions on the fullerene [230]. As well as the C-O and C=O present in the side chain, it could include C-O and C=O due to oxidation of the carbon atoms in the fullerene cage, but these two possibilities cannot be distinguished using XPS

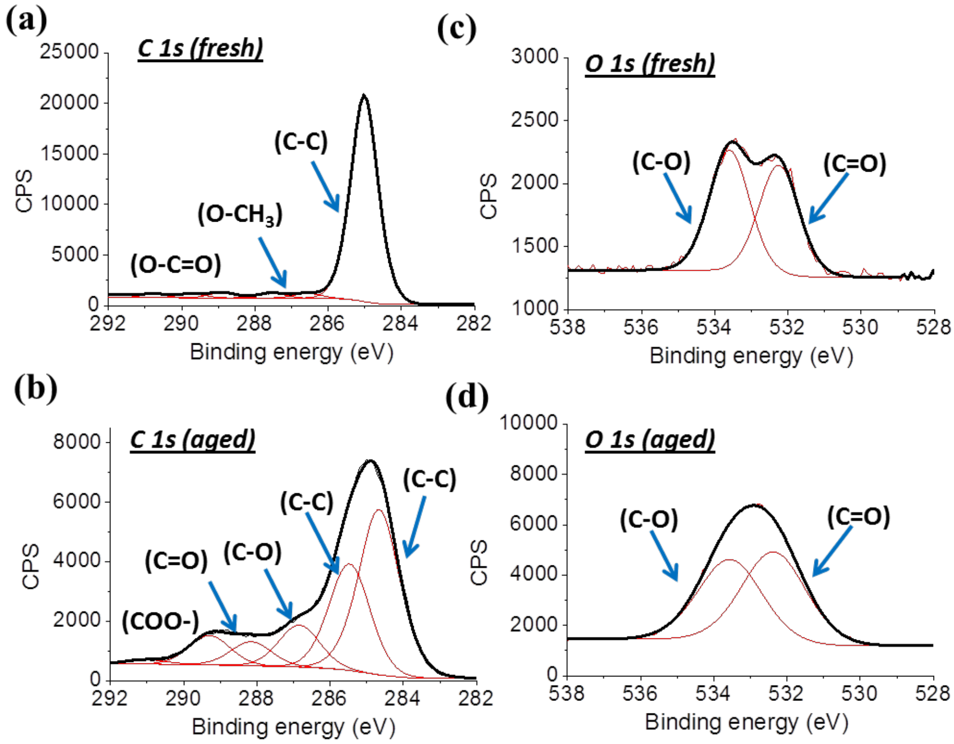

Figure 5.12: Curve fitted peaks for carbon (C 1s) and oxygen (O 1s) before and after light soaking of $PC_{71}BM$. Although sulphur and nitrogen were detected, these were too weak to produce a sufficient signal, and are likely due to surface contamination.

Although trace amounts of both sulphur and nitrogen were detected after light soaking, their levels were too low for curve fitting and are likely due to surface contamination.

5.5.2 PCPDTBT

XPS analyses were also conducted on films of pristine PCPDTBT, and PCPDTBT cast with fullerenes and processing additives. Table 5.9 shows the relative elemental change for pristine PCPDTBT, with Figure 5.13 showing binding energy signals for the measured elements, before and after light soaking for 25, 100 and 300 hours.

Table 5.9: Shown are the relative atom concentrations for fresh and aged PCPDTBT. Overall nitrogen and oxygen increase in concentration, resulting in a proportional decrease in carbon and sulphur.

	Atom % concentration			
Name	**0 hours**	**25 hours**	**100 hours**	**300 hours**
C 1s	86.52	78.04	62.07	60.58
O 1s	0.25	9.75	25.44	26.87
N 1s	4.03	4.49	6.04	6.28
S 2p	9.20	7.71	6.45	6.27

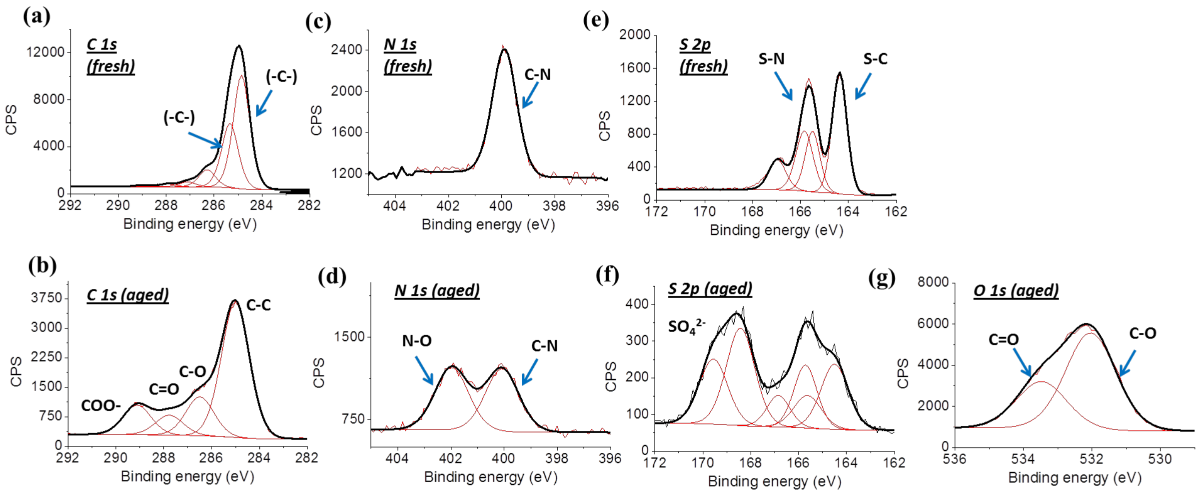

Figure 5.13: Curve fitted peaks for C 1s, N 1s, S 2p and O 1s, before (fresh) and after (aged) light soaking. Oxygen levels were too low for a sufficient signal to be detected before light soaking.

Based on the chemical structure of PCPDTBT, no oxygen (O 1s) should be present at 0 hours. However, a small amount is present, suggesting some oxidation of the powder material or between preparation in the glovebox and transfer to the XPS system. Based on the molecular structure, the composition was expected to be approximately 86% C, 6% N and 8%

S (H is not detected by XPS). While the carbon matches closely, the nitrogen (N) and sulphur (S) content do not. The N:S ratio should be 2:3, but was measured as 3:4 suggesting either excess N or possibly molecular orientation at the surface, such that N is more exposed to the surface, giving a slightly greater signal.

Shown in Table 5.9, the amount of oxygen increases significantly after light soaking, along with an increase in nitrogen, but a decrease in carbon and sulphur is observed. For fresh carbon (C 1s) [Figure 5.13 (a)], curve fitting shows peaks at 284.7 eV and 285.2 eV for unsaturated graphite-like and hydrocarbon-like carbon respectively [230]. This corresponds to carbon in the CPDT and BT monomers, and in the 2-ethyl-hexyl side chains. 286.3 eV is attributed to C-N or C-S bonds. The remaining peaks are related to the aromatic rings, and have been witnessed by others [145, 231].

Following light soaking for 300 hours [Figure 5.13 (b)], curve fitting shows symmetric signals at 285 eV, 286.5 eV, 287.9 eV and 289.2 eV, corresponding to C-C, C-O, C=O and COO- bonds respectively (aged C 1s). The lack of asymmetric peaks indicates a break-up of aromatic rings, which would almost certainly lead to the inability of the polymer for charge transfer. In an OPV cell, this would significantly inhibit the ability to absorb light and enable to transfer charge.

Fresh nitrogen (N 1s) [Figure 5.13 (c)] showed a single peak at 399.9 eV corresponding to the C-N-S in the BT monomer. In aged N 1s [Figure 5.13 (d)], the peak has increased in intensity and split into two peaks at 399.9 eV and 402 eV. The new peak at 402 eV is similar to that found on ageing of the fresh $PC_{61}BM$ and $PC_{71}BM$. This suggests possible absorption of N from the atmosphere, and oxidation of at least some of the original N in the molecule and some of the absorbed N. This is an interesting observation, as the N in the BT unit should be stable. The author may be the first to witness this oxidation for two reasons. Firstly, there are a lack of reports on the long-term chemical changes in D-A polymers using XPS. Secondly, there are few reports on XPS showing the change in the N 1s peak for semiconducting polymers. The latter reason is important, as it is not possible to rule out a change in the electronic state of the polymer chain through a reaction with or adsorption of N_2 gas. This could have happened in the polymer backbone or side chain. However, the likely cause is the oxidation of the N atom in the BT unit. This reasoning is attributed to a C-N peak that only increases by ~50%, while an N-O peak increase dramatically. Ultimately, XPS cannot distinguish between these two possibilities.

Fresh PCPDTBT shows two well-resolved sulphur (S 2p) pairs of peaks (doublets) (Figure 5.13 (e)). The fits shown are constrained, so that the two components of each doublet have the known energy separation and intensity ratio expected from pure S (an energy separation of 1.7 eV and one peak half the intensity of the other). The first doublet, with a peak at approximately 164 eV corresponds to carbon-bonded S, attributed to the S in the aromatic rings of the PCPDTBT molecular structure. The second peak of the doublet with half the intensity, is at approximately 165.8 eV, and corresponds to S in the N-bonded position [230]. Aged S 2p [Figure 5.13 (f)] shows a more complex structure. The original first two doublets are still present, but the relative intensity of the first doublet (at approximately 164 eV) is lower such that these two doublets are now approximately the same in relative intensity. A third doublet is now present at approximately 168.4 eV. This third component corresponds to S in a fully oxidised sulphate environment, typically SO_4^{2-}. This is consistent with the view of Krebs [156], that it is likely for the aromatic structure to be broken with longer exposure times, forming R-SO_x.

The negligible level of oxygen in PCPDTBT at 0 hours, meant it was not possible for any curve fitting, however, aged O 1s shows two peaks after light soaking for 300 hours [Figure 5.13 (g)]. The peaks at 532 eV and 533 eV correspond to C=O and C-O bonds respectively, with C=O at a higher proportion. Carbonyl groups have been shown to be charge traps in OFET devices [146], and likely to do the same in OPV cells.

Based on the findings of the XPS analysis, Figure 5.14 summarises the changes in the chemical structure of PCPDTBT after light soaking, showing the three primary changes including the ring structure decomposing into R-SO_x.

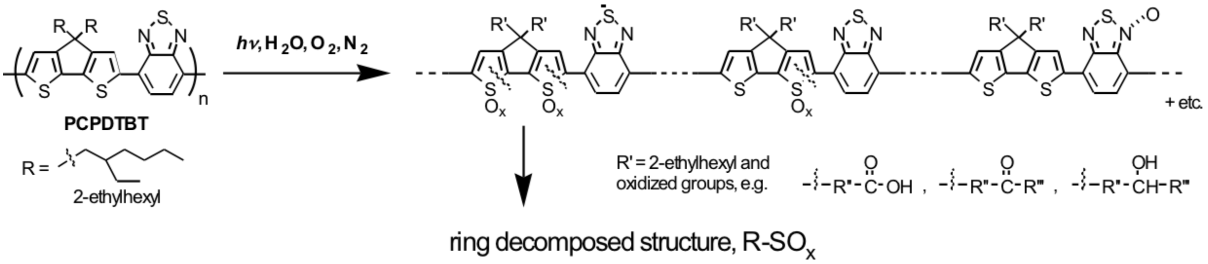

Figure 5.14: Plausible change of chemical structure of PCPDTBT after light soaking in normal atmospheric conditions, based on XPS data. The thiophene ring structure decomposes into R-SOx

5.5.3 PCPDTBT·PCBM

Films of PCPDTBT blended with $PC_{61}BM$ or $PC_{71}BM$ respectively were also investigated with XPS, to understand the changes occurring in the active layer during light soaking. Data for these tests is shown in Table 5.10.

Table 5.10: Shown are the relative atom concentrations for fresh and aged PCPDTBT with $PC_{61}BM$ or $PC_{71}BM$. Overall nitrogen and oxygen increase in concentration, resulting in a proportional decrease in carbon and sulphur. $PC_{71}BM$ appears to be more stable to oxidation than $PC_{61}BM$.

	Atom % concentration			
	PCPDTBT·$PC_{61}BM$		**PCPDTBT·$PC_{71}BM$**	
Name	**0 hours**	**300 hours**	**0 hours**	**300 hours**
C 1s	93.25	67.89	93.79	74.21
O 1s	1.98	27.91	1.66	21.06
N 1s	1.44	2.61	1.35	2.69
S 2p	3.34	1.59	3.20	2.04
C:S	27.92	42.70	29.31	36.38
Relative % of PCPDTBT	36.33	24.36	34.78	32.54

Data shown in Table 5.10 shows a similar trend to that seen in pristine PCPDTBT, where O 1s increases considerably together with a small increase in N 1s and a decrease in S 2p. These changes are slightly reduced for $PC_{71}BM$, indicating that this fullerene derivative has a *protective* effect on the polymer, compared to $PC_{61}BM$.

As all blends possess 75% fullerene content, it would be expected that the molecular structures of PCPDTBT·$PC_{61}BM$ to possess 95.7% C, 2.3% O, 1.2% S and 0.8% N, and the PCPDTBT·$PC_{71}BM$ to possess 96.1% C, 2.1% O, 1.0% S and 0.8% N. However, both layers exhibit higher S and N content, which could be explained by surface contamination and oxidation during transport.

By comparing the carbon to sulphur ratio (C:S), it is possible to gain insight into the vertical gradient in the active layer. In pristine PCPDTBT:PCBM active layers, carbon is present in both materials, with sulphur only present in PCPDTBT. A decrease in relative PCPDTBT concentration for light soaked samples, infers PCBM aggregation at the surface [232].

5.5.4 PCPDTBT·PCBM with processing additives

XPS was also used to investigate films of PCPDTBT·$PC_{71}BM$ with and without processing additives. Table 5.11 shows data for PCPDTBT·$PC_{71}BM$ with ClN or ODT.

Upon light soaking of PCPDTBT·$PC_{71}BM$ films with ClN or ODT, the same trend is seen for previous samples. Higher O is observed, along with higher N, lower S and lower C. The level of oxygen is slightly increased after light soaking when a processing additive is used, however the magnitude of this effect does not correlate to the loss of performance observed in working OPV cells. It can, therefore, be concluded that processing additives impair the performance of OPV cells via physical rather than chemical changes.

Table 5.11: Shown is the relative atom concentrations fresh and aged PCPDTBT·$PC_{71}BM$ with 1-chloronaphthalene (ClN) or ODT. Overall nitrogen and oxygen increase in concentration, resulting in a proportional decrease in carbon and sulphur. As expected, films made with ODT show increased sulphur content.

	Atom % concentration			
	PCPDTBT·$PC_{71}BM$ with ClN		**PCPDTBT·$PC_{71}BM$ with ODT**	
Name	**0 hours**	**300 hours**	**0 hours**	**300 hours**
C 1s	91.50	71.88	90.84	69.48
O 1s	1.61	22.58	1.26	23.48
N 1s	2.41	2.90	2.56	3.73
S 2p	4.49	2.64	5.34	3.31
C:S	20.38	27.23	17.01	20.99
Relative % of PCPDTBT	48.0	42.1	58.0	52.8

The vertical concentration gradient was measured by calculating the polymer·fullerene composition at the top surface of PCPDTBT·$PC_{71}BM$ active layers. Table 5.11 shows the peak area ratios of the S 2p and C 1s peaks for the top surfaces. Even though $PC_{71}BM$ contains oxygen, the O 1s intensity cannot unambiguously be assigned to $PC_{71}BM$ due to the air contamination of the sample. Additionally, the volume fraction of PCPDTBT at the top layer of the blend films compared to a pure PCPDTBT top layer is shown in Table 5.11. Previous studies of polymer-fullerene blends have used these two ratios to correlate the relative polymer concentration at the top surface of the blend [232, 233].

From Table 5.11, it is found that the relative % of PCPDTBT at 0 hours is higher than if the film was homogeneously distributed; one should expect 25% relative PCPDTBT if this was the case. However, the measured concentration of PCPDTBT is 58% for films with ODT (48% for ClN) and 35% for films without ODT. This indicates that all layers exhibit an enrichment of PCPDTBT at the surface; however, a much higher enrichment occurs at the surface of blends with ODT/ClN. Therefore, by using this surface for deposition of the anode electrode, one would expect to improve the charge transfer to the electrodes. It also indicates that cells made with ODT/ClN are even better suited for inverted cells than made without ODT/ClN.

After ageing, the layers with ODT show a composition change (around 10% relative decrease in PCPDTBT content – 12% for ClN) at the top surface. However, layers without ODT/ClN show almost no change. While PCPDTBT·$PC_{71}BM$ with ODT provides improved initial conditions for inverted cells, the inclusion of the additive leads to greater changes in the layer and thus, more significant change in the morphology. Previous reports indicate that ODT remains in the film after processing, due to its high boiling point (270°C), and continues to alter the morphology dynamically with time [234]. These XPS data support this view.

5.6 Summary

The stability of the PCPDTBT material was tested using a combination of OPV device data and analytical instruments. From device data, it was shown that the material is less stable than more commonly reported P3HT polymer. It appears that the inclusion of ODT into the active layer of PCPDTBT-based OPV devices, led to a reduced stability. This was witnessed for encapsulated and non-encapsulated devices and for both inverted and non-inverted architectures. EQE measurements determined the spectral response as a function of time. By tracking the peak absorption wavelengths of PCPDTBT and $PC_{71}BM$ (793 nm and 483 nm respectively), $PC_{71}BM$ was found to be the lesser stable component of the active layer. ODT was found to increase the photocurrent across the visible range, while decreasing the intrinsic stability of PCPDTBT·$PC_{71}BM$ based cells. The physical changes were examined using AFM and GISAXS/GIWAXS, and infer that the inclusion of processing additives lead to greater morphological instability during ageing experiments. When considering the power generated over the lifetime, cells made without ODT give a greater output, despite the reduced initial performance.

In an attempt to overcome the negative effects of ODT, naphthalene-based processing additives were trialled. The PCE of PCPDTBT·$PC_{71}BM$ devices containing ClN, BrN or ODT were measured at 2.30%, 1.72% and 2.95%, respectively. When looking at the metric of total extractable power, the first 1000 hour, devices made with ClN performed best, despite the lower initial performance.

In an attempt to increase the stability of OPV cells, inverted cells of PCPDTBT·$PC_{71}BM$ with and without ODT were fabricated using ZnO and a composite MoO_3/Ag anode. Inverted cells of PCPDTBT·$PC_{71}BM$ with and without ODT demonstrated increased intrinsic stability compared to non-inverted cells, due to improved stability of the J_{SC} and FF with time.

XPS analysis was conducted on fresh and aged films of PCBM and PCPDTBT and blends of these materials, with and without processing additives. After ageing, XPS studies show that PCPDTBT appears as an oxygen-containing polymer, with data indicating that a break-up in the aromatic rings, formation of sulphates at the thiophene ring, chain scission in the polymer backbone and also loss of side chains. For films of fullerene derivatives, oxidation of carbon atoms in the fullerene cage and side chains is observed, including a breaking of the cage structure, after ageing. Films of PCPDTBT·$PC_{61}BM$ and PCPDTBT·$PC_{71}BM$ were also studied. The uptake of oxygen following light soaking was reduced when $PC_{71}BM$ was used instead of $PC_{61}BM$, inferring $PC_{71}BM$ to be more stable. Films of PCPDTBT·$PC_{71}BM$ with ClN and ODT respectively were also studied, however, similar degradation was observed to films without processing additives. The level of oxidation in PCPDTBT·$PC_{71}BM$ films with and without processing additives does not correlate with the reduction in performance seen in OPV cells. This suggests that OPV cell degradation is determined mostly by physical rather than chemical changes. However, XPS data did show that ODT inclusion leads to greater morphological changes, supportive of the device, AFM and GISAXS/GIWAXS data.. It should also be noted that the level of oxidation for samples studied using XPS, is likely to be much higher than in OPV cells. The same degradation processes would be expected in OPV cells, however on a longer timescale, due to the protective effect of the electrodes.

Chapter 6 Optical and electrical characterisation of cross-linkable PCPDTBT

6.1 Introduction

In order to improve the stability of CPDT-based polymers and oligomers, it is possible to develop active materials that cross-link through either photo- or thermal-initiation. Published works support this approach for both donor and acceptor materials in the active layer [137, 138].

In this chapter, cross-linkable PCPDTBT was used to make OPV cells with high PCE and improved stability. The 2-ethylhexyl groups were substituted with 5-hexenyl groups on the 4, 4-position of CPDT; the cross-linking nature originated from the vinyl group of 5-hexenyl [235, 236].

Four variants of thermally cross-linkable PCPDTBT were studied. These differed by their side chains, which are as follows:

- 5% hexenyl and 95% 2-ethylhexyl (**C1**);
- 50% hexenyl and 50% 2-ethylhexyl (**C2**);
- 5% hexenyl capped with a random mixture of hydrogen, anisole and phenyl groups, and 95% 2-ethylhexyl (**C3**);
- 50% hexenyl capped with a random mixture of hydrogen, anisole and phenyl groups, and 50% 2-ethylhexyl (**C4**).

From here onwards, these will be referred to as **C1**, **C2**, **C3** and **C4**. PCPDTBT with 2-ethylhexyl side chains only, was included as a control.

6.2 Synthesis

Initially, PCPDTBT polymers with 5% (**C1**) and 50% (**C2**) cross-linkable 5-hexenyl side chains, were synthesised using Pd catalysed Suzuki coupling. **C2** was synthesised with a higher concentration of cross-linkable side chains, for chemical structure clarification before and after cross-linking. Chemical changes in **C1** were only observable with ^{1}H NMR, owing to relatively few vinyl groups. Although an increase in cross-linkable side chains is desired, this proportionately reduces the solubilising 2-ethylhexyl side chains needed for efficient solution processing and film fabrication.

Subsequent addition of excess bromobenzene or bromoanisole after initial polymerisation, led to 5-hexenyl side chains capped with phenyl or anisole groups, via Heck coupling. This addition reduced the cross-linking temperatures of **C1** and **C2** from approximately 260°C to 170°C. These variants are **C3** and **C4** respectively. Figure 6.1 shows the synthetic schemes for **C1** and **C2** (top), and **C3** and **C4** (bottom).

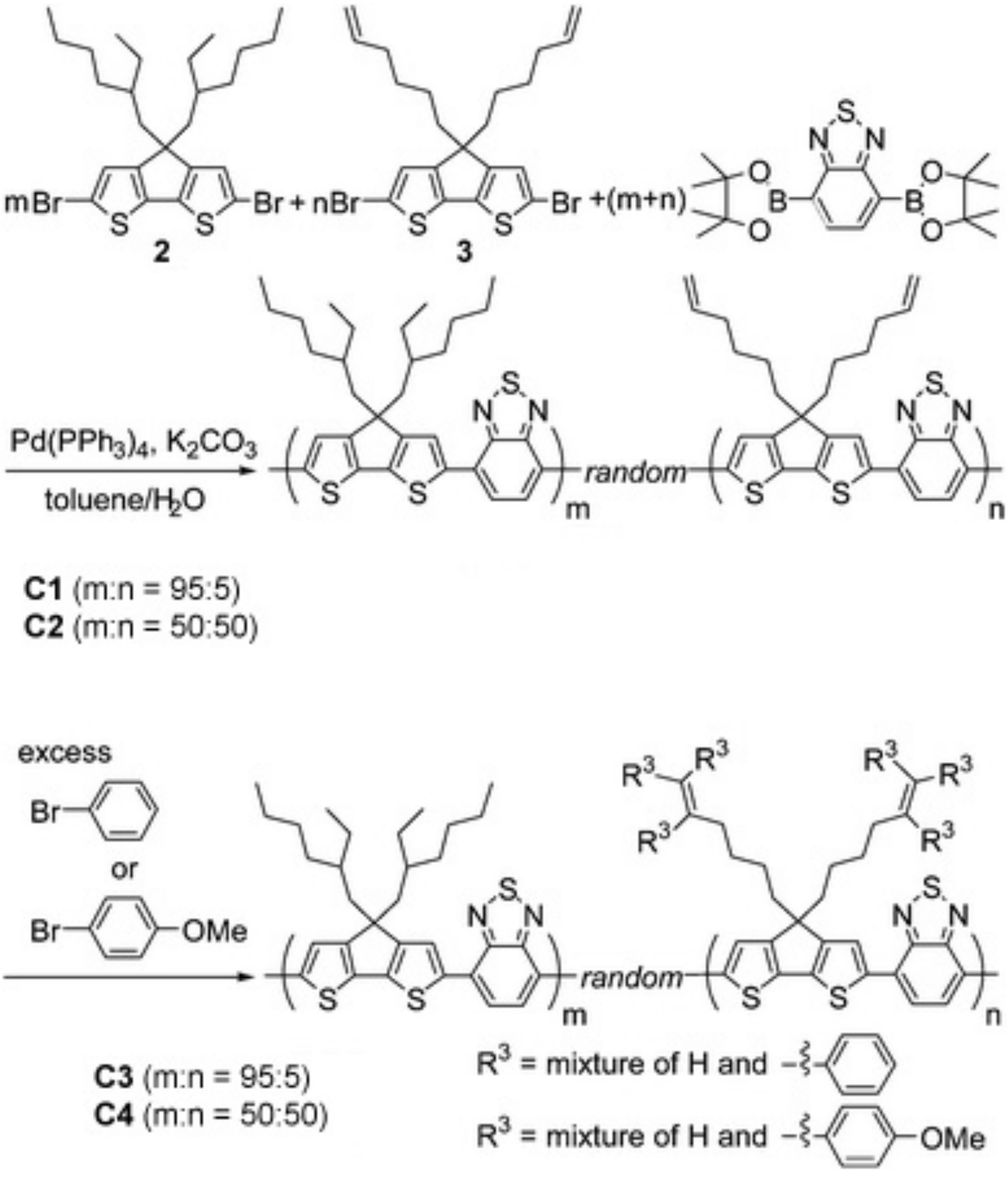

Figure 6.1: BT bonded to CPDT with either 2-ethylhexyl or 5-hexenyl side chains, forming a larger CPDT-BT monomer (top). **C1** and **C2** (middle) contain 5% and 50% cross-linkable 5-hexenyl side chains. The 5-hexenyl side chains of **C1** and **C2** treated with either bromobenzene or bromoanisole, become phenyl- or anisole-capped, with reduced cross-linking temperatures. These are **C3** and **C4** respectively (bottom).

6.3 FTIR and optical properties to confirm cross-linking action

Three different analytical techniques were used to characterise the cross-linking properties of CPDT-BT based polymers. Firstly, Fourier-transform Infrared (FTIR) spectroscopy was undertaken to investigate the presence of particular chemical bonds, and evaluate if cross-linking occurred in polymers **C1** to **C4** after annealing.

Films of **C1** to **C4** were prepared on KBr slides. Two samples of each film were prepared and annealed below and above their respective cross-linking temperatures for one hour. Figure 6.2 shows FTIR spectra of **C2**, showing absorption peaks at 993 cm^{-1} and 910 cm^{-1}, corresponding to out of plane bending of the vinyl group (–C=C–H) [235]. **C2** is presented independently as it shows the strongest spectroscopic signal. After annealing at 260°C, both peaks were reduced by 32%, demonstrating a cross-linking reaction between adjacent vinyl side chains, resulting in C=C bond loss.

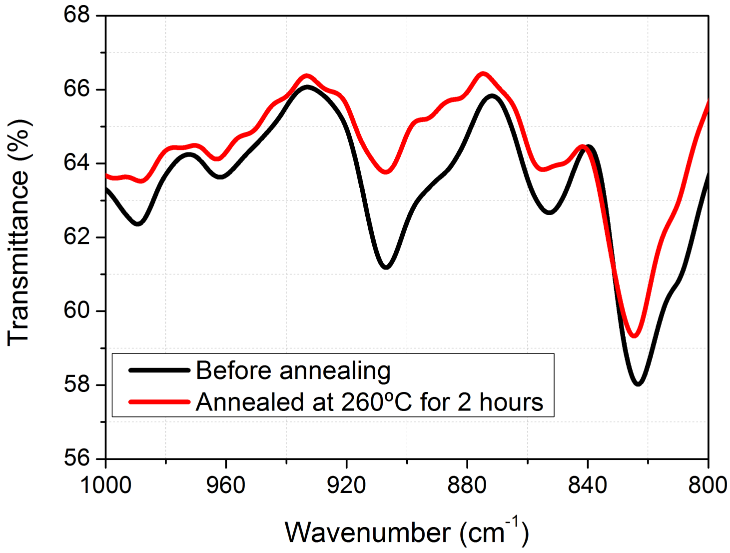

Figure 6.2: FTIR spectra of **C2** on a KBr substrate before and after annealing at 260°C. Peaks at 993 cm^{-1} and 910 cm^{-1} are reduced following cross-linking, owing to the loss of C=C bonds.

Only small changes in FTIR spectra before and after annealing were observed in **C1** and **C3** because of a lower concentration of cross-linkable side groups. **C4**, containing a significant content of cross-linking units, showed evidence of cross-linking in agreement with the results for **C2**.

A second strategy to evaluate whether cross-linking occurred was to check the polymers' solubility. **C1** to **C4** were dissolved in chlorobenzene and heated until the polymer became insoluble. **C3** became insoluble at 170°C, inferring a cross-linking reaction. However, **C1**, **C2** and **C4** only became insoluble at the higher temperature of 260°C for one hour, which is a temperature unsuited for OPV cell fabrication. Shown in Figure 6.3 is **C3** (a) and **C4** (b)**,** before and after cross-linking, where the polymer was highly soluble in chlorobenzene before (left-hand vial) and insoluble after annealing (right-hand vial). **C3** became the primary focus of further work, due to its lower cross-linking temperature. The reason for the reduced cross-linking temperature is the styryl structure given by the Heck reaction [Figure 6.1 (bottom)]. Styryl groups are more reactive than allyl groups, lowering the cross-linking temperature [113]. The anisole group on **C4** is bulkier than on **C3**, which may be the reason for its higher cross-linking temperature.

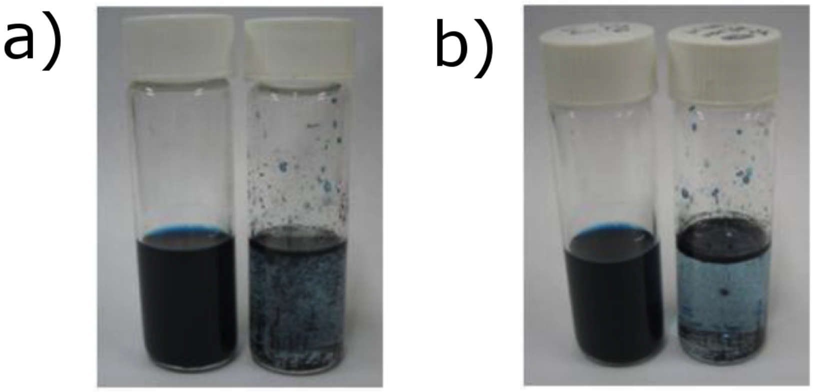

Figure 6.3: **C3** and **C4** are soluble in chlorobenzene before cross-linking (left vials) and become insoluble at their respective cross-linking temperatures of 170ºC and 260ºC (right vials).

As a final test, **C3** and **C4** were spin-cast onto glass substrates to form polymer films and annealed at their cross-linking temperatures (170°C for **C3** and 260°C for **C4**). A control sample of the non-cross-linkable analogue used in Chapter 5 (termed PCPDTBT) was also spin cast onto a glass substrate. These polymers were selected as **C3** is a polymer suited for OPV fabrication, and **C4** has a close chemical structure to **C3**, but a higher cross-linking active site concentration. Chloroform (1 mL) was deposited on the polymer film and allowed to stand for 30 seconds, before being spun dry at 1000 RPM for 30 seconds. PCPDTBT has approximately the same solubility in chloroform as in chlorobenzene, and was expected to be dissolved upon flooding. Thin film absorption measurements were taken before and after chloroform rinsing, shown in Figure 6.4. The absorption spectrum for non-cross-linkable PCPDTBT is not shown, as it immediately dissolved in chloroform, leaving little trace of the original film.

The absorption properties for thin films of **C3** and **C4** do change, with a relative decrease in intensity, however, a large quantity of the polymers remain on the glass substrate. **C3** remains partially-soluble after cross-linking due to fewer 5-hexenyl groups; hence it experiences the large change in absorption properties during chloroform rinsing. Conversely, **C4** is only slightly affected by the solvent rinsing tests due to the higher content of 5-hexenyl groups, providing further evidence of it cross-linking nature.

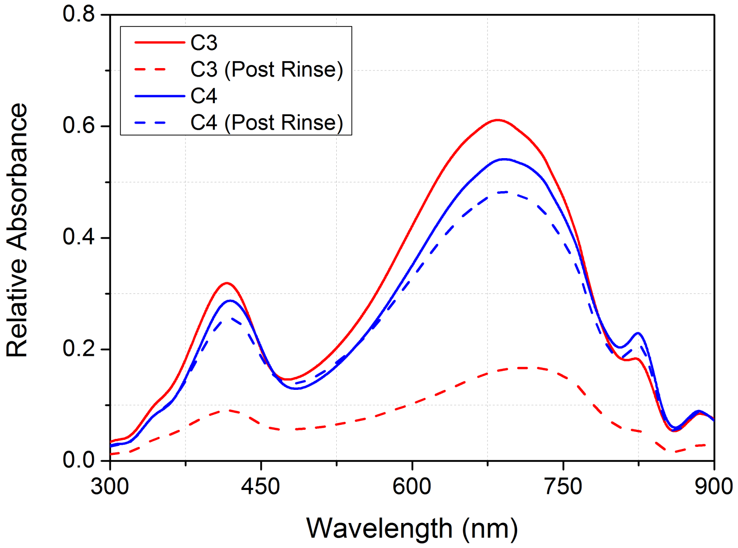

Figure 6.4: Absorption spectra of **C3** and **C4** before and after rinsing with chloroform. **C4** demonstrates greater chemical stability due to the higher concentration of cross-linked 5-hexenyl side chains.

6.4 Optical characterisation of cross-linkable PCPDTBT

PCPDTBT and **C3** were spin-cast on glass substrates to form 100 nm films and then UV-visible spectra compared after annealing at 80ºC and 170ºC. These temperatures are below and above the cross-linking temperature of **C3**, and more suitable for OPV cell fabrication. Figure 6.5 shows that PCPDTBT has increased absorption compared to **C3** at both 80ºC and 170ºC. The 5-hexenyl groups of **C3** prevent closer packing of the polymer chains, reducing π-π* overlapping and thus limiting the optical absorption. However, it is unlikely that the polymer density has changed by a factor of three. It is possible that a large change in absorption originates from changes in polymer molecular orientation.

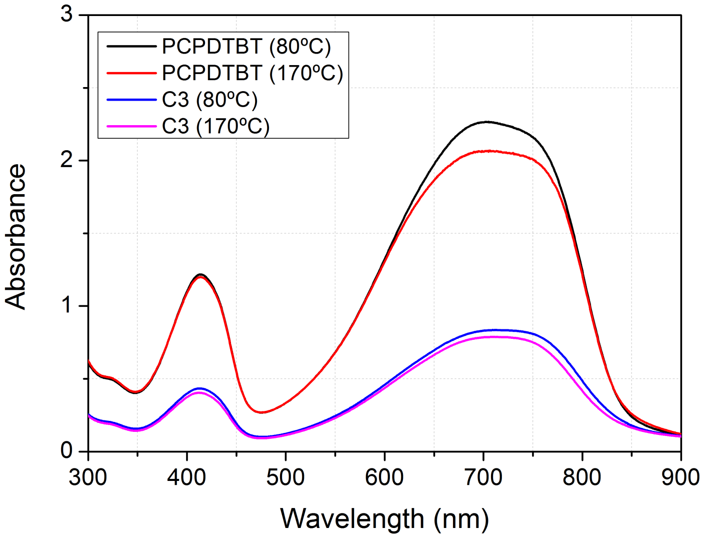

Figure 6.5: Absorption spectra for PCPDTBT and **C3**, annealed at 80ºC and 170ºC. The relative change in absorption is greater for PCPDTBT compared to **C3**, due to the bulky side chains of **C3** preventing oxygen and water from reaching the polymer backbone.

PCPDTBT's relative change in absorption after annealing at 170ºC is greater than for **C3**, and is attributed to thermo-oxidation [151]. The increased heat accelerates the reaction between the polymer backbone and any oxygen or water present, leading to conjugation loss.

It is likely that the longer and bulky side chains of **C3** restrict oxygen and water from reaching the polymer backbone, making it inherently more stable.

Absorption spectra of 100 nm films of PCPDTBT·$PC_{71}BM$ with ODT and **C3**·$PC_{71}BM$ with ODT were compared and are shown in Figure 6.6. These films were annealed at their optimum temperatures of 80°C and 170°C respectively.

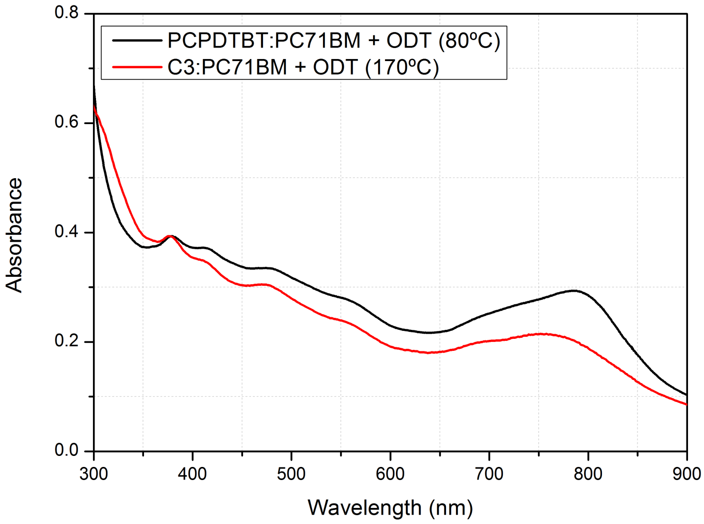

Figure 6.6: Absorption spectra of 120 nm films of PCPDTBT and **C3** each blended with $PC_{71}BM$ and ODT.

C3·$PC_{71}BM$ again shows reduced absorption compared to PCPDTBT, originating from the longer side chains in **C3**. The absorption spectrum of **C3** indicates that the π–π* transition is only weakly affected by the presence and positioning of the side chains (the high-energy peak does not shift), but the low energy absorption peak does see a significant change in relative intensity. This is assumed to be a result of reduced intrachain charge-transfer (CT) from CPDT to BT groups.

Due to the high cross-linking temperatures of **C1**, **C2** and **C4**, further cell characterisation focused on **C3** only.

6.5 Charge transport properties

C3 was characterised using SCLC devices to probe the charge transport properties. SCLC devices were made, characterised and the subsequent I-V curves modelled using the Mott–Gurney law. SCLC devices were biased from -2 to + 10 V under dark conditions, and the resulting current measured. Figure 6.7 shows a plot of the logarithm (base 10) of measured current against the logarithm (base 10) of the effective voltage. It was possible to apply linear fits showing the Ohmic (red) and SCLC (blue) regions, as described in section 3.3.8. Figure 6.7 demonstrates that current is space-charge limited, facilitating the use of the Mott-Gurney law. The hole mobility term was deduced from a Mott-Gurney fit overlapping the measured data points, as shown in Figure 6.7.

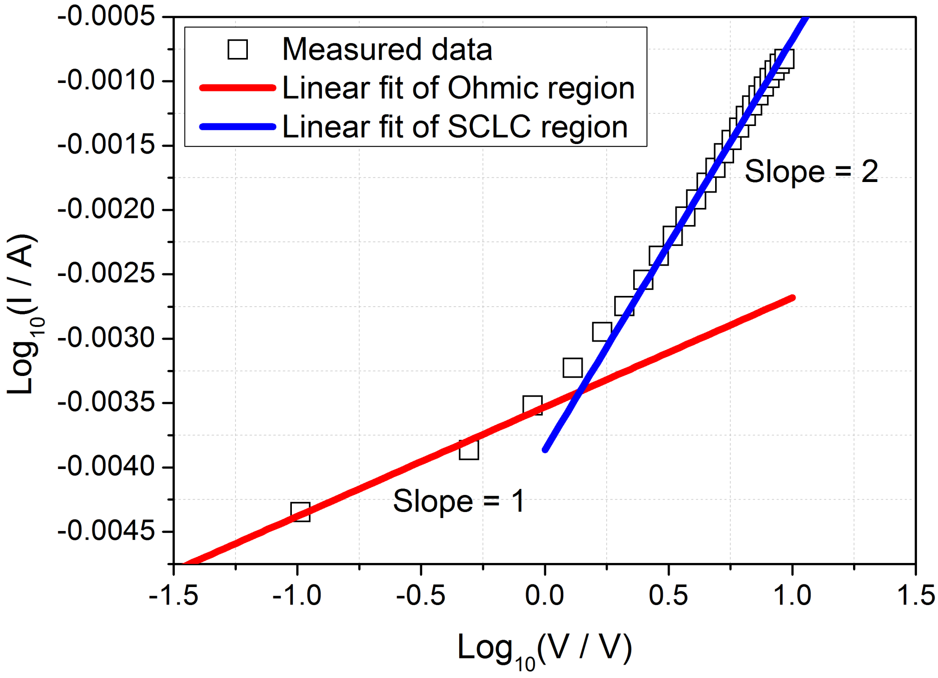

Figure 6.7: The current flow in SCLC devices is space-charge limited, as demonstrated by the gradient of the linear fit for the SCLC region being twice that of the gradient for the fit of the Ohmic region. For **C3** annealed at 170°C, the maximum hole mobility was found to be 2×10^{-4} $cm^2.V^{-1}.s^{-1}$. Hole mobilities were also calculated for SCLC devices annealed at other temperatures (not shown).

Figure 6.8 shows the hole mobility with respect to annealing temperature, with the results summarised in Table 6.1. PCPDTBT demonstrated a maximum mobility of 2 x 10^{-4} $cm^2.V^{-1}.s^{-1}$, but that decreased to 6 x 10^{-5} $cm^2.V^{-1}.s^{-1}$ after annealing at temperatures greater than 120°C. This is consistent with previous experiments, showing that hole mobility declines at higher temperatures [118].

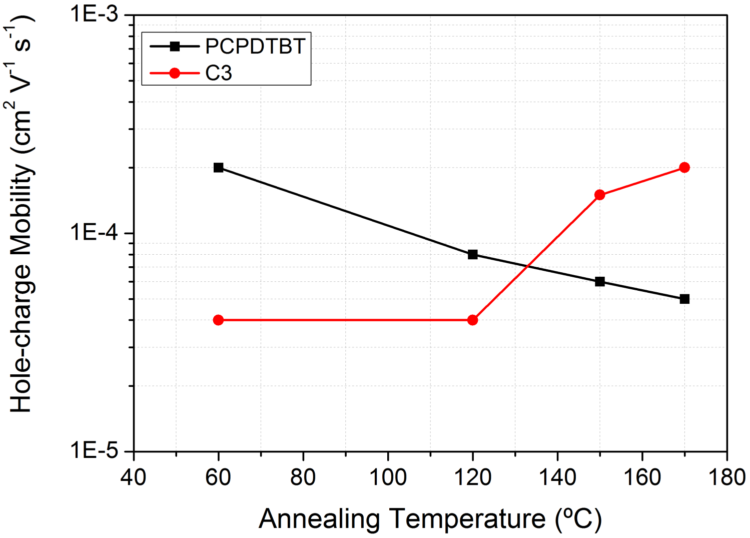

Figure 6.8: The dependence of PCPDTBT and **C3** effective hole mobilities on annealing temperature, obtained from SCLC devices using the Mott-Gurney law.

Table 6.1: Effective hole mobility values, calculated using SCLC devices with a 100 nm thick film.

	Hole mobility ($cm^2.V^{-1}.s^{-1}$)	
Annealing temperature (°C)	**PCPDTBT**	**C3**
60	2.0 x 10^{-4}	4.0 x 10^{-5}
120	8.0 x 10^{-5}	4.0 x 10^{-5}
150	6.0 x 10^{-5}	1.5 x 10^{-4}
170	5.0 x 10^{-5}	2.0 x 10^{-4}

The maximum hole mobility of **C3** for low temperature annealing was 4.0 x 10^{-5} cm^{2}.V^{-1}.s^{-1}; however this significantly improved to 2.0 x 10^{-4} cm^{2}.V^{-1}.s^{-1} after annealing at the cross-linking temperature of 170°C or greater. **C3**'s allyl group reduces the mobility prior to cross-linking, presumably reducing the intermolecular packing between adjacent polymer chains and making charge transport less favourable. Cross-linking reduces this packing dimension; improving charge transport, thus hole mobility. This view is supported by WAXS and GISAXS data.

6.6 OPV characteristics

Six-pixel OPV cells were made from **C3**·PC$_{71}$BM and **C3**·PC$_{71}$BM using previously optimised processing conditions. Figure 6.9 shows the best performing I-V characteristics for **C3**·PC$_{61}$BM and **C3**·PC$_{71}$BM with ODT, with data summarised in Table 6.2. Also included in Table 6.2 are data for the non-cross-linked PCPDTBT, fabricated and tested under the same conditions.

The optimum polymer-fullerene blend ratio for both **C3**·PC$_{61}$BM and **C3**·PC$_{71}$BM with ODT was the same as in Chapter 4 and Chapter 5. However, differences were discovered for optimal film thickness and annealing temperatures. The best performing **C3**·PC$_{61}$BM cell gave a similar PCE to the corresponding PCPDTBT cell, despite a J$_{SC}$ reduction of 6%. The higher PCE is primarily due to the 6% increase in V$_{OC}$ and a minor increase in Fill Factor (FF). The reduced J$_{SC}$ correlates well with the absorption experiments from section 6.3 (see Figure 6.6), indicating that **C3** has a much-reduced absorption spectrum compared to PCPDTBT of equal thickness.

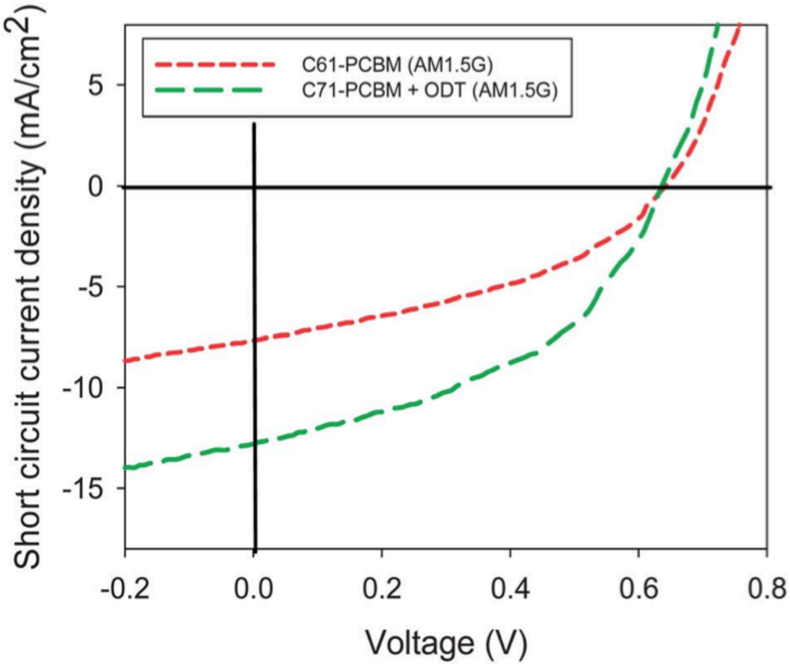

Figure 6.9: OPV cell I-V characterisation under AM1.5G illumination (100 mW.cm^{-2}) for the best performing cells of **C3**·$PC_{61}BM$ and **C3**·$PC_{71}BM$ with ODT. $PC_{71}BM$ shows increased J_{SC}, through increased photon absorption.

The measured J_{SC} is remarkably high given the substantially lower absorption of **C3**, when compared to PCPDTBT. Cells fabricated from **C3**·$PC_{71}BM$ with ODT showed a minor decrease in PCE (6% reduction). OPV cells fabricated with the cross-linked polymer also exhibited slightly lower J_{SC}. However, this drop in performance as a result of reduced J_{SC} was partially offset by the increase in FF and V_{OC}. For cells fabricated with and without ODT, the increase in V_{OC} with cross-linkable polymers is an interesting observation.

Table 6.2: OPV cell performances of PCPDTBT and **C3** blended with $PC_{61}BM$ or $PC_{71}BM$ with ODT respectively.

	Annealing Temperature (°C)	V_{OC} (V)	J_{SC} (mA.cm^{-2})	FF (%)	PCE (%)
PCPDTBT·$PC_{61}BM$	80	0.61	-7.10	42.6	1.85
PCPDTBT·$PC_{71}BM$ + ODT	80	0.61	-13.8	44.2	3.88
C3·$PC_{61}BM$	170	0.65	-6.71	43.0	1.84
C3·$PC_{71}BM$ + ODT	170	0.64	-12.8	44.8	3.65

The higher V_{OC} of the cross-linked cells (50 mV increase) can be expected when considering the lower HOMO level of **C3** (HOMO [C3] = 4.93 eV, HOMO [PCPDTBT] = 5.00 eV, from cyclic voltammograms of polymer films). For OPV cells using PCPDTBT, it was observed that annealing the active layer worsened OPV performance, consistent with other work [118], predominantly as a result of decreases in FF and J_{SC}. The likely reason for this deterioration relates to a worse morphology for efficient charge separation and transfer, and that a slow drying process improves the morphology during phase separation. This is different to the trend observed with OPV cells fabricated with **C3**, where consistent cell performance is observed for annealing temperatures up to 170°C. The minor improvement in FF is likely to be a result of the increased hole mobility of **C3** after annealing. The increase in hole mobility enables the series resistance, R_S to decrease, which contributes to improved charge transport properties.

6.6.1 Lifetime analysis

The lifetime of cross-linkable PCPDTBT was investigated due to its increased stability over non-cross-linkable analogues. Cells using PCPDTBT·$PC_{61}BM$ and **C3**·$PC_{61}BM$ as reported in Table 6.2 were lifetime tested. Data is shown in Figure 6.10.

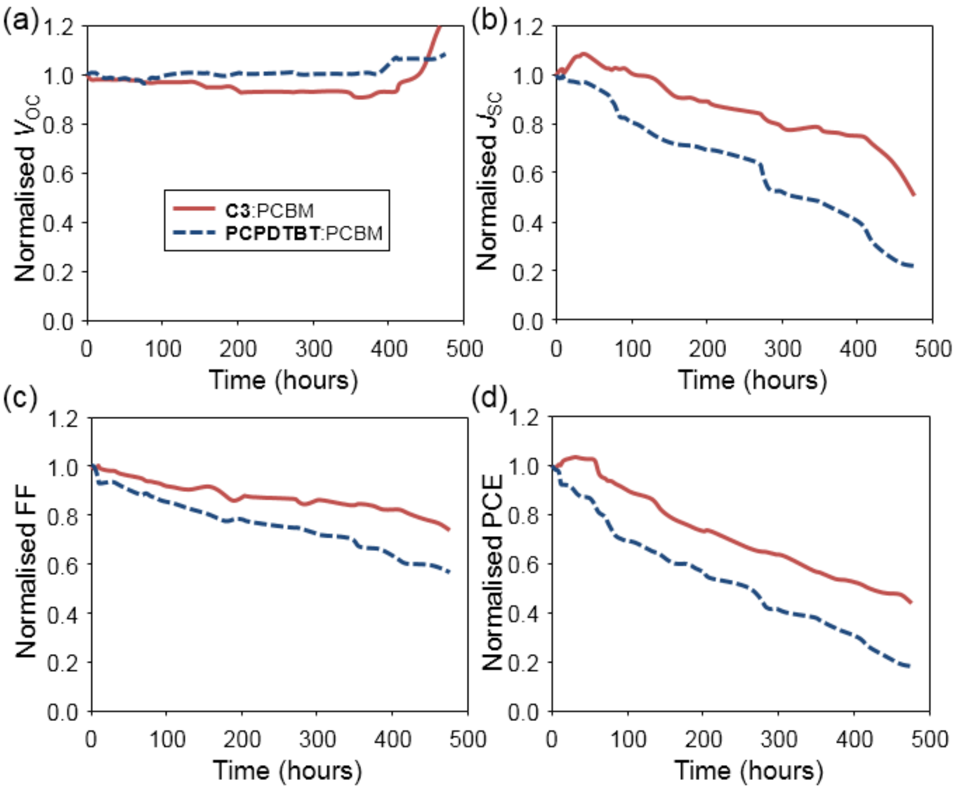

Figure 6.10: Light soaking tests of PCPDTBT·$PC_{61}BM$ and cross-linked **C3**·$PC_{61}BM$ respectively. The PCE of **C3** is stable due to more stable J_{SC} and FF.

The V_{OC} is shown to be relatively stable for both cells. The slower change in PCE with time for cross-linked **C3**·$PC_{61}BM$ is a result of more stable J_{SC} and FF. As demonstrated in previous chapters, the active layer morphology changes with age, leading to decreased PCE. The cross-linking behaviour of **C3** appears to reduce changes in morphology, inhibiting the aggregation of PCBM, thus increasing FF and J_{SC} stabilities with time.

6.7 Morphological studies using AFM

Both SCLC device and OPV cell data, and absorption spectra indicate improved thermal stability for cross-linked **C3**. In order to understand the changes in hole mobility during cross-linking, AFM images of the polymer film at different annealing temperatures were taken, and are shown in Figure 6.11. AFM showed that annealing **C3** did not have a drastic effect on the surface roughness of R_A = 0.563 nm, R_Z = 5.99 nm at 60°C, to R_A = 0.606 nm, R_Z = 6.89 nm at 170°C. This is compared to PCPDTBT (micrographs not shown), where a substantial increase in surface roughness is observed from R_A = 1.17 nm, R_Z = 10.5 nm at 60ºC to R_A = 1.99 nm, R_Z = 17.31 nm at 170ºC. The increased surface roughness indicates substantial changes to the polymer morphology of the non-cross-linkable PCPDTBT after annealing, presumably indicating less thermal stability. AFM data are also shown for cells of **C3**·$PC_{61}BM$ with a 1:3 ratio in Figure 6.11. After cross-linking at 170°C, PCBM aggregation is not observed.

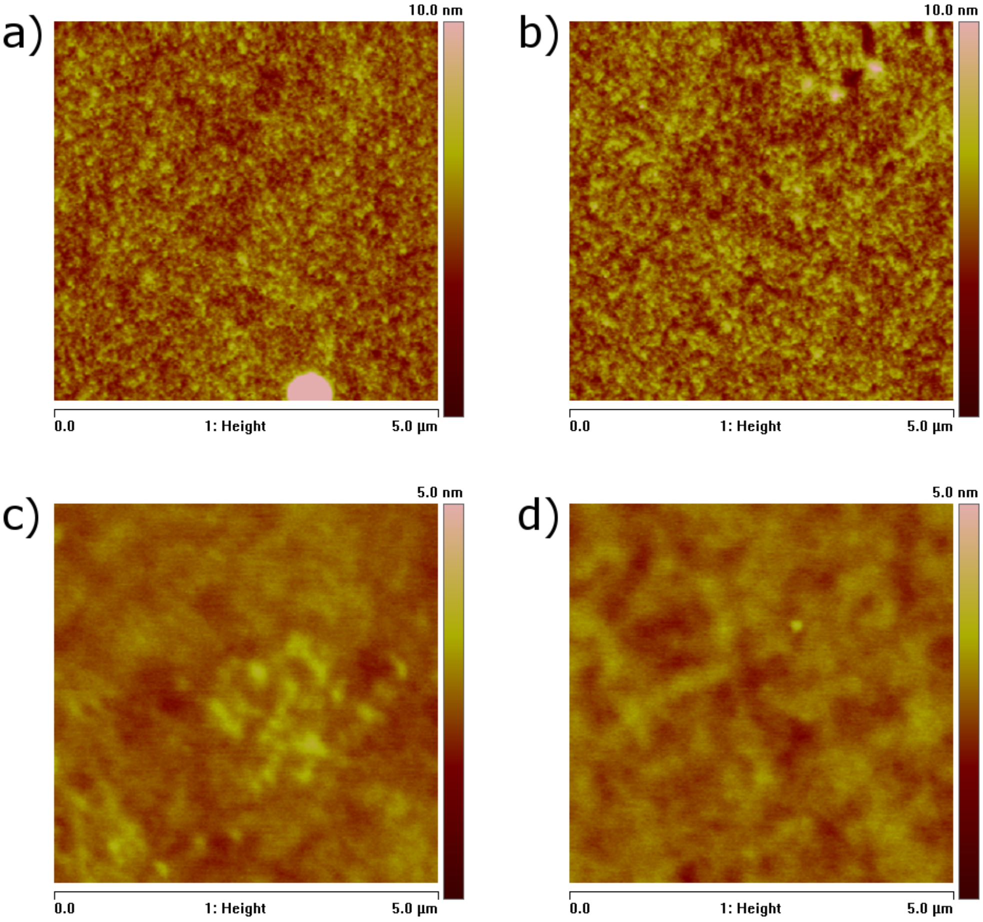

Figure 6.11: AFM topography of the film surface of **C3** (a) before and (b) after annealing at 170°C and blended with $PC_{61}BM$ (c) before and (d) after annealing at 170°C.

6.8 Morphological studies using WAXS/GISAXS/GIWAXS

WAXS measurements for **C3** were used to understand the nature of molecular stacking in cross-linkable PCPDTBT with PCBM, and are shown in Figure 6.12. WAXS data for **C3** shows a slightly different molecular structure when compared to PCPDTBT reported elsewhere.

Prior to cross-linking, the lamella packing of **C3** showed a broad feature with a peak at 2θ = 5.12° (d-spacing = 8.63 Å), corresponding to the branched side chains from the polymer. Despite the side chains of **C3** being longer, the spacing between polymer chains is less than for PCPDTBT (2θ = 4.77°, d-spacing = 9.27 Å). This spacing appears to increase after cross-linking. A second broad peak is also observed at 2θ = 11.7° (3.80 Å), increasing after cross-linking. However, for both dimensions, a much stronger peak is observed in the WAXS curve after cross-linking, suggesting that the cross-linking action increases the order in the polymer film and hence the increased hole mobility in **C3**.

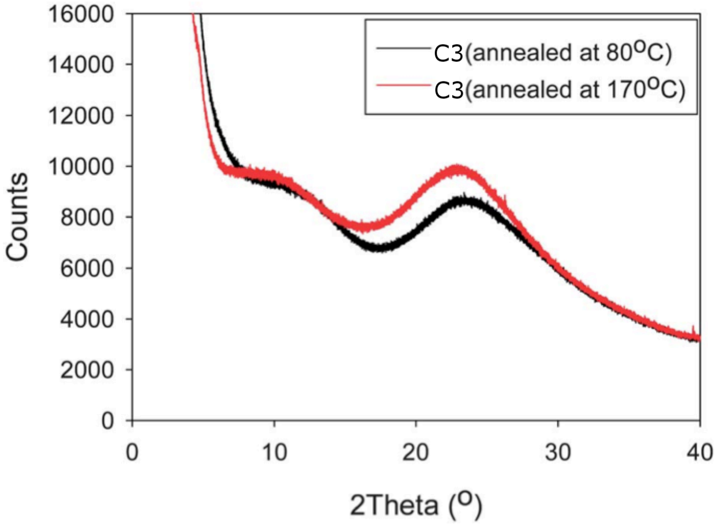

Figure 6.12: WAXS measurements of **C3** taken before and after cross-linking. WAXS data change corresponds to increased ordering of the polymer.

For further understanding of the structural development of the cross-linkable polymers and the cross-linking effect on PCBM aggregation, *in situ* cross-linking of **C3** and

C4, with and without PCBM, was investigated using grazing incidence small angle X-ray scattering (GISAXS). Samples were annealed for one hour at 170°C for **C3**, and 260°C for **C4**, above the cross-linking temperature. In-plane GISAXS profiles (Figure 6.13) were retrieved as a function of the in-plane scattering wavevector, q_{xy}. The GISAXS profile in Figure 6.13 (a) for the thin film of **C3** with less cross-linking density shows successively increased intensity in the q-region of 0.004–0.02 Å^{-1}, presumably owing to the formation of additionally large domains upon cross-linking. Correspondingly, GISAXS profile shown in Figure 6.13 (b) for the annealed thin film of **C3** revealed gradually enhanced scattering intensity in the higher q-region above 0.02 Å^{-1}, due to the characteristic $PC_{61}BM$ aggregation of 10–20 nm size. In contrast, the GISAXS profiles observed for the film of C4 without [Figure 6.13 (c)] or with $PC_{61}BM$ [Figure 6.13 (d)], reflect essentially no growth in the overall q-region observed. Likely, the very high cross-linking density restricted formation of additional polymer domains and completely suppressed PCBM aggregation.

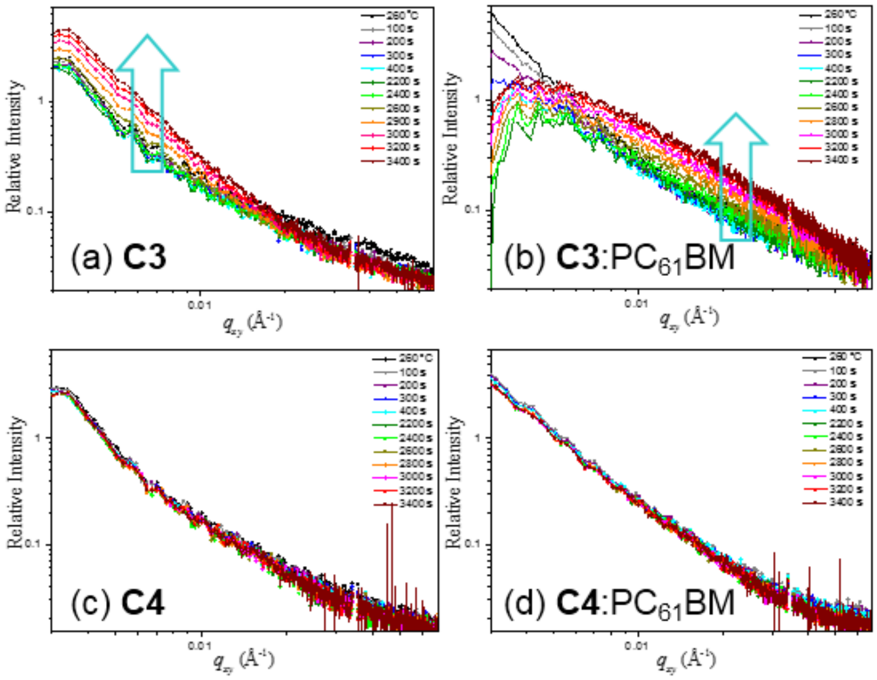

Figure 6.13: In-plane GISAXS profiles of thin films of (a) **C3**, (b) **C3**:$PC_{61}BM$, (c) **C4**, and (d) **C4**:$PC_{61}BM$, annealed at 260 °C for 1 hour. The arrows in (a) and (b) depict the characteristic intensity growths in different q_{xy}-regions resulted from the conjugated polymer cross-linking and $PC_{61}BM$ aggregation, respectively.

6.9 Summary

Cross-linkable analogues of PCPDTBT were characterised and used to fabricate OPV cells. To demonstrate the cross-linking occurrence, FTIR analysis demonstrated chemical changes consistent with cross-linking, however, these were only weakly observed in **C1** and **C3** due to fewer cross-linkable side chains. The cross-linking action was also shown by heating of the polymers **C1-4** to their respective cross-linking temperatures in solutions of chloroform, and all polymers became insoluble after sustained periods at the elevated temperatures. Of the four cross-linkable variants of PCPDTBT, three (**C1**, **C2**, **C4**) cross-linked at 260ºC with the other (**C3**) at 170ºC, so the latter remained the focus for device characterisation

Hole mobilities of PCPDTBT and **C3** were evaluated using SCLC devices. A control sample of PCPDTBT shoed decreasing hole mobility with increasing temperature, with a maximum mobility of 2.0 x 10^{-4} cm^2 V^{-1} s^{-1} recorded from annealing at 60^0C. Conversely, the hole mobility of **C3**'s hole increased with increasing temperature, reaching a maximum of 2.0 x 10^{-4} cm^2 V^{-1} s^{-1} at 170ºC.

OPV cells fabricated with both PCPDTBT and **C3** respectively showed similar PCEs, with **C3**·$PC_{61}BM$ and **C3**·$PC_{71}BM$ with ODT yielding PCEs of 1.84% and 3.65% respectively. OPV cells made with **C3** showed increased V_{OC} compared to PCPDTBT, due to its lower HOMO position. However, **C3** showed a lower value for J_{SC}, explained by the lower absorption.

Lifetime analysis of PCPDTBT and **C3** based cells showed that cross-linkable side chains increased stability. This increased stability was through more stable J_{SC} and FF, resulting in more stable PCE. It was found using AFM and GISAXS/GIWAXS measurements that the cross-linkable side chains resulting in a more stable morphology, by restricting PCBM aggregation.

Chapter 7 Conclusions and further work

The main focus of this thesis was to investigate improvements in OPV cell power conversion efficiencies (PCE) and lifetimes using materials made from the cyclopentadithiophene (CPDT) - benzothiadiazole (BT) monomer units.

Initial work focused on characterising new materials to evaluate their performances. In the first part of this section, the use of oligomers for donor materials in OPV cells was studied to assess their viability as an alternative to polymers for CPDT-BT solar cells. A donor-acceptor-donor (D-A-D) small molecule, of order CPDT-BT-CPDT (C2B1) was trialled, and an optical band gap of 1.8eV was measured. Evaporative OFETs and OPVs performed poorly. When processed from solution, OFET mobility was measured at 5×10^{-3} $cm^2.V^{-1}.s^{-1}$ in the saturation region. After blending with a fullerene derivative ($PC_{71}BM$) and also depositing from solution, a PCE of 1.57% was achieved under AM1.5G illumination. Due to the poor performance of the oligomer, the remaining research focused on donor-acceptor (D-A) polymers. PCPDTBT, synthesised using direct heterolytic arylation pathway, was characterised under AM1.5G and showed a PCE of 2.24% and 4.23% when blended with $PC_{61}BM$, and $PC_{71}BM$ with ODT, respectively. These cells outperformed those of Suzuki-coupled PCPDTBT (2.01% and 3.89% for $PC_{61}BM$, and $PC_{71}BM$ with ODT respectively) fabricated and tested at the same time. Prior to the commencement of this thesis, no working OPV cells had been demonstrated using polymers synthesised using direct-arylation, and to our knowledge this is the first known occurrence. This synthetic route offers the potential for high yield, high throughput and *green* synthesis of polymer material for OPV cells.

The second part of the thesis focused on characterising and understanding the stability of PCPDTBT, which was undertaken using a combination of OPV device data and analytical instruments. From device data, the material was shown to be less stable than the more commonly used P3HT polymer. The influence of including processing additives on device stability was also studied. PCPDTBT-based active layers including ODT possessed a reduced stability, halving the device half-life ($T_{50\%}$). EQE measurements were used to measure the spectral response as a function of time. By tracking the peak absorption wavelengths of PCPDTBT and $PC_{71}BM$ (793 nm and 483 nm respectively), PCBM was found to be the lesser stable component of the active layer. The physical changes were probed using AFM and GISAXS/GIWAXS, showing that the incorporation of the processing additive leads to reduced morphological stability during ageing experiments. A metric used to evaluate the long term stability was power generation over the cells' lifetime. When considering the power generated over the cell's lifetime, those made without ODT show greater output, despite the worse initial performance. The electrical power outputs were 840 $mWh.cm^{-2}$ and 1457 $mWh.cm^{-2}$ for encapsulated cells with and without ODT respectively. Non-encapsulated cells provided outputs of 131 $mWh.cm^{-2}$ and 150 $mWh.cm^{-2}$ for OPV cells with and without ODT respectively. Despite the initial higher performance of devices made with ODT, the poorer stability leads to less power generation over a cells' lifespan.

In an attempt to overcome the negative effects of ODT, alternative naphthalene-based processing additives were trialled. The PCE of $PCPDTBT{\cdot}PC_{71}BM$ devices containing ClN, BrN or ODT were measured as 2.30%, 1.72% and 2.95%, respectively. When looking at the metric of total extractable power, devices made with ClN performed best, despite the lower initial performance. AFM indicated that devices made with ClN provided a compromise between ODT (relatively smooth) and BrN (relatively rough), in terms of performance and stability.

XPS analysis was conducted on fresh and aged films of PCBM and PCPDTBT and blends of these materials, with and without processing additives. After ageing, XPS studies show that PCPDTBT appears as an oxygen-containing polymer, with data indicating that a break-up in the aromatic rings, formation of sulphates at the thiophene ring, chain scission in the polymer backbone and also loss of side chains. For films of fullerene derivatives, oxidation of carbon atoms in the fullerene cage and side chains are observed, including a breaking of the cage structure, after ageing. Films of $PCPDTBT{\cdot}PC_{61}BM$ and $PCPDTBT{\cdot}PC_{71}BM$ were also studied. The uptake of oxygen following light soaking was reduced when $PC_{71}BM$ was used instead of $PC_{61}BM$, inferring $PC_{71}BM$ to be more stable. Films of $PCPDTBT{\cdot}PC_{71}BM$ with ClN and ODT respectively were also studied, however, similar degradation was observed to films without processing additives. The level of oxidation in PCPDTBT·$PC_{71}BM$ films with and without processing additives do not correlate with the reduction in performance seen in OPV cells. This suggests that OPV cell degradation is determined mostly by physical rather than chemical changes. However, XPS data did show that ODT inclusion leads to greater morphological changes, supportive of the device, AFM and GISAXS/GIWAXS data.

Four cross-linkable analogues of PCPDTBT (**C1**-**C4**) were successfully characterised and used to fabricate OPV cells. FTIR analysis was used to demonstrate that chemical changes consistent with cross-linking did occur, most noticeably in **C2** and **C4**, due to the higher proportion of cross-linkable side chains. The cross-linking action was also shown by heating of the polymers **C1-4** to their respective cross-linking temperatures, in solutions of chloroform. In all cases, the polymers were shown to become insoluble after heating for one hour. Of the four cross-linkable variants of PCPDTBT, three (**C1**, **C2**, **C4**) cross-linked at 260ºC with the other (**C3**) at 170ºC. OPV cells therefore concentrated on active layers made with **C3**, which cross-links at a lower temperature of 170ºC.

Hole mobilities of a control sample of PCPDTBT and **C3** were evaluated using SCLC devices. A control sample of PCPDTBT showed decreasing hole mobility with increasing temperature, with a maximum mobility of 2.0×10^{-4} cm^2 V^{-1} s^{-1} recorded from annealing at 60^0C. Conversely, the hole mobility of **C3** increased with increasing temperature, reaching a maximum of 2.0×10^{-4} cm^2 V^{-1} s^{-1} at 170ºC. A much stronger peak was observed in the WAXS curve after cross-linking, suggesting that the action increases the order in the polymer film. This explains the increased hole mobility in **C3** after cross-linking

OPV cells fabricated with both a control sample of PCPDTBT and **C3** showed similar PCE performance. OPVs made with **C3**·$PC_{61}BM$ and **C3**·$PC_{71}BM$ with ODT demonstrated a PCE of 1.84% and 3.65% respectively. Cells made with **C3** showed increased V_{OC} compared to the control sample, which was to be expected owing to its lower HOMO level. However, **C3** showed reduced J_{SC} , which could be explained by the reduced optical absorption as witnessed from data in UV-visible spectra. The bulkier cross-linkable side chains of **C3** appear to have an impact on the polymer packing, which reduces the absorption in the active region.

When comparing the stability of OPVs made with **C3** and a control sample of PCPDTBT, **C3-**based OPV devices showed that cross-linkable side chains moderately increased stability. This was due to the increased stabilities of J_{SC} and FF, resulting in more stable PCE. AFM and GISAXS/GIWAXS measurements inferred that the cross-linkable side chains result in a more stable active layer morphology, limiting PCBM aggregation during light soaking.

7.1 Further work

Initial experimentation on the C2B1 oligomer was limited by the amount of material available. Evaporated C2B1 OFET devices and OPV cells showed inferior performance. Deposition parameters could be optimised, with a particular focus on investigating the effect of deposition rates upon oligomer disorder in the active layer. Due to the limited availability of materials, the effect of including additives in C2B1-based OPV cells, which could lead to performance enhancements, was also not considered. Some trials have also been undertaken by the author's group, using C2B1 as a sensitizer in P3HT- or PCPDTBT- solar cells [90]. Additionally, oligomers and polymers using different sequences of CPDT and BT monomers could be investigated. This could include oligomers of the structure CPDT-BT-CPDT-BT-CPDT, or polymers with alternating CPDT-CPDT-BT-BT.

A large part of this thesis was devoted to the detrimental effect that additives have on long-term stability. However, the use of additives cannot be completely ruled out for stable OPV devices, as alternatives could be available. Only 1-chloronaphthalene and 1-bromonaphthalene have been used so far, however 1-fluoronaphthalene and 1-iodonaphthalene are available. The effect of processing additive boiling point upon surface roughness and OPV cell lifetime should be explored further. This may lead to OPV cells with increased extractable electrical power.

In addition to naphthalene-based solvents, processing additives with boiling points well below the glass transition temperature of the active layer materials should be trialled. Increased temperatures are required to purge residual solvent, however this may in turn undo the beneficial effects due to excessive heating of the polymer. Not only does this lead to thermo-oxidation, it may, however, change the morphology via a different mechanism.

PCPDTBT-based OPV cells should be further investigated with a focus upon the long-term effects of temperature and humidity. This would require equipment capable of controlling the atmosphere during light soaking experimentation. Although temperature was constant at 50°C ± 5°C, it is hard to deduce what effect if any infrared radiation from the halogen light-soaking system had upon OPV cells. This could be developed further by investigating the effect of stability under different wavelengths.

Although potentially difficult, the active layers of encapsulated OPV cells should also be investigated using XPS, as the data in this thesis was focused on non-encapsulated samples. Improved packaging and de-packaging will need to be developed. Due to the restriction of molecular oxygen or water in active layer, XPS may shed light on potentially other degradation pathways. XPS studies may also yield further information regarding any chemical changes occurring within cross-linkable PCPDTBT. For both encapsulated and cross-linked PCPDTBT, depth profiling using XPS may yield further information about chemical changes with respect to material concentration.

Cross-linkable PCPDTBT demonstrated relatively high PCEs with increased stability. **C4** could demonstrate even greater OPV cell stability, if it wasn't for its high cross-linking temperature. Different side chain structures, with the same number of cross-linkable side chain groups, could be investigated to reduce the cross-linking temperature. The remarkably high J_{SC} for cross-linkable PCPDTBT, given its significantly lower absorption, makes the material worthy of further investigation. Based upon GISAXS data, where the PCBM is shown to aggregate, it might be worth trialling cross linkable PCBM to improve stability.

References

1. Administration, U. S. E. I. *International Energy Outlook 2014*. (2014).

2. Government, U. *UK Renewable Energy Roadmap Update 2013*. (2013).

3. MacKay, D. J. C. *Sustainable Energy--without the Hot Air*. (UIT, 2009). at <http://books.google.co.uk/books?id=IsgiPQAACAAJ>

4. *UK Solar PV Strategy Part 2*. (2014).

5. Parida, B., Iniyan, S. & Goic, R. A review of solar photovoltaic technologies. *Renew. Sustain. Energy Rev.* **15,** 1625–1636 (2011).

6. Nayak, P. K. & Cahen, D. Updated Assessment of Possibilities and Limits for Solar Cells. *Adv. Mater.* **26,** 1622–1628 (2014).

7. Palm, J., Probst, V. & Karg, F. H. Second generation CIS solar modules. *Sol. Energy* **77,** 757–765 (2004).

8. Green, M. A. Third generation photovoltaics: solar cells for 2020 and beyond. *Phys. E Low-dimensional Syst. Nanostructures* **14,** 65–70 (2002).

9. Thin Film Module Technology. *First Solar* (2015). at <http://www.firstsolar.com/en/technologies and capabilities/pv-modules/first-solar-series-3-black-module/cdte-technology>

10. Facchetti, A. π-Conjugated Polymers for Organic Electronics and Photovoltaic Cell Applications. *Chem. Mater.* **23,** 733–758 (2010).

11. Green, M. A., Emery, K., Hishikawa, Y., Warta, W. & Dunlop, E. D. Solar cell efficiency tables (version 44). *Prog. Photovoltaics Res. Appl.* **22,** 701–710 (2014).

12. Jørgensen, M. *et al.* Stability of Polymer Solar Cells. *Adv. Mater.* **24,** 580–612 (2012).

13. Coppo, P. & Turner, M. L. Cyclopentadithiophene based electroactive materials. *J. Mater. Chem.* **15,** 1123–1133 (2005).

14. Lu, J. *et al.* Crystalline low band-gap alternating indolocarbazole and benzothiadiazole-cored oligothiophene copolymer for organic solar cell applications. *Chem. Commun.* 5315–5317 (2008). doi:10.1039/B811031J

15. Peters, C. H. Lifetime and reliability of polymer solar cells. (Stanford University, 2011).

16. Douglas, J. D. The Development of Semiconducting Materials for Organic Photovoltaics. (University of California, Berkeley, 2013).

17. Scharber, M. C. *et al.* Design Rules for Donors in Bulk-Heterojunction Solar Cells--Towards 10% Energy-Conversion Efficiency. *Adv. Mater.* **18,** 789–794 (2006).

18. Gadisa, A., Svensson, M., Andersson, M. R. & Inganäs, O. Correlation between oxidation potential and open-circuit voltage of composite solar cells based on blends of polythiophenes/ fullerene derivative. *Appl. Phys. Lett.* **84,** (2004).

19. Garcia-Belmonte, G. & Bisquert, J. Open-circuit voltage limit caused by recombination through tail states in bulk heterojunction polymer-fullerene solar cells. *Appl. Phys. Lett.* **96,** - (2010).

20. Cowan, S. R., Roy, A. & Heeger, A. J. Recombination in polymer-fullerene bulk heterojunction solar cells. *Phys. Rev. B* **82,** 245207 (2010).

21. Mihailetchi, V. D., Blom, P. W. M., Hummelen, J. C. & Rispens, M. T. Cathode dependence of the open-circuit voltage of polymer:fullerene bulk heterojunction solar cells. *J. Appl. Phys.* **94,** 6849–6854 (2003).

22. Vandewal, K. *et al.* Varying polymer crystallinity in nanofiber poly(3-alkylthiophene): PCBM solar cells: Influence on charge-transfer state energy and open-circuit voltage. *Appl. Phys. Lett.* **95,** - (2009).

23. BUNDGAARD, E. & KREBS, F. C. Low band gap polymers for organic photovoltaics. *Sol. Energy Mater. Sol. Cells* **91,** 954–985 (2007).

24. Dou, L. *et al.* Tandem polymer solar cells featuring a spectrally matched low-bandgap polymer. *Nat Phot.* **6,** 180–185 (2012).

25. Nicholson, P. G. & Castro, F. A. Organic photovoltaics: principles and techniques for nanometre scale characterization. *Nanotechnology* **21,** 492001 (2010).

26. Tang, C. W. Two-layer organic photovoltaic cell. *Appl. Phys. Lett.* **48,** 183–185 (1986).

27. Slota, J. E., He, X. & Huck, W. T. S. Controlling nanoscale morphology in polymer photovoltaic devices. *Nano Today* **5,** 231–242 (2010).

28. Steim, R., Kogler, F. R. & Brabec, C. J. Interface materials for organic solar cells. *J. Mater. Chem.* **20,** 2499–2512 (2010).

29. Hong, K. *et al.* Reducing the contact resistance in organic thin-film transistors by introducing a PEDOT:PSS hole-injection layer. *Org. Electron.* **9,** 864–868 (2008).

30. Friedel, B. *et al.* Effects of Layer Thickness and Annealing of PEDOT:PSS Layers in Organic Photodetectors. *Macromolecules* **42,** 6741–6747 (2009).

31. Timpanaro, S., Kemerink, M., Touwslager, F. J., De Kok, M. M. & Schrader, S. Morphology and conductivity of PEDOT/PSS films studied by scanning–tunneling microscopy. *Chem. Phys. Lett.* **394,** 339–343 (2004).

32. Huang, J., Miller, P. F., de Mello, J. C., de Mello, A. J. & Bradley, D. D. C. Influence of thermal treatment on the conductivity and morphology of PEDOT/PSS films. *Synth. Met.* **139,** 569–572 (2003).

33. Wakizaka, D., Fushimi, T., Ohkita, H. & Ito, S. Hole transport in conducting ultrathin films of PEDOT/PSS prepared by layer-by-layer deposition technique. *Polymer (Guildf).* **45,** 8561–8565 (2004).

34. Krebs, F. C., Gevorgyan, S. A. & Alstrup, J. A roll-to-roll process to flexible polymer solar cells: model studies, manufacture and operational stability studies. *J. Mater. Chem.* **19,** 5442–5451 (2009).

35. Krebs, F. C. All solution roll-to-roll processed polymer solar cells free from indium-tin-oxide and vacuum coating steps. *Org. Electron.* **10,** 761–768 (2009).

36. Zhang, F. J. *et al.* Energy level alignment and morphology of interfaces between molecular and polymeric organic semiconductors. *Org. Electron.* **8,** 606–614 (2007).

37. Ciná, S. *et al.* P-135: Efficient Electron Injection from PEDOT-PSS into a Graded-n-doped Electron Transporting Layer in an Inverted OLED Structure. *SID Symp. Dig. Tech. Pap.* **36,** 819–821 (2005).

38. Meyer, J. *et al.* Transition Metal Oxides for Organic Electronics: Energetics, Device Physics and Applications. *Adv. Mater.* **24,** 5408–5427 (2012).

39. Kettle, J., Waters, H., Horie, M. & Chang, S.-W. Effect of hole transporting layers on the performance of PCPDTBT : PCBM organic solar cells. *Journal of Physics D: Applied Physics* **45,** 125102 (2012).

40. Tseng, Y.-C., Mane, A. U., Elam, J. W. & Darling, S. B. Ultrathin molybdenum oxide anode buffer layer for organic photovoltaic cells formed using atomic layer deposition. *Sol. Energy Mater. Sol. Cells* **99,** 235–239 (2012).

41. Irwin, M. D., Buchholz, D. B., Hains, A. W., Chang, R. P. H. & Marks, T. J. p-Type semiconducting nickel oxide as an efficiency-enhancing anode interfacial layer in

polymer bulk-heterojunction solar cells. *Proc. Natl. Acad. Sci.* **105** **,** 2783–2787 (2008).

42. Hancox, I. *et al.* Optimization of a High Work Function Solution Processed Vanadium Oxide Hole-Extracting Layer for Small Molecule and Polymer Organic Photovoltaic Cells. *J. Phys. Chem. C* **117,** 49–57 (2013).

43. Steirer, K. X. *et al.* Solution deposited NiO thin-films as hole transport layers in organic photovoltaics. *Org. Electron.* **11,** 1414–1418 (2010).

44. Oh, I., Kim, G., Han, S. & Oh, S. PEDOT:PSS-free organic photovoltaic cells using tungsten oxides as buffer layer on anodes. *Electron. Mater. Lett.* **9,** 375–379 (2013).

45. Waldauf, C. *et al.* Highly efficient inverted organic photovoltaics using solution based titanium oxide as electron selective contact. *Appl. Phys. Lett.* **89,** - (2006).

46. Roesch, R., Eberhardt, K.-R., Engmann, S., Gobsch, G. & Hoppe, H. Polymer solar cells with enhanced lifetime by improved electrode stability and sealing. *Sol. Energy Mater. Sol. Cells* **117,** 59–66 (2013).

47. Zhang, F. *et al.* Recent development of the inverted configuration organic solar cells. *Sol. Energy Mater. Sol. Cells* **95,** 1785–1799 (2011).

48. Girtan, M. Comparison of ITO/metal/ITO and ZnO/metal/ZnO characteristics as transparent electrodes for third generation solar cells. *Sol. Energy Mater. Sol. Cells* **100,** 153–161 (2012).

49. Li, H. *et al.* Zinc Oxide as a Model Transparent Conducting Oxide: A Theoretical and Experimental Study of the Impact of Hydroxylation, Vacancies, Interstitials, and Extrinsic Doping on the Electronic Properties of the Polar ZnO (0002) Surface. *Chem. Mater.* **24,** 3044–3055 (2012).

50. Fortunato, E., Ginley, D., Hosono, H. & Paine, D. C. Transparent Conducting Oxides for Photovoltaics. *MRS Bull.* **32,** 242–247 (2007).

51. Chen, F.-C., Wu, J.-L., Hsieh, K.-H., Chen, W.-C. & Lee, S.-W. Polymer photovoltaic devices with highly transparent cathodes. *Org. Electron.* **9,** 1132–1135 (2008).

52. Wang, J.-C. *et al.* Highly efficient flexible inverted organic solar cells using atomic layer deposited ZnO as electron selective layer. *J. Mater. Chem.* **20,** 862–866 (2010).

53. Sun, Z., Shi, S., Bao, Q., Liu, X. & Fahlman, M. Role of Thick-Lithium Fluoride Layer in Energy Level Alignment at Organic/Metal Interface: Unifying Effect on High Metallic Work Functions. *Adv. Mater. Interfaces* **2,** n/a–n/a (2015).

54. Eo, Y. S., Rhee, H. W., Chin, B. D. & Yu, J.-W. Influence of metal cathode for organic photovoltaic device performance. *Synth. Met.* **159,** 1910–1913 (2009).

55. De Bettignies, R., Leroy, J., Firon, M. & Sentein, C. Accelerated lifetime measurements of P3HT:PCBM solar cells. *Synth. Met.* **156,** 510–513 (2006).

56. Hau, S. K. *et al.* Air-stable inverted flexible polymer solar cells using zinc oxide nanoparticles as an electron selective layer. *Appl. Phys. Lett.* **92,** - (2008).

57. Manor, A., Katz, E. A., Tromholt, T. & Krebs, F. C. Enhancing functionality of ZnO hole blocking layer in organic photovoltaics. *Sol. Energy Mater. Sol. Cells* **98,** 491–493 (2012).

58. Verbakel, F., Meskers, S. C. J. & Janssen, R. A. J. Electronic memory effects in diodes from a zinc oxide nanoparticle-polystyrene hybrid material. *Appl. Phys. Lett.* **89,** - (2006).

59. Bristow, N. & Kettle, J. Outdoor performance of organic photovoltaics: Diurnal analysis, dependence on temperature, irradiance, and degradation. *J. Renew. Sustain. Energy* **7,** - (2015).

60. Kim, J. Y. *et al.* New Architecture for High-Efficiency Polymer Photovoltaic Cells Using Solution-Based Titanium Oxide as an Optical Spacer. *Adv. Mater.* **18,** 572–576 (2006).

61. Park, S. H. *et al.* Bulk heterojunction solar cells with internal quantum efficiency approaching 100%. *Nat. Photonics* **3,** 297–302 (2009).

62. Koster, L. J. A., Mihailetchi, V. D. & Blom, P. W. M. Ultimate efficiency of polymer/fullerene bulk heterojunction solar cells. *Appl. Phys. Lett.* **88,** 93511–93513 (2006).

63. Krebs, F. C. *Stability and Degradation of Organic and Polymer Solar Cells.* (John Wiley & Sons, 2012).

64. BUNDGAARD, E. & KREBS, F. Low band gap polymers for organic photovoltaics. *Sol. Energy Mater. Sol. Cells* **91,** 954–985 (2007).

65. Kitamura, C., Tanaka, S. & Yamashita, Y. Design of Narrow-Bandgap Polymers. Syntheses and Properties of Monomers and Polymers Containing Aromatic-Donor and o-Quinoid-Acceptor Units. *Chem. Mater.* **8,** 570–578 (1996).

66. Huang, W. *et al.* Unraveling the Morphology of High Efficiency Polymer Solar Cells Based on the Donor Polymer PBDTTT-EFT. *Adv. Energy Mater.* n/a–n/a (2014). doi:10.1002/aenm.201401259

67. Wu, J.-S., Cheng, S.-W., Cheng, Y.-J. & Hsu, C.-S. Donor-acceptor conjugated polymers based on multifused ladder-type arenes for organic solar cells. *Chem. Soc. Rev.* **44,** 1113–1154 (2015).

68. Yang, T. *et al.* Inverted polymer solar cells with 8.4% efficiency by conjugated polyelectrolyte. *Energy Environ. Sci.* **5,** 8208–8214 (2012).

69. He, Z. *et al.* Simultaneous enhancement of open-circuit voltage, short-circuit current density, and fill factor in polymer solar cells. *Adv. Mater.* **23,** 4636–43 (2011).

70. Sariciftci, N. S. *et al.* Semiconducting polymer-buckminsterfullerene heterojunctions: Diodes, photodiodes, and photovoltaic cells. *Appl. Phys. Lett.* **62,** 585–587 (1993).

71. Yu, G., Gao, J., Hummelen, J. C., Wudl, F. & Heeger, A. J. Polymer Photovoltaic Cells: Enhanced Efficiencies via a Network of Internal Donor-Acceptor Heterojunctions. *Science (80-.).* **270,** 1789–1891 (1995).

72. Svensson, M. *et al.* High-Performance Polymer Solar Cells of an Alternating Polyfluorene Copolymer and a Fullerene Derivative. *Adv. Mater.* **15,** 988–991 (2003).

73. Chen, M.-H. *et al.* Efficient Polymer Solar Cells with Thin Active Layers Based on Alternating Polyfluorene Copolymer/Fullerene Bulk Heterojunctions. *Adv. Mater.* **21,** 4238–4242 (2009).

74. Wang, E. *et al.* High-performance polymer heterojunction solar cells of a polysilafluorene derivative. *Appl. Phys. Lett.* **92,** - (2008).

75. Dang, M. T., Hirsch, L. & Wantz, G. P3HT:PCBM, Best Seller in Polymer Photovoltaic Research. *Adv. Mater.* **23,** 3597–3602 (2011).

76. Zhou, Y. *et al.* Efficiency enhancement for bulk-heterojunction hybrid solar cells based on acid treated CdSe quantum dots and low bandgap polymer PCPDTBT. *Sol. Energy Mater. Sol. Cells* **95,** 1232–1237 (2011).

77. Hou, J., Chen, H.-Y., Zhang, S., Li, G. & Yang, Y. Synthesis, Characterization, and Photovoltaic Properties of a Low Band Gap Polymer Based on Silole-Containing Polythiophenes and 2,1,3-Benzothiadiazole. *J. Am. Chem. Soc.* **130,** 16144–16145 (2008).

78. He, Z. *et al.* Enhanced power-conversion efficiency in polymer solar cells using an inverted device structure. *Nat. Photonics* **6,** 591–595 (2012).

79. Zhang, S. *et al.* Side Chain Selection for Designing Highly Efficient Photovoltaic Polymers with 2D-Conjugated Structure. *Macromolecules* **47,** 4653–4659 (2014).

80. Mühlbacher, D. *et al*. High photovoltaic performance of a low-bandgap polymer. *Adv. Mater.* **18,** 2884–2889 (2006).

81. Peet, J. *et al*. Efficiency enhancement in low-bandgap polymer solar cells by processing with alkane dithiols. *Nat. Mater.* **6,** 497–500 (2007).

82. Brunetti, F. G., Kumar, R. & Wudl, F. Organic electronics from perylene to organic photovoltaics: painting a brief history with a broad brush. *J. Mater. Chem.* **20,** 2934–2948 (2010).

83. Collins, B. A., Li, Z., McNeill, C. R. & Ade, H. Fullerene-Dependent Miscibility in the Silole-Containing Copolymer PSBTBT-08. *Macromolecules* **44,** 9747–9751 (2011).

84. Lee, J. K. *et al*. Processing additives for improved efficiency from bulk heterojunction solar cells. *J. Am. Chem. Soc.* **130,** 3619–3623 (2008).

85. Alem, S. *et al*. Effect of mixed solvents on PCDTBT:PC70BM based solar cells. *Org. Electron.* **12,** 1788–1793 (2011).

86. Günes, S. & Sariciftci, N. S. Hybrid solar cells. *Inorganica Chim. Acta* **361,** 581–588 (2008).

87. Krebs, F. C. *et al*. Manufacture, integration and demonstration of polymer solar cells in a lamp for the 'Lighting Africa' initiative. *Energy Environ. Sci.* **3,** 512–525 (2010).

88. Liu, C.-Y., Holman, Z. C. & Kortshagen, U. R. Hybrid Solar Cells from P3HT and Silicon Nanocrystals. *Nano Lett.* **9,** 449–452 (2009).

89. Lloyd, M. T., Anthony, J. E. & Malliaras, G. G. Photovoltaics from soluble small molecules. *Mater. Today* **10,** 34–41 (2007).

90. Chang, S. W., Waters, H., Kettle, J. & Horie, M. Cyclopentadithiophene-benzothiadiazole oligomers: Synthesis via direct arylation, X-ray crystallography, optical properties, solution casted field-effect transistor and photovoltaic characteristics. *Org. Electron. physics, Mater. Appl.* **13,** 2967–2974 (2012).

91. Allard, S., Forster, M., Souharce, B., Thiem, H. & Scherf, U. Organic Semiconductors for Solution-Processable Field-Effect Transistors (OFETs). *Angew. Chemie Int. Ed.* **47,** 4070–4098 (2008).

92. Mas-Torrent, M. & Rovira, C. Novel small molecules for organic field-effect transistors: towards processability and high performance. *Chem. Soc. Rev.* **37,** 827–838 (2008).

93. Chen, Y.-H. *et al.* Vacuum-Deposited Small-Molecule Organic Solar Cells with High Power Conversion Efficiencies by Judicious Molecular Design and Device Optimization. *J. Am. Chem. Soc.* **134,** 13616–13623 (2012).

94. Zhou, J. *et al.* Solution-Processed and High-Performance Organic Solar Cells Using Small Molecules with a Benzodithiophene Unit. *J. Am. Chem. Soc.* **135,** 8484–8487 (2013).

95. Jia, T. *et al.* Synthesis of four-armed triphenylamine-based molecules and their applications in organic solar cells. *New J. Chem.* - (2015). doi:10.1039/C4NJ01537A

96. Yoo, S., Domercq, B. & Kippelen, B. Efficient thin-film organic solar cells based on pentacene/C60 heterojunctions. *Appl. Phys. Lett.* **85,** 5427–5429 (2004).

97. Uchida, S., Xue, J., Rand, B. P. & Forrest, S. R. Organic small molecule solar cells with a homogeneously mixed copper phthalocyanine: C 60 active layer. *Appl. Phys. Lett.* **84,** 4218–4220 (2004).

98. Loser, S. *et al.* Naphthodithiophene-Diketopyrrolopyrrole Small Molecule Donors for Efficient Solution-Processed Solar Cells. in *MRS Proceedings* **1390,** mrsf11–1390 (2012).

99. Beaujuge, P. M. & Fréchet, J. M. J. Molecular design and ordering effects in π-functional materials for transistor and solar cell applications. *J. Am. Chem. Soc.* **133,** 20009–20029 (2011).

100. Chen, J. & Cao, Y. Development of novel conjugated donor polymers for high-efficiency bulk-heterojunction photovoltaic devices. *Acc. Chem. Res.* **42,** 1709–1718 (2009).

101. Burke, D. J. & Lipomi, D. J. Green chemistry for organic solar cells. *Energy Environ. Sci.* **6,** 2053–2066 (2013).

102. Clayden, J., Greeves, N. & Warren, S. *Organic Chemistry*. (OUP Oxford, 2012). at <https://books.google.co.uk/books?id=kQgu2j_ber0C>

103. Carlé, J. E. Polymer synthesis. *DTU Energy* at <http://plasticphotovoltaics.org/lc/lc-materials/lc-synthesis.html>

104. Suzuki, A. Recent advances in the cross-coupling reactions of organoboron derivatives with organic electrophiles, 1995-1998. *J. Organomet. Chem.* **576,** 147–168 (1999).

105. Kowalski, S., Allard, S. & Scherf, U. Synthesis of Poly(4,4-dialkyl-cyclopenta[2,1-b:3,4-b?]dithiophene-alt-2,1,3-benzothiadiazole) (PCPDTBT) in a Direct Arylation Scheme. *ACS Macro Lett.* **1,** 465–468 (2012).

106. Bard, A. J., Stratmann, M. & Licht, S. *Encyclopedia of Electrochemistry, Volume 6, Semiconductor Electrodes and Photoelectrochemistry*. (2002).

107. Duan, C., Huang, F. & Cao, Y. Recent development of push--pull conjugated polymers for bulk-heterojunction photovoltaics: rational design and fine tailoring of molecular structures. *J. Mater. Chem.* **22,** 10416–10434 (2012).

108. Kim, J. Y. *et al*. Efficient tandem polymer solar cells fabricated by all-solution processing. *Science* **317,** 222–225 (2007).

109. Blakesley, J. C. *et al*. Towards reliable charge-mobility benchmark measurements for organic semiconductors. *Org. Electron.* **15,** 1263–1272 (2014).

110. Torres, T. & Bottari, G. *Organic Nanomaterials: Synthesis, Characterization, and Device Applications*. (Wiley, 2013). at <https://books.google.co.uk/books?id=jdtvAAAAQBAJ>

111. Kymissis, I. *Organic Field Effect Transistors: Theory, Fabrication and Characterization*. (Springer, 2008). at <https://books.google.co.uk/books?id=GD_ry6FtSEQC>

112. Zhang, M. *et al*. Field-Effect Transistors Based on a Benzothiadiazole–Cyclopentadithiophene Copolymer. *J. Am. Chem. Soc.* **129,** 3472–3473 (2007).

113. Tsao, H. N. *et al*. Ultrahigh Mobility in Polymer Field-Effect Transistors by Design. *J. Am. Chem. Soc.* **133,** 2605–2612 (2011).

114. Sirringhaus, H., Bird, M. & Zhao, N. Charge Transport Physics of Conjugated Polymer Field-Effect Transistors. *Adv. Mater.* **22,** 3893–3898 (2010).

115. Limketkai, B. N. Charge-carrier transport in amorphous organic semiconductors. (Massachusetts Institute of Technology, 2008).

116. Lanzani, G. *Photophysics of Molecular Materials: From Single Molecules to Single Crystals*. (Wiley, 2006). at <https://books.google.co.uk/books?id=xEQXLB-zf4UC>

117. Sun, S. S. & Sariciftci, N. S. *Organic Photovoltaics: Mechanisms, Materials, and Devices*. (CRC Press, 2010). at <https://books.google.co.uk/books?id=0RHNYMQmOVsC>

118. Kettle, J. *et al*. Optimisation of PCPDTBT solar cells using polymer synthesis with Suzuki coupling. *Sol. Energy Mater. Sol. Cells* **95,** 2186–2193 (2011).

119. Hertel, D. & Bässler, H. Photoconduction in Amorphous Organic Solids. *ChemPhysChem* **9,** 666–688 (2008).

120. Perez, M. D., Borek, C., Forrest, S. R. & Thompson, M. E. Molecular and morphological influences on the open circuit voltages of organic photovoltaic devices. *J. Am. Chem. Soc.* **131,** 9281–9286 (2009).

121. Lenes, M., Morana, M., Brabec, C. J. & Blom, P. W. M. Recombination-Limited Photocurrents in Low Bandgap Polymer/Fullerene Solar Cells. *Adv. Funct. Mater.* **19,** 1106–1111 (2009).

122. Agostinelli, T. *et al.* Real-Time Investigation of Crystallization and Phase-Segregation Dynamics in P3HT:PCBM Solar Cells During Thermal Annealing. *Adv. Funct. Mater.* **21,** 1701–1708 (2011).

123. Ray, B. & Alam, M. A. A compact physical model for morphology induced intrinsic degradation of organic bulk heterojunction solar cell. *Appl. Phys. Lett.* **99,** - (2011).

124. Campoy-Quiles, M. *et al.* Morphology evolution via self-organization and lateral and vertical diffusion in polymer:fullerene solar cell blends. *Nat Mater* **7,** 158–164 (2008).

125. Drummy, L. F. *et al.* Molecular-Scale and Nanoscale Morphology of P3HT:PCBM Bulk Heterojunctions: Energy-Filtered TEM and Low-Dose HREM. *Chem. Mater.* **23,** 907–912 (2011).

126. Wang, T. *et al.* The development of nanoscale morphology in polymer:fullerene photovoltaic blends during solvent casting. *Soft Matter* **6,** 4128–4134 (2010).

127. Yu, J., Zheng, Y. & Huang, J. Towards High Performance Organic Photovoltaic Cells: A Review of Recent Development in Organic Photovoltaics. *Polymers (Basel).* **6,** 2473–2509 (2014).

128. Tang, H. *et al.* Precise construction of PCBM aggregates for polymer solar cells via multi-step controlled solvent vapor annealing. *J. Mater. Chem.* **20,** 683–688 (2010).

129. Moulé, A. J. & Meerholz, K. Morphology Control in Solution-Processed Bulk-Heterojunction Solar Cell Mixtures. *Adv. Funct. Mater.* **19,** 3028–3036 (2009).

130. Lunt, R. R., Giebink, N. C., Belak, A. A., Benziger, J. B. & Forrest, S. R. Exciton diffusion lengths of organic semiconductor thin films measured by spectrally resolved photoluminescence quenching. *J. Appl. Phys.* **105,** - (2009).

131. Etzold, F. *et al.* The Effect of Solvent Additives on Morphology and Excited-State Dynamics in PCPDTBT:PCBM Photovoltaic Blends. *J. Am. Chem. Soc.* **134,** 10569–10583 (2012).

132. Albrecht, S. *et al.* On the field dependence of free charge carrier generation and recombination in blends of PCPDTBT/PC70BM: influence of solvent additives. *J. Phys. Chem. Lett.* **3,** 640–645 (2012).

133. Gu, Y., Wang, C. & Russell, T. P. Multi-Length-Scale Morphologies in PCPDTBT/PCBM Bulk-Heterojunction Solar Cells. *Adv. Energy Mater.* **2,** 683–690 (2012).

134. Horie, M. *et al.* Cyclopentadithiophene-benzothiadiazole oligomers and polymers; synthesis, characterisation, field-effect transistor and photovoltaic characteristics. *J. Mater. Chem.* **22,** 381–389 (2012).

135. Griffini, G. *et al.* Long-Term Thermal Stability of High-Efficiency Polymer Solar Cells Based on Photocrosslinkable Donor-Acceptor Conjugated Polymers. *Adv. Mater.* **23,** 1660–1664 (2011).

136. Kim, H. J. *et al.* Solvent-resistant organic transistors and thermally stable organic photovoltaics based on cross-linkable conjugated polymers. *Chem. Mater.* **24,** 215–221 (2011).

137. Hsieh, C.-H. *et al.* Highly efficient and stable inverted polymer solar cells integrated with a cross-linked fullerene material as an interlayer. *J. Am. Chem. Soc.* **132,** 4887–4893 (2010).

138. Cheng, Y.-J., Hsieh, C.-H., Li, P.-J. & Hsu, C.-S. Morphological stabilization by in situ polymerization of fullerene derivatives leading to efficient, thermally stable organic photovoltaics. *Adv. Funct. Mater.* **21,** 1723–1732 (2011).

139. Gearba, I. R., Nam, C.-Y., Pindak, R. & Black, C. T. Thermal crosslinking of organic semiconducting polythiophene improves transverse hole conductivity. *Appl. Phys. Lett.* **95,** - (2009).

140. Wantz, G. *et al.* Stabilizing polymer-based bulk heterojunction solar cells via crosslinking. *Polym. Int.* **63,** 1346–1361 (2014).

141. Reese, M. O. *et al.* Consensus stability testing protocols for organic photovoltaic materials and devices. *Sol. Energy Mater. Sol. Cells* **95,** 1253–1267 (2011).

142. Manceau, M. *et al.* Effects of long-term UV-visible light irradiation in the absence of oxygen on P3HT and P3HT:PCBM blend. *Sol. Energy Mater. Sol. Cells* **94,** 1572–1577 (2010).

143. Neugebauer, H., Brabec, C., Hummelen, J. C. & Sariciftci, N. S. Stability and photodegradation mechanisms of conjugated polymer/fullerene plastic solar cells. *Sol. Energy Mater. Sol. Cells* **61,** 35–42 (2000).

144. Paci, B. *et al.* Structural/morphological monitoring approach to stability and durability issues of photoactive films for organic solar cells. *Chem. Phys. Lett.* **504,** 216–220 (2011).

145. Hintz, H., Egelhaaf, H.-J., Peisert, H. & Chassé, T. Photo-oxidation and ozonization of poly(3-hexylthiophene) thin films as studied by UV/VIS and photoelectron spectroscopy. *Polym. Degrad. Stab.* **95,** 818–825 (2010).

146. Manceau, M., Rivaton, A., Gardette, J.-L., Guillerez, S. & Lemaître, N. The mechanism of photo- and thermooxidation of poly(3-hexylthiophene) (P3HT) reconsidered. *Polym. Degrad. Stab.* **94,** 898–907 (2009).

147. Reese, M. O. *et al.* Photoinduced Degradation of Polymer and Polymer–Fullerene Active Layers: Experiment and Theory. *Adv. Funct. Mater.* **20,** 3476–3483 (2010).

148. Kumar, A., Hong, Z., Sista, S. & Yang, Y. The Critical Role of Processing and Morphology in Determining Degradation Rates in Polymer Solar Cells. *Adv. Energy Mater.* **1,** 124–131 (2011).

149. Keivanidis, P. E. *et al.* Dependence of Charge Separation Efficiency on Film Microstructure in Poly(3-hexylthiophene-2,5-diyl):[6,6]-Phenyl-C61 Butyric Acid Methyl Ester Blend Films. *J. Phys. Chem. Lett.* **1,** 734–738 (2010).

150. Wang, N., Tong, X., Burlingame, Q., Yu, J. & Forrest, S. R. Photodegradation of small-molecule organic photovoltaics. *Sol. Energy Mater. Sol. Cells* **125,** 170–175 (2014).

151. Jørgensen, M., Norrman, K. & Krebs, F. C. Stability/degradation of polymer solar cells. *Sol. Energy Mater. Sol. Cells* **92,** 686–714 (2008).

152. Liu, S.-W. *et al.* 4-Hydroxy-8-methyl-1{,}5-naphthyridine aluminium chelate: a morphologically stable and efficient exciton-blocking material for organic photovoltaics with prolonged lifetime. *J. Mater. Chem.* **20,** 7800–7806 (2010).

153. Würthner, F. *et al.* Supramolecular p−n-Heterojunctions by Co-Self-Organization of Oligo(p-phenylene Vinylene) and Perylene Bisimide Dyes. *J. Am. Chem. Soc.* **126,** 10611–10618 (2004).

154. Kamkar, D. A., Wang, M., Wudl, F. & Nguyen, T.-Q. Single Nanowire OPV Properties of a Fullerene-Capped P3HT Dyad Investigated Using Conductive and Photoconductive AFM. *ACS Nano* **6,** 1149–1157 (2012).

155. Seo, H. O. *et al.* Studies of degradation behaviors of poly (3-hexylthiophene) layers by X-ray photoelectron spectroscopy. *Surf. Interface Anal.* **46,** 544–549 (2014).

156. Norrman, K., Madsen, M. V, Gevorgyan, S. A. & Krebs, F. C. Degradation Patterns in Water and Oxygen of an Inverted Polymer Solar Cell. *J. Am. Chem. Soc.* **132,** 16883–16892 (2010).

157. Feron, K., Nagle, T. J. T., Rozanski, L. L. J., Gong, B. B. & Fell, C. J. Spatially resolved photocurrent measurements of organic solar cells: Tracking water ingress at edges and pinholes. *Sol. Energy Mater. Sol. Cells* **109,** 169–177 (2013).

158. Grossiord, N., Kroon, J. M., Andriessen, R. & Blom, P. W. M. Degradation mechanisms in organic photovoltaic devices. *Org. Electron.* **13,** 432–456 (2012).

159. Tapponnier, A., Biaggio, I. & Günter, P. Ultrapure C60 field-effect transistors and the effects of oxygen exposure. *Appl. Phys. Lett.* **86,** - (2005).

160. Creegan, K. M. *et al.* Synthesis and characterization of C60O, the first fullerene epoxide. *J. Am. Chem. Soc.* **114,** 1103–1105 (1992).

161. Könenkamp, R., Priebe, G. & Pietzak, B. Carrier mobilities and influence of oxygen in C60 films. *Phys. Rev. B* **60,** 11804–11808 (1999).

162. Bao, Q., Liu, X., Braun, S. & Fahlman, M. Oxygen- and Water-Based Degradation in [6,6]-Phenyl-C61-Butyric Acid Methyl Ester (PCBM) Films. *Adv. Energy Mater.* **4,** n/a–n/a (2014).

163. Camaioni, N. *et al.* A stabilization effect of [60]fullerene in donor–acceptor organic solar cells. *Sol. Energy Mater. Sol. Cells* **76,** 107–113 (2003).

164. Baral, J.K., Izquierdo, R., Packirisamy, M. & Truong, V.-V. Improved polymer solar cell performance by engineering of cathode interface. *Eur. Phys. J. Appl. Phys.* **55,** 30202 (2011).

165. Veldman, D., Bennett, I. J., Brockholz, B. & de Jong, P. C. Non-destructive testing of crystalline silicon photovoltaic back-contact modules. *Photovoltaic Specialists Conference (PVSC), 2011 37th IEEE* 3237–3240 (2011). doi:10.1109/PVSC.2011.6186628

166. Friend, R. H. *et al.* Electroluminescence in conjugated polymers. *Nature* **397,** 121–128 (1999).

167. Rosch, R. *et al.* Investigation of the degradation mechanisms of a variety of organic photovoltaic devices by combination of imaging techniques-the ISOS-3 inter-laboratory collaboration. *Energy Environ. Sci.* **5,** 6521–6540 (2012).

168. Sharma, A., Andersson, G. & Lewis, D. A. Role of humidity on indium and tin migration in organic photovoltaic devices. *Phys. Chem. Chem. Phys.* **13,** 4381–4387 (2011).

169. Sharma, A., Watkins, S. E., Lewis, D. A. & Andersson, G. Effect of indium and tin contamination on the efficiency and electronic properties of organic bulk hetero-junction solar cells. *Sol. Energy Mater. Sol. Cells* **95,** 3251–3255 (2011).

170. Wong, K. W. *et al.* Blocking reactions between indium-tin oxide and poly (3,4-ethylene dioxythiophene):poly(styrene sulphonate) with a self-assembly monolayer. *Appl. Phys. Lett.* **80,** (2002).

171. Schaer, M., Nüesch, F., Berner, D., Leo, W. & Zuppiroli, L. Water Vapor and Oxygen Degradation Mechanisms in Organic Light Emitting Diodes. *Adv. Funct. Mater.* **11,** 116–121 (2001).

172. Cros, S. *et al.* Definition of encapsulation barrier requirements: A method applied to organic solar cells. *Sol. Energy Mater. Sol. Cells* **95,** S65–S69 (2011).

173. Groner, M. D., George, S. M., McLean, R. S. & Carcia, P. F. Gas diffusion barriers on polymers using Al2O3 atomic layer deposition. *Appl. Phys. Lett.* **88,** - (2006).

174. Hauch, J. A., Schilinsky, P., Choulis, S. A., Rajoelson, S. & Brabec, C. J. The impact of water vapor transmission rate on the lifetime of flexible polymer solar cells. *Appl. Phys. Lett.* **93,** - (2008).

175. Huang, Z. H. Thin film encapsulation by e-beam evaporation of oxides. in *Electronics Packaging Technology Conference (EPTC), 2010 12th* 23–26 (2010). doi:10.1109/EPTC.2010.5702599

176. Ahmad, J., Bazaka, K., Anderson, L. J., White, R. D. & Jacob, M. V. Materials and methods for encapsulation of OPV: A review. *Renew. Sustain. Energy Rev.* **27,** 104–117 (2013).

177. Sarkar, S., Culp, J. H., Whyland, J. T., Garvan, M. & Misra, V. Encapsulation of organic solar cells with ultrathin barrier layers deposited by ozone-based atomic layer deposition. *Org. Electron.* **11,** 1896–1900 (2010).

178. Carcia, P. F., McLean, R. S., Groner, M. D., Dameron, A. A. & George, S. M. Gas diffusion ultrabarriers on polymer substrates using Al2O3 atomic layer deposition and SiN plasma-enhanced chemical vapor deposition. *J. Appl. Phys.* **106,** - (2009).

179. Lei, T. *Design, Synthesis, and Structure-Property Relationship Study of Polymer Field-Effect Transistors.* (Springer Berlin Heidelberg, 2015). at <https://books.google.co.uk/books?id=N_ASBgAAQBAJ>

180. Kagan, C. R. & Andry, P. *Thin-Film Transistors.* (Taylor & Francis, 2003). at <https://books.google.co.uk/books?id=YT5q2_mgap0C>

181. Sun, Y. *et al.* Polythiophene-based field-effect transistors with enhanced air stability. *Org. Electron.* **11,** 351–355 (2010).

182. Mihailetchi, V. D., Wildeman, J. & Blom, P. W. M. Space-Charge Limited Photocurrent. *Phys. Rev. Lett.* **94,** 126602 (2005).

183. Petty, M. C. *Molecular Electronics: From Principles to Practice*. (Wiley, 2008). at <https://books.google.co.uk/books?id=If7XW2f5DKAC>

184. Pereira, L. F. R. *Organic Light Emitting Diodes: The Use of Rare Earth and Transition Metals*. (Pan Stanford, 2012). at <https://books.google.co.uk/books?id=XYfOBQAAQBAJ>

185. Jiang, C. Y., Sun, X. W., Zhao, D. W., Kyaw, A. K. K. & Li, Y. N. Low work function metal modified ITO as cathode for inverted polymer solar cells. *Sol. Energy Mater. Sol. Cells* **94,** 1618–1621 (2010).

186. Sachtler, W. M. H., Dorgelo, G. J. H. & Holscher, A. A. The work function of gold. *Surf. Sci.* **5,** 221–229 (1966).

187. Moet, D. J. D. Enhanced performance of single and double junction plastic solar cells. (Rijksuniversiteit Groningen, 2011).

188. Moet, D. J. D. *et al.* Enhanced dissociation of charge-transfer states in narrow band gap polymer:fullerene solar cells processed with 1,8-octanedithiol. *Appl. Phys. Lett.* **96,** - (2010).

189. Rivnay, J., Mannsfeld, S. C. B., Miller, C. E., Salleo, A. & Toney, M. F. Quantitative Determination of Organic Semiconductor Microstructure from the Molecular to Device Scale. *Chem. Rev.* **112,** 5488–5519 (2012).

190. Zhan, X. & Zhu, D. Conjugated polymers for high-efficiency organic photovoltaics. *Polym. Chem.* **1,** 409–419 (2010).

191. Gunes, S., Neugebauer, H. & Sariciftci, N. S. Conjugated Polymer-Based Organic Solar Cells. *Chem. Rev.* **107,** 1324–1338 (2007).

192. Heeger, A. J. Semiconducting polymers: the Third Generation. *Chem. Soc. Rev.* **39,** 2354–2371 (2010).

193. Pron, A., Gawrys, P., Zagorska, M., Djurado, D. & Demadrille, R. Electroactive materials for organic electronics: preparation strategies, structural aspects and characterization techniques. *Chem. Soc. Rev.* **39,** 2577–2632 (2010).

194. Klauk, H. Organic thin-film transistors. *Chem. Soc. Rev.* **39,** 2643–2666 (2010).

195. Mayer, A. C., Scully, S. R., Hardin, B. E., Rowell, M. W. & McGehee, M. D. Polymer-based solar cells. *Mater. Today* **10,** 28–33 (2007).

196. Payne, M. M., Parkin, S. R., Anthony, J. E., Kuo, C.-C. & Jackson, T. N. Organic Field-Effect Transistors from Solution-Deposited Functionalized Acenes with Mobilities as High as 1 cm^2.V^-1.s^-1. *J. Am. Chem. Soc.* **127,** 4986–4987 (2005).

197. Locklin, J. & Bao, Z. Effect of morphology on organic thin film transistor sensors. *Anal. Bioanal. Chem.* **384,** 336–342 (2006).

198. Egginger, M., Bauer, S., Schwödiauer, R., Neugebauer, H. & Sariciftci, N. S. Current versus gate voltage hysteresis in organic field effect transistors. *Monatshefte Fur Chemie* **140,** 735–750 (2009).

199. Kalb, W. L., Haas, S., Krellner, C., Mathis, T. & Batlogg, B. Trap density of states in small-molecule organic semiconductors: A quantitative comparison of thin-film transistors with single crystals. *Phys. Rev. B* **81,** 155315 (2010).

200. Gibson, G. L., McCormick, T. M. & Seferos, D. S. Atomistic Band Gap Engineering in Donor-Acceptor Polymers. *J. Am. Chem. Soc.* **134,** 539–547 (2012).

201. Signore, G., Nifosì, R., Albertazzi, L., Storti, B. & Bizzarri, R. Polarity-Sensitive Coumarins Tailored to Live Cell Imaging. *J. Am. Chem. Soc.* **132,** 1276–1288 (2010).

202. Yamaguchi, S., Shirasaka, T., Akiyama, S. & Tamao, K. Dibenzoborole-Containing π-Electron Systems: Remarkable Fluorescence Change Based on the 'On/Off' Control of the π-π* Conjugation. *J. Am. Chem. Soc.* **124,** 8816–8817 (2002).

203. Jenekhe, S. A., Lu, L. & Alam, M. M. New Conjugated Polymers with Donor-Acceptor Architectures: Synthesis and Photophysics of Carbazole-Quinoline and Phenothiazine-Quinoline Copolymers and Oligomers Exhibiting Large Intramolecular Charge Transfer. *Macromolecules* **34,** 7315–7324 (2001).

204. Wu, W.-C., Liu, C.-L. & Chen, W.-C. Synthesis and characterization of new fluorene-acceptor alternating and random copolymers for light-emitting applications. *Polymer (Guildf).* **47,** 527–538 (2006).

205. Brabec, C., Scherf, U. & Dyakonov, V. *Organic Photovoltaics: Materials, Device Physics, and Manufacturing Technologies*. (Wiley, 2011). at <https://books.google.co.uk/books?id=DSGQi34Q36wC>

206. Hauch, J. A. *et al.* Flexible organic P3HT:PCBM bulk-heterojunction modules with more than 1 year outdoor lifetime. *Sol. Energy Mater. Sol. Cells* **92,** 727–731 (2008).

207. Voroshazi, E., Verreet, B., Aernouts, T. & Heremans, P. Long-term operational lifetime and degradation analysis of P3HT:PCBM photovoltaic cells. *Sol. Energy Mater. Sol. Cells* **95,** 1303–1307 (2011).

208. Peters, C. H. *et al.* High Efficiency Polymer Solar Cells with Long Operating Lifetimes. *Adv. Energy Mater.* **1,** 491–494 (2011).

209. Peters, C. H. *et al.* The Mechanism of Burn-in Loss in a High Efficiency Polymer Solar Cell. *Adv. Mater.* **24,** 663–668 (2012).

210. Song, Q. L. *et al*. Small-molecule organic solar cells with improved stability. *Chem. Phys. Lett.* **416,** 42–46 (2005).

211. AL-Amar, M. M. *et al*. A new method to improve the lifetime stability of small molecule bilayer heterojunction organic solar cells. *Sol. Energy Mater. Sol. Cells* **109,** 270–274 (2013).

212. Na-Na, W., Jun-Sheng, Y., Yue, Z. & Ya-Dong, J. Photocurrent analysis of organic photovoltaic cells based on CuPc/C 60 with Alq 3 as a buffer layer. *Chinese Phys. B* **19,** 38602 (2010).

213. Stapleton, A. *et al*. A multilayered approach to polyfluorene water-based organic photovoltaics. *Sol. Energy Mater. Sol. Cells* **102,** 114–124 (2012).

214. Salim, T. *et al*. Solvent additives and their effects on blend morphologies of bulk heterojunctions. *J. Mater. Chem.* **21,** 242–250 (2011).

215. Yao, Y., Hou, J., Xu, Z., Li, G. & Yang, Y. Effects of Solvent Mixtures on the Nanoscale Phase Separation in Polymer Solar Cells. *Adv. Funct. Mater.* **18,** 1783–1789 (2008).

216. Potscavage, W. J., Yoo, S., Domercq, B. & Kippelen, B. Encapsulation of pentacene/C60 organic solar cells with Al2O3 deposited by atomic layer deposition. *Appl. Phys. Lett.* **90,** - (2007).

217. Sachs-Quintana, I. T. *et al*. Electron Barrier Formation at the Organic-Back Contact Interface is the First Step in Thermal Degradation of Polymer Solar Cells. *Adv. Funct. Mater.* **24,** 3978–3985 (2014).

218. Peet, J., Senatore, M. L., Heeger, A. J. & Bazan, G. C. The Role of Processing in the Fabrication and Optimization of Plastic Solar Cells. *Adv. Mater.* **21,** 1521–1527 (2009).

219. Horie, M. *et al*. Cyclopentadithiophene based polymers-a comparison of optical{,} electrochemical and organic field-effect transistor characteristics. *J. Mater. Chem.* **20,** 4347–4355 (2010).

220. Pivrikas, A., Neugebauer, H. & Sariciftci, N. S. Charge Carrier Lifetime and Recombination in Bulk Heterojunction Solar Cells. *Sel. Top. Quantum Electron. IEEE J.* **16,** 1746–1758 (2010).

221. Coates, N. E. *et al*. 1,8-octanedithiol as a processing additive for bulk heterojunction materials: Enhanced photoconductive response. *Appl. Phys. Lett.* **93,** - (2008).

222. Jeng, U.-S. *et al.* A small/wide-angle X-ray scattering instrument for structural characterization of air{--}liquid interfaces, thin films and bulk specimens. *J. Appl. Crystallogr.* **43,** 110–121 (2010).

223. Wu, W.-R. *et al.* Competition between Fullerene Aggregation and Poly(3-hexylthiophene) Crystallization upon Annealing of Bulk Heterojunction Solar Cells. *ACS Nano* **5,** 6233–6243 (2011).

224. Waters, H. *et al.* Organic photovoltaics based on a crosslinkable PCPDTBT analogue; synthesis, morphological studies, solar cell performance and enhanced lifetime. *J. Mater. Chem. A* **1,** 7370 (2013).

225. Su, M.-S. *et al.* Improving Device Efficiency of Polymer/Fullerene Bulk Heterojunction Solar Cells Through Enhanced Crystallinity and Reduced Grain Boundaries Induced by Solvent Additives. *Adv. Mater.* **23,** 3315–3319 (2011).

226. Cho, S. *et al.* Bulk heterojunction bipolar field-effect transistors processed with alkane dithiol. *Org. Electron.* **9,** 1107–1111 (2008).

227. Heo, S. W., Kim, S. H., Lee, E. J. & Moon, D. K. Enhanced performance in bulk heterojunction solar cells by introducing naphthalene derivatives as processing additives. *Sol. Energy Mater. Sol. Cells* **111,** 16–22 (2013).

228. Lloyd, M. T. *et al.* Influence of the hole-transport layer on the initial behavior and lifetime of inverted organic photovoltaics. *Sol. Energy Mater. Sol. Cells* **95,** 1382–1388 (2011).

229. Hermenau, M. *et al.* Water and oxygen induced degradation of small molecule organic solar cells. *Sol. Energy Mater. Sol. Cells* **95,** 1268–1277 (2011).

230. Smith, G. (University of C. Personal communications.

231. Hintz, H., Peisert, H., Egelhaaf, H.-J. & Chassé, T. Reversible and Irreversible Light-Induced p-Doping of P3HT by Oxygen Studied by Photoelectron Spectroscopy (XPS/UPS). *J. Phys. Chem. C* **115,** 13373–13376 (2011).

232. Tsoi, W. C. *et al.* Effect of Crystallization on the Electronic Energy Levels and Thin Film Morphology of P3HT:PCBM Blends. *Macromolecules* **44,** 2944–2952 (2011).

233. Xu, Z. *et al.* Vertical Phase Separation in Poly(3-hexylthiophene): Fullerene Derivative Blends and its Advantage for Inverted Structure Solar Cells. *Adv. Funct. Mater.* **19,** 1227–1234 (2009).

234. Waters, H. *et al.* Effect of processing additive 1,8-octanedithiol on the lifetime of PCPDTBT based Organic Photovoltaics. *Org. Electron. physics, Mater. Appl.* **15,** 2433–2438 (2014).

235. Fukuhara, T., Shibasaki, Y., Ando, S. & Ueda, M. Synthesis of thermosetting poly(phenylene ether) containing allyl groups. *Polymer (Guildf).* **45,** 843–847 (2004).

236. Wang, L. *et al.* Thermal and physical properties of allyl PPO and its composite. *J. Appl. Polym. Sci.* **102,** (2006).